University of South-Eastern Norway

www.usn.no

FMH606 Master's Thesis 2023

Process Technology

Thermodynamics and fluid flow models for CO_2 flow assurance

Alua Akhmetova

Faculty of Technology, Natural sciences and Maritime Sciences

Campus Porsgrunn

Course: FMH606 Master's Thesis, 2023

Title: Thermodynamics and fluid flow models for CO_2 flow assurance

Number of pages: 118

Keywords: Carbon Capture and Storage, MACON CCS, CO_2 injection, leakage detection, upward and downward vertical flow, horizontal flow, FlowManager^{TM} and OLGA simulation

Student:	Alua Akhmetova
Supervisor:	Prof. Amaranath Sena Kumara Wahumpurage, Prof. Britt Margrethe Emilie Moldestad
External partner:	Angela Lynn De Leebeeck, Jaspreet Singh Sachdeva

Summary:

Carbon capture and storage (CCS) has been widely recognized as a potential method for lowering CO_2 emissions. MACON CCS is one of the CCS projects introduced in Norway by SINTEF in 2021. The project aims to facilitate large – scale deployment of CCS from industrial sources by solving specific and internationally acknowledged constraints in monitoring and controlling varied industrial CCS transport networks. TechnipFMC is collaborating with SINTEF and working on the project by combining thermodynamics and fluid flow models for CO_2 flow assurance.

The present study consists of three investigations: 1) understanding the degree to which the simulation model accurately represents CO_2 transport by comparing simulation results to experiments, 2) investigating the effect of adding impurities on CO_2 transport through simulations, and 3) completing study research on leakage detection methods suitable for subsea CO_2 transport.

Experimental data when CO_2 in a single gas, liquid, and two – phase flow was obtained from two experimental setups, one in a vertical and the other in a horizontal pipeline. In addition, the pressure gradient, density, and volume fraction of liquid from the experiments were compared to calculated data from FlowManager™ and OLGA software.

Analyzing the results when CO_2 is pure and in a two – phase flow regime applying numerical calculations precisely on the line where the experiments were taken was complicated based on PT calculations. Hence, according to the calculations in FlowManager™, using the PVT table from Multiflash results in poor density performance since the phase transition of CO_2 occurred. However, in OLGA, the calculations were based on the PH calculation, which allowed for the accurate estimation of gas and liquid density. There was no observed phase transition phenomenon; hence the pressure drop calculations performed better. A better match between calculated and experimental density significantly improved the model's pressure gradient predictions and volume fraction predictions.

The effect of impurities on the PVT characteristics of CO_2 was also investigated. The study discovered that a small quantity of impurities increases the phase envelope of CO_2 where it is in a two – phase flow. Therefore, the more impurities CO_2 has the more expansive the area of the two –phase flow regime.

While analyzing SINTEF's experimental results performed in a horizontal flow loop, it was observed that there was an inconsistency between measured and calculated data, with the calculated data underestimating the measured data by up to -50 %. Moreover, it is observed that when pure CO_2 is in a single gas or single liquid phase, the calculated pressure gradient values from both software were close to each other. In addition, when calculated densities were compared to NIST data, the relative error was noticeably modest.

SINTEF concluded that the pressure sensors installed on the horizontal flow loop could have an inaccuracy up to 35 % after 5 years of use, especially when the pressure drop between the sensors is very small, as was the case in the study. Therefore, the experiments completed by SINTEF in a horizontal flow loop will be repeated and simulations with new data will be completed in FlowManager™ by TechnipFMC.

Preface

This report is the final work of my master's thesis at the Department of Process Technology at the University of South-Eastern Norway, USN, spring 2023. The thesis was written in collaboration with TechnipFMC and SINTEF.

I would like to express appreciation to my supervisor Amaranath Sena Kumara Wahumpurage, Professor of USN's Department of Process, Energy, and Environmental Technology. I appreciate his assistance, encouragement, and support during the journey. Working with a supervisor with extensive experience and knowledge in academia and industry was an honor for me.

I also like to thank my co-supervisor Britt Margrethe Emilie Moldestad, Professor at the Department of Process, Energy, and Environmental Technology at USN, who always had confidence in me and for her constant support whenever needed.

I am grateful to my supervisor Angela Lynn De Leebeeck from TechnipFMC, for her support, advice, and sharing expertise with me. You have given me helpful guidance and support throughout this project. A special thank goes to Jaspreet Singh Sachdeva for his time and effort in supporting me with my simulations. All the feedback and sessions with discussions have improved my understanding and knowledge within this field, and I would like to show my appreciation to both of you.

A great thank you to Sigmund Smøttebråten, Manager FlowManager Services at TechnipFMC, for introducing me to the field of Carbon Capture and Storage, for showing interest in my work and finding positive outcomes from the results, and for giving me academic freedom and the opportunity to be part of this exciting project. Thank you for your considerable help in arranging a license for OLGA to simulate my models and complete the project.

I want to express my gratitude to Yessica Arellano and Jacob Stang from the SINTEF for allowing me to be part of the MACON project, for their help and support, and for providing experimental data for the project.

Finally, I greatly appreciate the support of my family and friends throughout my studies. I am grateful for everything you have done for me.

It has been an honor working with people with a lot to offer to academia and the industry. I did my best to develop the work as much as possible to prepare it for future studies, as there is much more that could be tested and done with this project. In addition, I made the thesis a valuable reference for prospective students interested in CCS and simulation topics. I hope you enjoy reading the thesis and learning more about this fascinating subject.

Porsgrunn, May 2023

Alua Akhmetova

Contents

List of Figures

List of Tables

Nomenclature

A	Area of a pipe	[m^2]
α_f	Volume fraction of flow	[-]
G	Gibbs Free Energy	[kJ/mol]
g	Gravity	[m/s^2]
H	Enthalpy	[kJ/mol]
I_f	Momentum of a flow	[kg·m/s]
M	Molar mass	[kg/mol]
m_{SG}	Mass flow rate of gas	[kg/s]
m_{SL}	Mass flow rate of liquid	[kg/s]
m_f	Mass of a flow	[kg]
p	Pressure	[bar]
Q	Heat Transfer Coefficient	[$W/m^2 \cdot °C$]
ρ	Density	[kg/m^3]
S	Entropy	[J/°C·mol]
T	Temperature	[°C]
t	Time	[s]
u_{SG}	Superficial gas velocity	[m/s]
u_{SL}	Superficial liquid velocity	[m/s]
u_f	Velocity of a flow	[m/s]
V	Molar volume of a gas	[l/mol]
x	Liquid Fraction	[-]

Abbreviations

AUVs	Autonomous Underwater Vehicles
CCS	Carbon Capture and Storage
CCSA	Carbon Capture and Storage Association
CCUS	Carbon Capture, Usage and Storage
Cl-ISE	Chloride Ion-Selective Electrode
CO_2	Carbon dioxide
DNV GL	Det Norske Veritas (Norway) Germanischer Lloyd (Germany)
EGE	Enhanced Greenhouse Effect
EOR	Enhanced Oil Recovery
EoS	Equation of State
FCM	Flow Control Module
FEED	Front End Engineering Design
FP	Fully Pressurised
H_2	Hydrogen
HSE	Health and Safety Executive
ID	Inner Diameter
IEA GHG	International Energy Agency Greenhouse Gases
IGCC	Integrated Gasification Combined Cycle
IOGP	International Association of Oil & Gas Producers
IPCC	Intergovernmental Panel on Climate Change
ISFET	Ion-Sensitive Field Effect Transistor
LCO_2	Liquefied Carbon dioxide
LNG	Liquefied Natural Gas
LPG	Liquefied Petroleum Gas
MACON CCS	Monitoring and Control of Networks for Carbon Capture and Storage
MAD	Mean Absolute Deviation
NCCS	Norwegian Carbon Capture and Storage (Research Centre)
NETL	National Energy Technology Laboratory
NIST	National Institute of Standards and Technology
NNSN	Norwegian National Seismic Network
NOK	Norwegian Krone

NPW	Negative Pressure Wave
OAWRS	Ocean Acoustic Waveguide Remote Sensing System
OD	Outer Diameter
OLGA	Oil and Gas (simulator)
pCO_2	potential Carbon dioxide
PFCs	Perfluorochemicals
pH	potential of Hydrogen
PLEM	Pipeline End Manifold
PVT	Pressure Volume Temperature
ROV	Remote Operated Vehicles
SCADA	Supervisory Control and Data Acquisition
SINTEF	The foundation for Scientific and Industrial Research at the Norwegian Institute of Technology
SPRT	Sequential Probability Ratio Test
SR	Semi-Refrigerated
STP	Standard Temperature and Pressure
VLE	Vapor-Liquid Equilibrium
ZEP	Zero Emissions Platform

1 Introduction

This chapter presents the thesis's background, objectives, scope of work, and structure.

1.1 Background

One of the most critical issues facing today's planet is global warming. A large portion of this growth is a direct result of the industrial revolution, followed by a rise in flue gas emissions. Greenhouse gas emissions over the last decade are at the highest levels in human history. According to scientific proof, the Carbon dioxide (CO_2) concentration in the atmosphere is constantly rising. The latest measurement in 2022 shows that the amount of CO_2 reached 420 ppm (parts per million) [1]. It shows the need for quick action. Limiting global warming to 1.5 °C above pre – industrial levels won't be possible unless there are immediate and significant reductions in emissions across all sectors. Nationally Determined Contributions, made public before COP26 (United Nations Climate Change Conference, 2021), imply that global greenhouse gas emissions would increase, increasing the likelihood that warming will reach 1.5°C and making it more challenging to keep it below 2 °C [2].

However, there are encouraging signals and more proof that climate action is being taken. Around three-quarters of greenhouse gas emissions now come from the energy sector, which also holds the key to preventing the worst consequences of climate change. Every industry has options to reduce emissions by at least halving them by 2030 and net zero by 2050 [3]. There is a global commitment to reduce emissions called The Paris Agreement. The Paris Agreement is an international agreement signed in 2015 by the United Nations Framework Convention on Climate Change (UNFCCC) [4]. The agreement's objective is to keep global warming well below 2 °C over pre – industrial levels and to pursue efforts to keep it below 1.5 °C. The Paris Agreement requires countries to set targets for decreasing emissions of greenhouse gases, which are the primary cause of climate change, to achieve this goal.

The Norwegian government is presently investing enormous resources in achieving global climate goals, and carbon capture and storage (CCS) has emerged as a critical area of focus. Due to this, there is more discussion, funding, and interest in CCS solutions. Norway has effectively used CCS in its national climate mitigation strategies for over 20 years. By offering significant CO_2 storage capacity, Norway's CCS Longship project will assist the European area in its decarbonization efforts as part of a continuous commitment to decrease emissions. The transition to a low – carbon society will be primarily facilitated by CCS technology, which will work together with a wide range of climate mitigation strategies in Norway and outside [5].

CCS consists of a facility for capturing CO_2, which is captured from flue gases or industrial operations, a transportation system, and a long-term storage location. The CO_2 must be transported from the capturing facility to the storage location through pipelines and ships. Only transportation via pipes will be of interest in this thesis. Carbon dioxide can be transported as a pure component or contain additional components like oxygen, nitrogen dioxide, sulfur dioxide, hydrogen sulfide etc. These species are expected to be present at low concentrations in the captured CO_2 and are called impurities. They change carbon dioxide's phase characteristics and affect pipeline transportation systems. Impurities can cause corrosion and introduce dust and solid formation, which may lead to operational difficulties. In addition, they can react with other components creating new impurities that might cause strong acids to

produce a more severe type of corrosion [6]. Therefore, a key component of managing the integrity of CO_2 transport pipes is identifying the types and quantities of impurities present in the carried CO_2 and the corrosion processes. Even though CCS has been used for many years, there are still issues with its feasibility and sustainability. Therefore, to improve safety and cost – efficiency, current knowledge of models and simulation tools for the multiphase flow of CO_2 with relevant impurities should be further enhanced.

1.2 Objective

The objective of the thesis is to contribute to the MACON (Monitoring and Control of Networks) CCS project, a collaboration between SINTEF and TechnipFMC, as well as other industrial partners. By addressing identified difficulties in monitoring and controlling future CCS transport networks, the project intends to assist CCS in becoming a broad, efficient climate policy instrument. The project is developing the structure for solving crucial data gaps to develop efficient and robust prediction flow models and sensor technology assessments for real-time monitoring of CCS streams for a large-scale CO_2 transport and storage infrastructure project in Norway.

The primary goal of this thesis is to compare simulation results to experimental data acquired from SINTEF flow studies for pure CO_2 existing in different phases. The simulations will be performed by multiphase flow simulator FlowManager™ developed by TechnipFMC and with dynamic multiphase flow simulator OLGA set by Schlumberger. In addition, the PVT table will be generated by the advanced thermodynamics software Multiflash. The purpose is to compare the simulation and experimental results and understand how accurately the simulation models can represent the physical phenomena governing the transport process.

Another area of research is the comparison of simulations using pure CO_2 and the effects of impurities on CO_2 transport. Although SINTEF did not conduct experiments for CO_2 with impurities during the thesis period, the impact of impurities on the PVT properties of CO_2 is also studied.

A further objective of the thesis is to research the most effective CO_2 leakage detection technologies applied during injection and transportation operations, which is a critical component of CCS.

1.3 Scope of work

The first aim of the work will be to study the PVT properties of pure CO_2 and CO_2 with impurities, as it is important to understand the effect of impurities on the transportation and injection processes into geological formations for long-term storage.

The experimental results will be compared to the simulated results. The experiments were carried out in two different experimental setups for pure CO_2 in different phases. The data from the experimental setup 1 is taken from the open-source paper [7] when pure CO_2 is in a two-phase flow regime. The data from experimental setup 2 was obtained very recently (April 2023) and has not been published yet. Some data analysis required before comparison with software calculations.

1.4 Thesis structure

Following an introduction in Chapter 1, a literature review of the research on the Carbon Capture and Storage (CCS) chain, its importance in fulfilling climate change targets, and the methods of CO_2 capture have been performed in Chapter 2. CO_2 transport via pipelines and ships has been discussed. Methods for detecting CO_2 leakage from reservoirs and during injection procedures are provided. Existing international CCS projects, as well as Norwegian CCS projects, are reviewed.

PVT properties of pure CO_2 and CO_2 with impurities were investigated in Chapter 3. For a better understanding of CO_2 properties, the phase envelope and Mollier diagram have been drawn. In addition, the impact of CO_2 impurities and the recommended maximum concentration in captured CO_2 have been discussed. Multiflash software was used to generate plots and data.

Chapter 4 covers the methodology of the thesis. Two experimental data sets from two independent experimental setups were used. Data from experimental setup 1 were obtained from the research paper titled "Upward and downward two-phase flow of CO_2 in a pipe: Comparison of experimental data and model predictions," published in the International Journal of Multiphase Flow [7]. The measurements were carried out in a 13.7 m long vertical pipeline with upward and downward flow when CO_2 exists in a two-phase flow regime. SINTEF presented data from experimental setup 2 in a 138 m long horizontal pipeline when CO_2 is present in a single gas, single liquid, and two-phase flow. Experiment data from both setups were compared to computed data from TechnipFMC's FlowManager™ software and Schlumberger's OLGA software. PVT table as the input file to the FlowManager™ software were generated by Multiflash. A brief description of the software's features and calculating method has also been provided.

Experimental setup 2 results analysis are performed in Chapter 5. The pressure correction method for four pressure sensors is explained to reduce the data's inaccuracy. Pressure sensor positions along the horizontal flow loop with corrected values are performed.

Chapter 6 contains simulation calculations and discussion. The calculated results from both software using the input parameters from two experimental setups are summarized and compared. In addition, the effect of the presence of impurity as methane was studied for vertical upward flow using the same input value as pure CO_2. Simulations using PVT tables generated with different EoS were evaluated, and the results with the closest match to the measured data were chosen as the input file to the FlowManager™. The parameters as pressure drop, density, and volume fraction of liquid were analyzed.

Conclusions from the main findings from this study and further work recommendations are summarized in Chapter 7.

2 Literature review

This chapter provides an overview of the research on Carbon Capture and Storage (CCS) and its impact on climate change. The fundamental CCS chain has been discussed, including CO_2 capture and its types and techniques, transportation, and storage. CO_2 leak detection techniques from reservoirs and pipelines have been researched, as well as their influence on the atmosphere, leakage size, types, and time to discover and fix them. Furthermore, leakage monitoring methods used in CCS projects have been covered. Existing and planned international CCS projects and CCS projects in Norway are also covered in the chapter.

2.1 What is Carbon Capture and Storage (CCS)?

CCS is a well – known climate change-reducing technology. Carbon dioxide is captured at power plants or industrial plants, transported, and injected into suitable geological formations. Such formations may be onshore or offshore. Offshore transport can take place through pipelines or ships. Lowering greenhouse gas emissions into the atmosphere is the primary benefit of storing carbon dioxide underground.

CCS technology can capture and store up to 90 % of CO_2 emissions from big emitters such as electricity utilities and energy – intensive emitters such as cement kiln facilities and others [8]. Reduction and removal of carbon emissions are now scientifically proven and recognized by the European Taxonomy for Sustainable Finance [9] and the Clean Planet for All [10] reference scenarios. CCS chain consists of the following steps: capture, transportation, storage. Figure 2.1 gives an overview of the CCS operational framework.

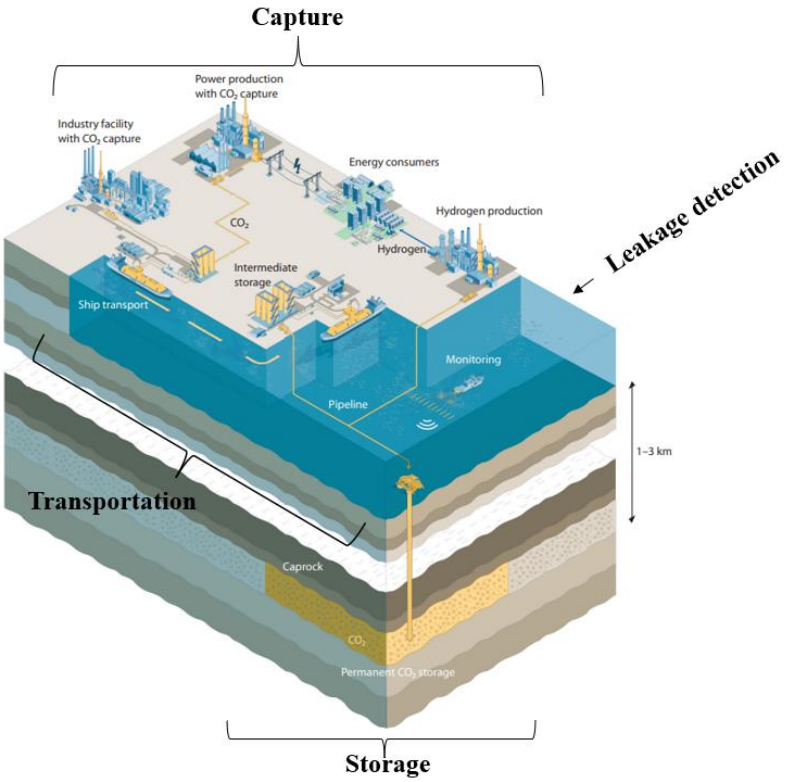

Figure 2.1: Modified illustration of CCS chain [11].

2.2 Role of CCS in meeting climate change targets

CCS application can significantly contribute to climate change mitigation. Its potential for carbon emissions reduction and removal is scientifically proven and has been operational since the 1980s. Over the past 40 years, human activity has captured and stored more than 260 million tons of CO_2 emissions, with an estimated 40 million tons of CO_2 being caught and stored annually [12]. As several large – scale CO_2 capture projects are near – ready, a CO_2 transportation network and storage infrastructure would connect CO_2 emitters in industrial clusters and power plants to storage sites and enable the timely and extensive decarbonization needed to meet the net – zero target.

2.3 How is CO_2 captured?

CO_2 is produced during the combustion, and the type of combustion process directly affects the choice of a suitable CO_2 removal process. There are three basic types of CO_2 capture:

- post – combustion capture
- oxy – fuel combustion capture
- pre – combustion capture

The methods are costly, accounting for around 70 – 80 % of the overall cost of a complete CCS system that includes capture, transport, and storage [13].

2.3.1 Post – combustion capture

Post – combustion capture is a process that removes CO_2 from flue gas after combustion has occurred. The method is ideal for thermal power generation, such as fossil fuel, biomass, municipal waste, and other waste – to – energy plants. CO_2 separates from combustion exhaust gases and can be captured using a chemical solvent or other separation methods [13]. As can be seen from Figure 2.2, the steam and flue gas are released after fuel combustion. The steam is used for energy generation (i.e., used in turbines). At the same time, the flue gas enters the post – combustion stage, where the flue gas undergoes separation to isolate the CO_2 from the nitrogen and water. Separating CO_2 from the other components makes this stage the most difficult. The most effective and established separation methods are absorption, adsorption, or membrane systems [14].

Post – combustion CO_2 capture effectively reduces greenhouse gas emissions from industrial facilities that burn fossil fuels. However, running the capture and regeneration processes demands a lot of energy, which can result in decreased efficiency and more significant expenses for the facility. Developing more efficient and cost – effective post – combustion CO_2 capture methods, such as employing novel solvents or combining the process with power generation to minimize energy usage, is ongoing [15-17].

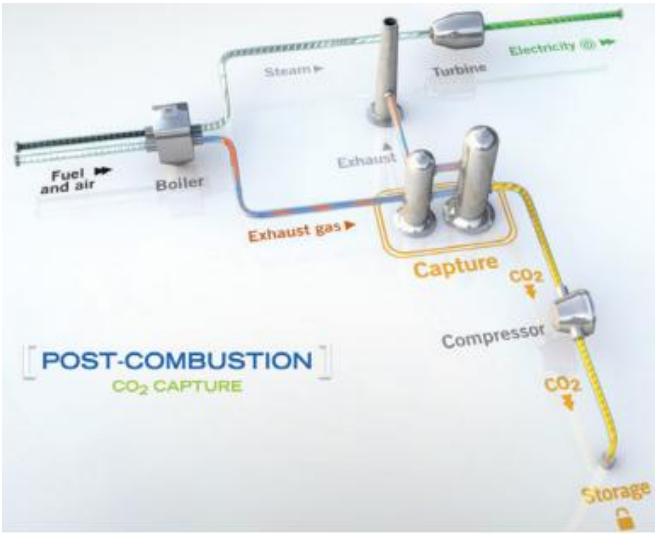

Figure 2.2: Flow process of post – combustion technology [18].

2.3.2 Pre – combustion capture

The pre – combustion method of CO_2 capture is primarily utilized in power plants that use fossil fuels like coal, natural gas, or petroleum. This technology captures CO_2 before the fuel is consumed, making it an efficient solution to minimize greenhouse gas emissions [19]. The technology is instrumental in large – scale industrial applications, such as power plants, where considerable amounts of CO_2 can be captured and stored. Some examples of pre – combustion techniques that capture CO_2 include Integrated Gasification Combined Cycle (IGCC) power plants, natural gas processing plants, hydrogen production, petrochemicals production, etc. [20-22].

In this process, the fuel is pretreated before combustion. As can be observed from the Figure 2.3, nitrogen (N_2) is discharged at the air separation unit before entering the gasifier unit. In the gasification process, fuel is partially combusted or transferred while consuming little oxygen. As a result, syngas, produced by this gasification process, primarily contains carbon monoxide (CO) and hydrogen (H_2). The syngas then passes through a water gas shift process, where the CO is converted into CO_2, and the steam produces additional H_2.

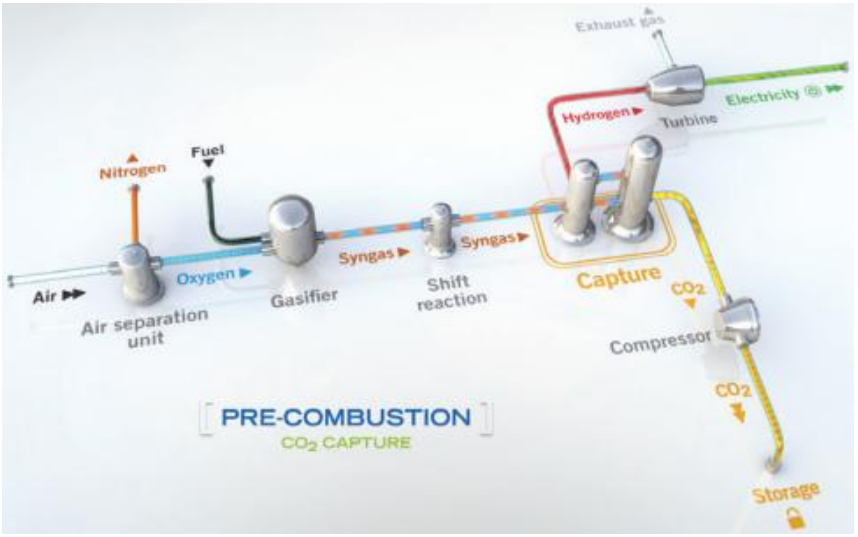

Figure 2.3: Flow process of pre – combustion technology [18].

Separating the CO_2 from the fuel component is not as difficult because the compound contains a large concentration of CO_2 and can be separated through different processes, such as absorption, adsorption, cryogenic processes, or passage through a membrane. Before the fuel enters the gas turbine, CO_2 is captured by a solvent at high pressure, which is released by lowering the solvent's pressure. Nonetheless, the most profitable technique is absorption [23]. Hence, the CO_2 is prepared for the process of compression and storage.

2.3.3 Oxyfuel combustion

Oxyfuel combustion uses pure oxygen rather than air to burn fuel such as natural gas, coal, or propane. When oxygen is used instead of air in the combustion process, a high – temperature, high – pressure gas is produced, which may be used in various industrial applications such as melting glass or steel, producing cement, power generation, and waste – to – energy [24-26]. Figure 2.4 demonstrates oxyfuel combustion process where after the separation of N_2 at the first air separation unit step, oxygen is used for combustion. This results in the generation of steam and exhaust gas containing CO_2 and water vapor. Steam is used for energy generation, and a capturing technique can separate the flue gas.

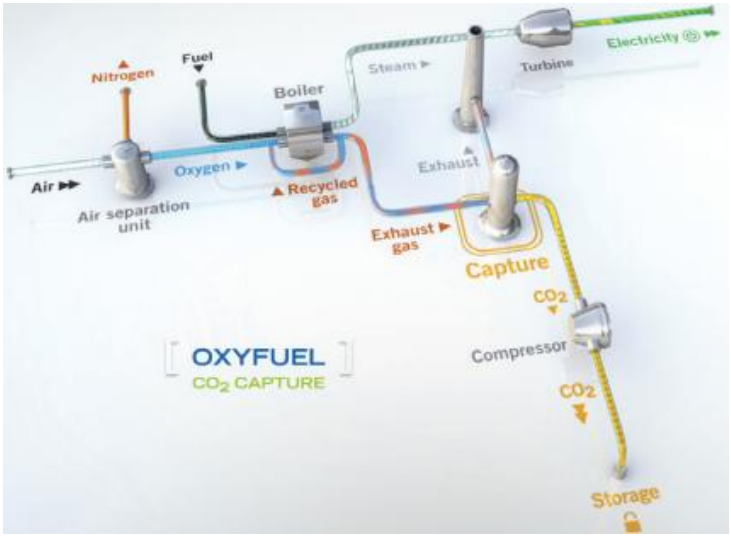

Figure 2.4: Flow process of oxyfuel combustion technology [18].

The advantages of the oxyfuel combustion technique are that it does not involve a CO_2 separation step, and some of the flue gas produced can be reused in the boiler for combustion. However, this process has a higher cost than the other combustion methods, which are obtaining pure oxygen from air and flue gas recirculation [27, 28].

Since all three carbon capture methods are essential to the CCS process, researchers are interested in reducing the energy costs for all three methods.

2.4 CO_2 transport

Once CO_2 is captured, it needs to be transported to a storage site for permanent injection into a geological formation. As a result, a dependable, safe, and cost – effective transportation system is essential for any CCS project. Depending on the volume of CO_2 to be carried, ships and pipelines can be used.

Transportation of CO_2 by ships will be economically feasible for relatively long transport distances and relatively small volumes [29, 30]. However, transportation by pipelines is considered the most economical for high volumes of CO_2 and is primarily used to transport CO_2 from the onshore plant to the injection well(s) in the reservoir on the continental shelf [31].

2.4.1 Ship transport of CO_2

CO_2 transported by ships is in single phase liquid. The transit distance is essential when comparing ship transport to pipeline transport. According to economic calculations study, long transport lengths favor ship transport of CO_2 over pipe transport [29]. Ship transport also has the flexibility to collect CO_2 from various low – cost sources, distribute it to different locations, and the comparatively cheap capital expenditure for ship – based transport compared to pipeline transport. According to Skagestad et al. [32], the key cost drivers for the ship are

liquefaction and operational expenses, whereas the main cost factor for pipeline transport is capital investment cost.

In Northern Lights project, CO_2 is transferred from capture facilities in ship storage tanks at a pressure between 13 and 15 bar; as the volumes to be transported (7500 m^3 ship) was small, it was decided to transport at medium pressure, with corresponding equilibrium temperatures. At the Northern Lights terminal, CO_2 is transported from the ship storage tank to onshore storage tanks at a pressure of 13 to 18 bar at the top of the onshore storage tanks, with appropriate equilibrium temperatures [33]. SINTEF released a paper entitled "At what Pressure Shall CO_2 Be Transported by Ship? An in-Depth Cost Comparison of 7 and 15 Bar Shipping" [34]. The current research investigated transport pressure choices of 7 and 15 bar over various annual volumes and transport lengths, including evaluations for CO_2 purity and impurity scenarios. The results reveal that shipping CO_2 at 7 bar and -46 °C is more cost-effective than shipping at 15 bar and might result in considerable cost savings, up to around 30 % in most cases. Despite the significant cost savings potential of 7 bar, Equinor in Northern Lights project chose shipping CO_2 at 15 bar due to its technological maturity. Shipping with 7 bar is likely the preferred solution for new development once it has been demonstrated to be reliable and safe on a large scale, such as preventing dry ice production and hydrates in the preparation and transportation supply chain.

Equinor's Shipping Logistics studies [33] reveal that for demonstration project quantities, a ship type closely resembles Fully Pressurised LPG ships modified to carry LCO_2, which requires higher pressure, would fulfill the technical criteria well. The modification required the change of material in the construction of the ship tanks to high tensile steels, re – engine, and capacity. Furthermore, existing experience in liquid CO_2 shipping in the small – scale food – grade business serves as a channel for information exchange, scaling demonstration, and proof of concept. Figure 2.5 demonstrates new ship construction, the most likely ship type for CCS's transportation processes. The transport requirements will determine the vessel type. For example, if CO_2 will be transported at medium pressure, the Full Pressurised (FP) vessel type will be selected. However, if it has to be transported at a lower pressure (6 - 8 bar), a semi-refrigerated (SR) vessel will be used [33].

Figure 2.5: Demonstration of ship for CO_2 transport [33].

In the paper [35], Omata investigated LPG carriers and saturated liquid transfer at -10 °C and a pressure range between 26.5 - 28 bar. The research covers the technological and economic effectiveness of a CO_2 transport system. One key emphasizing idea is employing a carrier ship with injection equipment on board to deliver straight to a subsea injection wellhead. This is an excellent alternative method in regions such as Eastern Asia, where bulk resources are often transferred at great distances globally by sea. It seems reasonable to apply it to CO_2 transport processes as well.

Impurities in the CO_2 concentration play an essential part in the process. It will impact the CO_2 phase diagram by expanding the two-phase flow regime, potentially causing corrosion and safety hazards. In 2022, ZEP/CCSA published a report named "Guidance for CO_2 transport by ship" [36]. It was mentioned that the primary objective is to transport CO_2 in the ship when the concentration of it is > 98 %. The rest will consist of impurities. Furthermore, it listed the type of relevant impurities and their impact on health and safety problems during transportation.

2.4.2 Pipeline transport of CO_2

In the Nordic region, there are very few onshore pipelines for transporting CO_2. As a result, they concentrate primarily on offshore pipelines. Focusing on offshore pipelines is motivated by two factors. Firstly, the Nordic area has extremely few onshore pipelines. As a result, onshore pipelines would face significant public resistance and extensive licensing processes. Secondly, Nordic conditions often imply that onshore pipes must travel through rough ground involving mountains, valleys, and solid foundation rock. This may result in ten to twenty times higher laying costs than similar offshore pipelines [37]. Pipeline transportation of CO_2 over longer distances is regarded as most efficient and economical when the CO_2 is in the dense phase, i.e., in a liquid or supercritical regime. This is because the friction losses along the pipeline per unit mass of CO_2 is lower [38]. To maintain a steady single phase flow through the pipeline, the recommended pressure and temperature range for a CO_2 pipeline is between 85

and 150 bar and 13 °C and 44 °C [39]. The pressure drop caused by the decrease in hydraulic head throughout the pipeline can be compensated for by adding recompression facilities. Bigger diameter pipes allow for lower flow rates with less pressure loss and, hence, fewer recompression facilities are required; nevertheless, larger pipelines are more expensive, so cost balancing must be considered [39].

Equinor runs multiphase pipe flow simulations for the Northern Lights project to select the pipeline's pressure and capacity. It has been concluded from the study that pipeline transport capacity will depend on the wellhead pressure, pipeline length, and export pressure from the onshore facility [33]. The Figure 2.6 represents the subsea pipeline from Naturgassparken to the well location in the Aurora reservoir.

Figure 2.6: Demonstration of subsea pipeline connected to terminal [33].

The presence of impurities in the CO_2 stream is another difficulty with CO_2 transportation. Since their existence can affect the pressure and temperature envelope boundaries within which a single phase flow is stable, it can create significant problems. Moreover, the presence of free water may result in the development of carbonic acid inside the pipeline, causing corrosion issues [40]. Hydrates can also develop, which can interfere with the operation of valves and compressors [41]. Finally, it should be noted that CO_2 mixtures from different capture technologies will have other dynamic behavior in pipelines [42]; hence it should be appropriately analyzed. As a result, transient two – phase flow effects must be considered while designing and operating CO_2 – transport pipeline networks.

CO_2 pipelines are mostly carbon steel and consist of insulated 12 – meter sections with crack arresters every 350 meters and block valves every 16 – 32 kilometers. The onshore pipes are buried 1 m deep. Offshore pipes in shallow water must also be installed in channels to prevent fishing and anchoring operations. However, deep water pipes are often only required to be buried if their diameter is less than 400 mm [43, 44]. The spool connecting the CO_2 pipeline

end PLEM (Pipeline end manifold), and the single well satellite structure must also be protected by the steel protection covers to ensure overflow and protection of all critical parts. Northern Lights project illustrated in Figure 2.7 how steel covers can protect a spool [33] . The pipelines must be monitored regularly to guarantee their integrity, and an accurate fiscal metering system must be in place to ensure the measurement of the accumulated fluxes. In addition, pipelines need to survive the harsh conditions found within CO_2 transportation, such as low CO_2 lubricating capacity, strong chemical reactivity, and high pressure, which can impact monitoring and metering equipment performance [45].

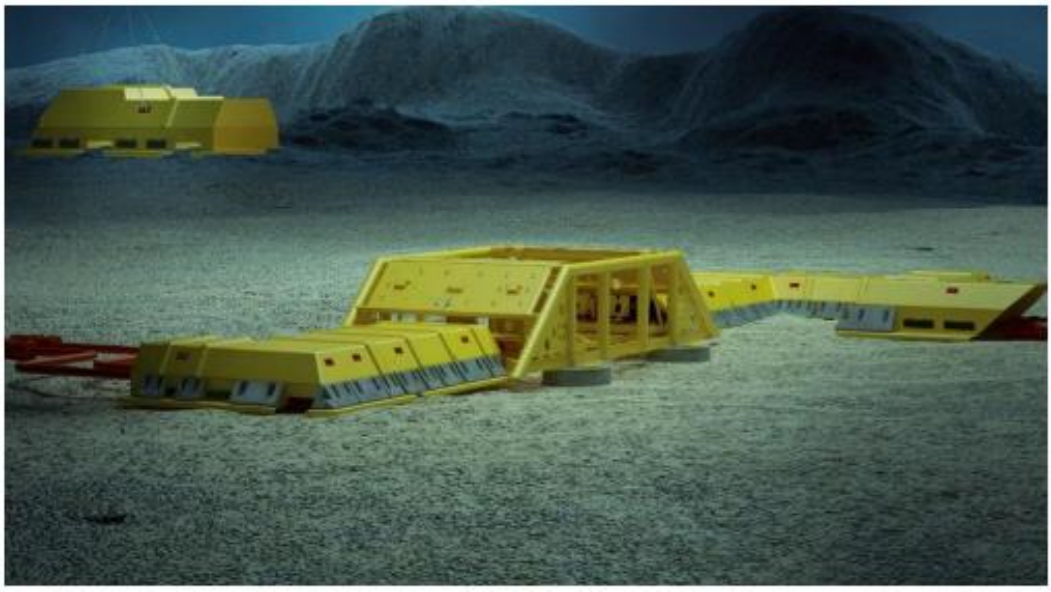

Figure 2.7: Illustration of spool protection [33].

Table 2.1 illustrates current CO_2 pipelines across the world.

Table 2.1: Existing and planned CO_2 pipeline projects [46-48].

Project name	Country	Length (km)	Capacity (Mt/y)	Onshore/Offshore
Quest	Canada	84	1.2	Onshore
Alberta Trunk Line	Canada	240	15	Onshore
Weyburn	Canada	330	2.0	Onshore
Saskpower Boundary Dam	Canada	66	1.2	Onshore
Monell	USA	52.6	1.6	Onshore
Bairoil	USA	258	23	Onshore
West Texas	USA	204	1.9	Onshore
Transpetco	USA	193	7.3	Onshore
Salt Creek	USA	201	4.3	Onshore
Sheep Mountain	USA	656	11	Onshore
Val verde	USA	130	2.5	Onshore
Slaughter	USA	56	2.6	Onshore
Cortez	USA	808	24	Onshore
Central Basin	USA	231.75	27	Onshore
Canyon Reef Carriers	USA	225	4.4	Onshore
Chowtaw (NEJD)	USA	294	7	Onshore
Decatur	USA	1.9	1.1	Onshore
SACROC	USA	354	4.2	Onshore
Este	USA	191	4.8	Onshore
Bravo	USA	350	7.3	Onshore
Snøhvit	Norway	153	0.7	Both
OCAP	Netherlands	97	0.4	Onshore
Lacq	France	27	0.06	Onshore
Rhourde Nouss-Quartzites	Algeria	30	0.5	Onshore
Qinshui [P1]	China	116	0.5	Onshore
Gorgon	Australia	8.4	4	Onshore
Bati Raman	Turkey	90	1.1	Onshore

[1] P noted as planned to be in operation.

Lu, Hongfang published a paper [48] which covered a brief overview of CO_2 transportation via pipeline and where it was divided into four parts: process, pipeline design, safety, and risk, and standard and specification. The following are the key findings:

- Control of temperature and pressure is the main focus of pipeline operation. The effect of impurities still needs to be analyzed.
- Design of the pipeline, although the CO_2 pipeline and natural gas pipeline are similar, their design considerations are still different.
- The ductile fracture and fracture control methods for CO_2 pipelines still need to be better understood. The study and inspection of the consequences of CO_2 pipeline leaking has also been a research hotspot in recent years since it may assist in enhancing the risk assessment system.
- CO_2 pipeline standards and specifications, as well as the associated integrity management system, must be upgraded.

Hence, the need for further development of the fundamental principles behind the development of CO_2 transportation pipelines can be highlighted.

2.5 CO_2 leakage

CO_2 may seep from the reservoir and reach the surface, spilling into the atmosphere. The primary focus of CO_2 storage monitoring techniques has been to monitor plume behavior in storage formations and to detect leakage to the environment. The cost of using geological formations offshore for CO_2 storage is much greater than that of similar onshore activities. Every piece of equipment must resist a hostile environment, which increases the expense of long – term monitoring systems compared to onshore systems. This also applies to the costs of leakage monitoring equipment installation and maintenance.

CO_2 leakage can occur from two primary sources: CO_2 transportation facilities or storage areas. Injection wells have been identified as the most likely source of leakage. As a result, maintaining wellbore integrity is essential for guaranteeing geological formation separation, particularly in areas with a history of oil and gas development and production [49]. Leakage from geological formations is commonly caused by two mechanisms: leaking via caprock and leakage through permeable pathways. Typically, leakage through caprock is gradual and may take tens of thousands of years [50], but spreading through permeable pathways is rapid and causes more significant problems [51].

In the work [52], P. Patil investigates the reasons for leaks from injection or abandoned wells. Possible leakages discovered by the study can occur between:

- cement plug and casing interface
- casing and annular cement interface
- annular cement and formation interface
- through corroded casing walls
- through cement plug
- through annular cement

CO_2 leakage from the storage area into the atmosphere might occur due to isolated, catastrophic events, such as an earthquake, or prolonged, gradual venting of CO_2 due to poor storage site selection or preparation. Any of these leaks would result in high CO_2 concentrations at the

surface or in the shallow subsurface, harming human health and safety as well as the health and safety of surrounding plants and animals. Therefore, analyzing the probability of CO_2 leakage requires first evaluating the effectiveness of the storage facility. Storage effectiveness is determined by various site-specific factors, including geological properties, the injection technology employed, and the procedures used to seal and hold CO_2 within the injection site [53]. As a result, research on leakage/risk assessment has received much attention in CCS investigations.

In 2019, DNV GL calculated the mass flow rate of released CO_2 using the software OLGA and the corresponding dimensions of the leakage for the Northern Lights project as input [54]. Table 2.2 displays information regarding the leakage size, rate, the time needed to identify the leakage, and the time required for human involvement to repair it. Leakage rate numbers represent the average of the first 30 minutes.

Table 2.2: The CO_2 release characteristics of Northern Lights pipelines [54].

Leakage category	**Leakage size (mm)**	**Leakage rate (kg/s)**	**Time for detection**	**Time to fix after detection**
Small (< ø20 mm)	2	0.6	6 months	1 month
	5	4	24 h	1 month
	10	15	24 h	1 month
Medium (ø20 mm – ø80 mm)	20	58	12 h	26 days
	50	255	15 min	6 days
Large (> ø80 mm)	100	411	15 min	3 days
Full pipe rupture	2 × ø239	700	15 min	1 day

Potential methods for detecting medium leaks in the pipeline system include:

- The estimated flow export from the tanks (level decrease) is too large compared to the flow rate into the well.
- The pump's flow rate is too high, and the pump will not be able to sustain a pressure of 45 bar at the pipeline input.
- The onshore tanks will be emptied far sooner than expected.
- Mass balance system; required input from flow measurements at both pipeline's endpoints.

The mass balance system is based on flow measurements at both ends and where the sum of mass flow rates into the control volume, which is the pipeline, and mass flow rates out of the control volume must be equal to the rate of the change of mass inside the control volume. A comparison of flow into and out of the system reveals considerable flow loss, including leaks.

The pressure and flow decrease between pressure sensors and flow meters deployed in the subsea production system or pipeline is monitored using mass balance as a leak detection method. If the imbalance surpasses a certain level, an alert will be triggered. The system monitors continuously and will alarm within minutes to one or several hours, depending on the extent and location of the leak. Massive leaks, for example, can be recognized in minutes with the proper system design, but tiny leaks may take longer to detect or may only be noticed once a scheduled Remote Operated Vehicles (ROV) inspection catches it visually [33]. Mass balancing as a leak detection method has some advantages and disadvantages [55].

Advantages:

- May use existing process instrumentation such as pressure and flow transmitters.
- Not weather dependent, and the technology is mature. Therefore, it is considered an excellent approach when production rates are high and stable.

Disadvantages:

- Poor system sensitivity.
- System accuracy during multiphase flow.
- Difficulty configuring the system effectively to minimize false alarms in these scenarios.

K. Li developed the experimental facility to investigate the thermodynamic and fluid dynamic behavior of the CO_2 leakage process when it is in the supercritical phase [56]. Based on the laboratory pipeline leaking system, inner pressure, mass outflow rate at the leakage nozzle, and Nusselt number in the pipeline were analyzed [57]. The primary purpose of the work was to study the leakage flow behavior in the damaged pipeline, which considerably impacts estimating the impact of accidental leaking and improving the leakage detection equipment. In addition, during the leaking process, a phase – transition phenomenon was noticed. Therefore, the mass flow rate and Nusselt number data might be used for leakage detection and verifying numerical simulations of supercritical – gas multiphase flows in the pipeline leakage process [56, 58]. As a result of the leakage, the experiment produced a typical highly under – expanded jet flow. As seen in Figure 2.8, the jet flow was made approximately 1 s after the leakage and gradually decreased as time passed.

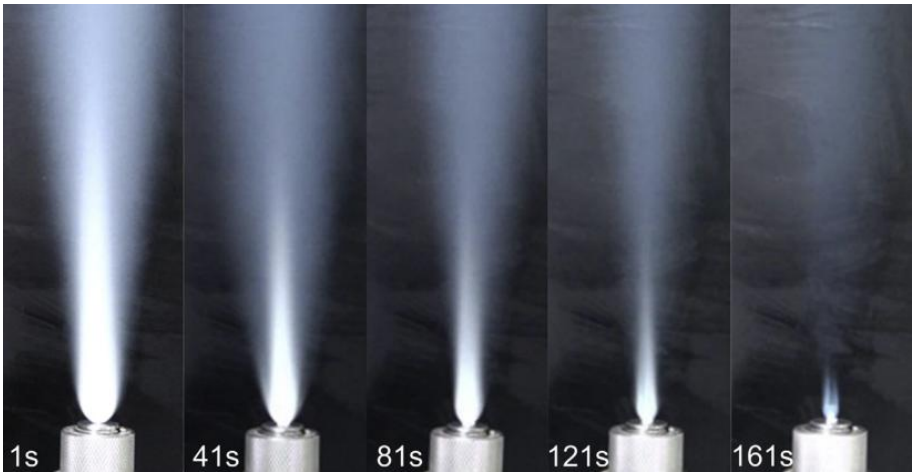

Figure 2.8: Pure CO_2 jet flow at 9 MPa initial pressure with a 1 mm nozzle [56].

Because of the high – pressure expansion, the jet flow has a significant Joule – Thomson effect, and the temperature of air surrounding the leaking nozzle rapidly declines [56, 59]. During this process, a white visible potential core filled with high – density CO_2 developed and weakened as the pressure decreased. Another problem of concern is the formulation of the dry ice bank around the leakage nozzle. The development of the dry ice bank is shown in Figure 2.9. Due to the Joule – Thomson effect of the CO_2 near the leakage nozzle, a rapid temperature drop occurred, which could fall below the melting point of the CO_2 leading to the formation of a flimsy dry ice bank and can be divided into four stages [56, 60]. The experimental research findings are the first – step measurements performed in the laboratory pipeline leaking system for pure CO_2.

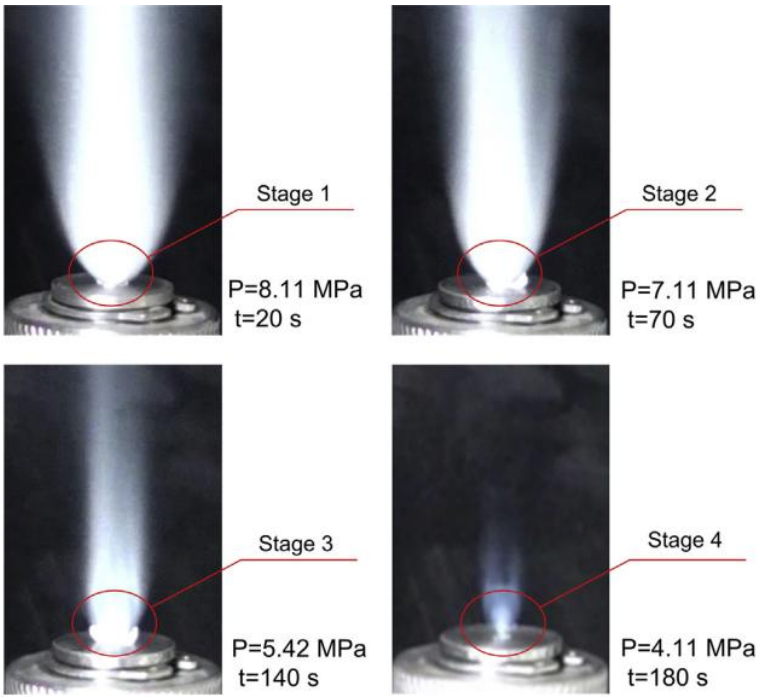

Figure 2.9: The dry ice bank's development process [56].

In addition to traditional leakage detection techniques for subsea injection systems, such as pressure readings from the X-mas tree and Flow Control Module (FCM), the installation of a leak detector is being studied for the Northern Lights Project. CO_2 sniffers and acoustic detectors can be used to identify leaks. The leak detector must detect and identify CO_2 leakage on all equipment positioned on the X-mas tree, FCM, and flow base, also known as the CO_2 header. The instrument must trend data and communicate chosen data to standalone screens, including leak detection alarms. Leak detection alarms must identify the location of the leak. If a leak occurs on the pipeline, the length and dispersion of the leak may be reduced by using leak detection, which results in the source or landfall emergency shutdown valve being shut down. The time for detection will depend on the size of the leakage. For large leaks, the leak source may be stopped quickly; however, small leaks may take a long time to be detected [33].

Many other studies have been conducted to model the consequences of geological CO_2 leakage. Figure 2.10 shows a schematic representation of CO_2 leaking from the seafloor. Case 1

represents the direct leakage of sequestered CO_2 into the ocean, and Case 2 represents the diffusion of sequestrated CO_2 into the pore water [61].

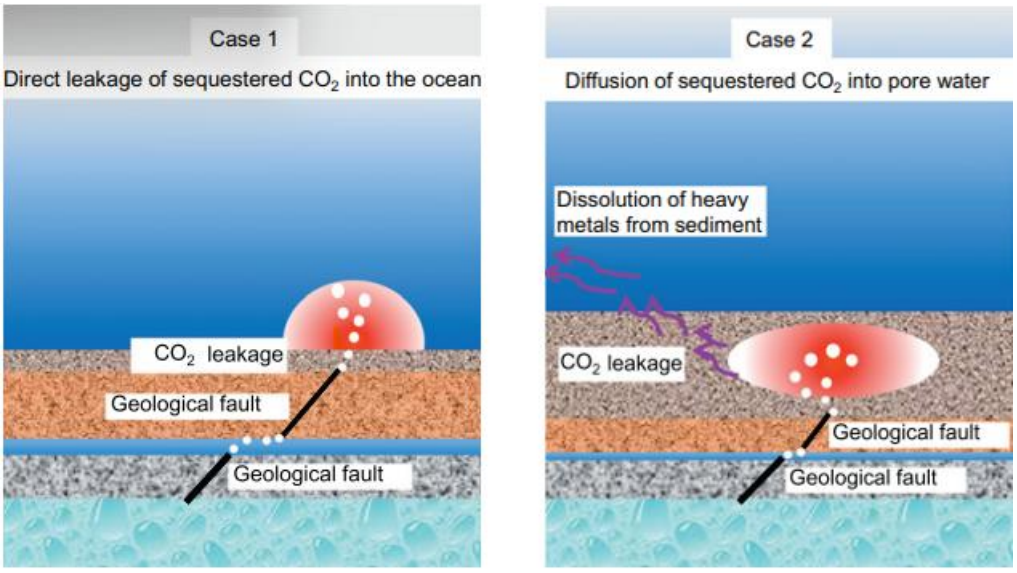

Figure 2.10: Representation of CO_2 leakage from the sub-seabed [61].

Further, detection and monitoring techniques applicable for both cases and the pipeline's leakage detection methods will be discussed, with leakage monitoring classified as surface and downhole monitoring.

2.5.1 Monitoring methods used in several CCS projects

IEA GHG published a report in 2012 titled "Quantification techniques for CO2 leakage," which discussed applicable methods used or could be suitable potential methods in the future [62]. Regarding the information [8, 62], monitoring methods used in some CCS projects have been summarized in Table 2.3 and described in the sections below.

Table 2.3: Monitoring methods applied in CCS projects [8, 62].

Methods	Sleipner project	Frio project	Nagaoka project	Ketzin project	In-Salah project	Otway Basin project	Weyburn projet
3D seismic	X		X	X	X	X	
4D seismic				X			
Micro – seismic	X		X				X
Vertical seismic profiling		X					
Gravimetry	X				X		X
Cross – hole electro-magnetical		X		X	X		
Pressure and temperature		X	X	X			
Geochemical sampling		X	X			X	X
Soil – gas		X			X		X
Tracers		X			X	X	
Atmospheric monitoring						X	
Microbiology				X			
Core sampling							X
InSar					X		

2.5.2 Atmospheric monitoring

Monitoring the atmospheric CO_2 content in the storage area can be used to detect deviations from the natural baseline. However, the reliability of these procedures may need to be improved by significant natural variations in CO_2 readings caused by soil respiration, organic matter breakdown, or unusual weather conditions [63]. The report presented by IEA GHG atmospheric monitoring methods using diode lasers has been discussed in detail [62].

2.5.3 Detecting bubble streams

Small leakages dissolve in water, but at high leakage rates, gas bubbles develop and rise from the bottom. Modern sonar devices can therefore examine extensive regions of seabed for evidence of leaking. In addition, high – resolution approaches may be used to identify bubble streams as hydroacoustic flares in various ways. To successfully monitor a storage site, the seabed above the facility must be scanned regularly for evidence of gas leakage. Practically, such an area is too huge for continuous monitoring; hence a ship – mounted system investigation of the seafloor and water column for unexpected signals is required to find suspected leaks. The sonar technology has significantly changed in recent years as on – site processing power has increased from traditional single – beam sonar to multibeam systems and side-scan sonar, which allow digitization and real – time 3D – visualization of the water column [62].

Figure 2.11 presents a 3D visualization of methane plumes at 1200 - 1900 m sea depths off the west of the United States, as imaged acoustically with a Kongsberg EM 302 multibeam sonar [64]. The surveys produced precise information on the seafloor's topography and sediment structures that could signal leakage. The data also provides detailed information about the plume's location, size, and shape.

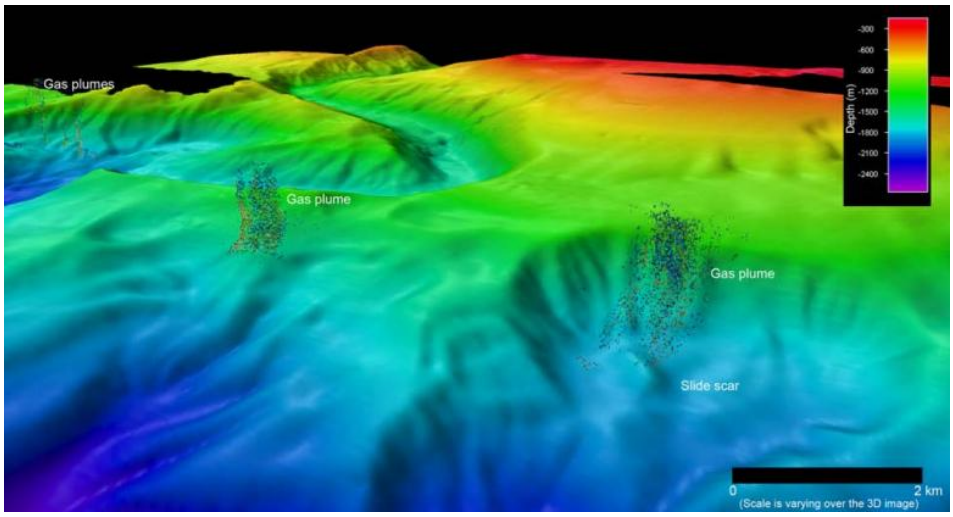

Figure 2.11: 3D visualization of gas seeps off the northern California margin [64].

GasQuant is a hydroacoustic swath system based on a lander created to detect bubble discharge fluctuation at seeps. It's a sonar – like device with a horizontally oriented swath with a 63° swath angle that records bubbles crossing it [62, 65]. Figure 2.12 demonstrates the system's dimensions and the extent of the swath's coverage area. It can monitor an area of around 2000 m^2. It was not, however, built for long-term monitoring over months. Therefore, energy supply is crucial over a lengthy period.

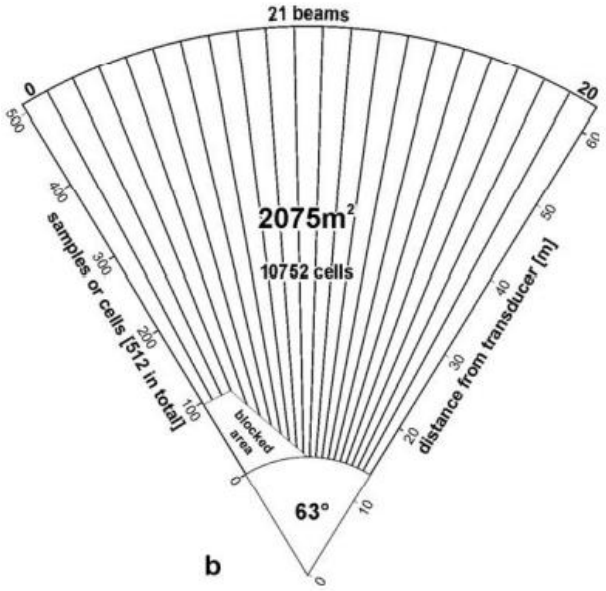

Figure 2.12: Dimensions of the hydroacoustic swath [65].

The Long Range Ocean Acoustic Waveguide Remote Sensing System (OAWRS) is another alternative with a vast coverage area in the hundreds of square kilometers [62, 66]. Unfortunately, this runs considerably lower frequency and needs a better resolution. However, OAWRS may be appropriate for first pass surveying of a storage site, with the ability to discover catastrophic leaks of substantial geographical extent.

2.5.4 Seismic monitoring

Seismic surveys, such as 3D and 4D seismic, are practical monitoring tools in a carbon capture and storage project, providing useful geological information where lateral formation changes, large-scale features, and a rock characteristic distribution can be observed. Recent research has proved the effectiveness of the seismic method in a time – lapse format for monitoring CO_2 geological storage [67-69].

Active and passive technologies can both be used. Active seismic uses an energy source to create acoustic waves, which are detected and analyzed to learn about the underlying geology of the storage region, whereas passive seismic uses geophones to record tremors and micro – earthquakes caused by fluid movement or crack development. In addition, the time-lapse of 4D monitoring is utilized to trace the evolution of the CO_2 plume over time. In contrast, 3D seismic gives a tridimensional view of the underground structures, including the dimension of the injected plume of CO_2 [67, 70]. High – quality 3D imaging can detect CO_2 mass weighing more than 106 kg at 1 – 2 km depths, providing ideal results [70].

The Norwegian National Seismic Network (NNSN) at the University of Bergen monitors seismic activity in Norway. The NNSN is made up of 34 seismic stations located in Norway and on Norwegian Arctic islands. In the near future, NNSN will be expanded with permanent seabed stations to monitor oil and gas operations and seismic monitoring in the Aurora area for the Northern Lights project [71].

2.5.5 Downhole pressure and temperature measurements

Continuous pressure and temperature measurements of the CO_2 at the injection point are provided by downhole pressure and temperature sensors. The measurements are often recorded in a memory gauge for retrieval at specific intervals or broadcast to the surface operators through a fiber optic connection. These measures may be used to detect casing failure, which may result in CO_2 leakage, to accurately estimate injection rates, the viscosity, and the density of the injected CO_2, and to verify reservoir models [72]. Moreover, monitoring temperature changes can help identify flow pathways throughout the reservoir. For more trustworthy findings, mathematical models can be developed based on the geology of the storage area, the amounts of injected CO_2, and its interaction with the surrounding fluids [73].

The approach was employed at the Ketzin site in Germany on smart wells with various permanent downhole sensing devices, including a fiber – optic pressure and temperature gauge. The injection well and two observation wells are equipped with distributed temperature sensing equipment, which allows for the collection of semi – temperature profiles over the entire length of the wells [74]. Analyzing the observed temperature differences led to a better understanding of the flow dynamics within the wells and the phenomena associated with CO_2 distribution. The downhole sensor system also monitors reservoir pressure in real – time during the injection process and permits viewing and management of the well. High – resolution pressure measurements from an observation well at the SECARB project near Cranfield, Mississippi, were used to monitor reservoir behavior to increase CO_2 injection rates [75]. Downhole pressure and temperature data might be used with other CO_2 monitoring methods and be beneficial in alerting operators to leaks, prompting the deployment of more specialized CO_2 leakage measurement equipment.

2.5.6 Gravimetry methods

Gravimetric surveys are used to determine the density change in a formation. As a result, such monitoring may provide information regarding CO_2 distribution in a storage facility. Little perturbations in the local gravitational field can detect changes in underground density caused by CO_2 injection; a decrease in density is noticed when CO_2 displaces denser brine inside the reservoir. Monitoring these variations provides information on the rate of CO_2 migration. However, the distance between the gravimetric meters and the plume causes limitations. The plume's form also influences the results, with vertically elongated plumes producing a more significant signal than flat-spread plumes [70].

2.5.7 Chemical sensors in situ pH/pCO_2

Many chemical sensors on the market are designed to monitor the water concentrations of various chemical components that can be linked to CO_2 leakage. Because seawater naturally includes several chemical elements, including CO_2, at varying concentrations, these sensors must provide reliable results.

Shitashima and Kyo first developed an in situ pH/pCO_2 sensor in 1998 [76] and updated it in 2008 [77]. A pH electrode is an ion – sensitive field effect transistor (ISFET), and a reference electrode is a chloride ion – selective electrode (Cl – ISE) in a newly developed sensor. In situ pH sensor provides a quick response time (a few seconds), high accuracy (0.005 pH), and a

depth rating of 6000 m [61]. This pH sensor was subsequently used to help develop the pCO_2 sensor for in – situ pCO_2 measurements in saltwater. Figure 2.13 illustrates an overview of the in situ pH/pCO_2 sensor and a close – up of the pH and pCO_2 electrodes.

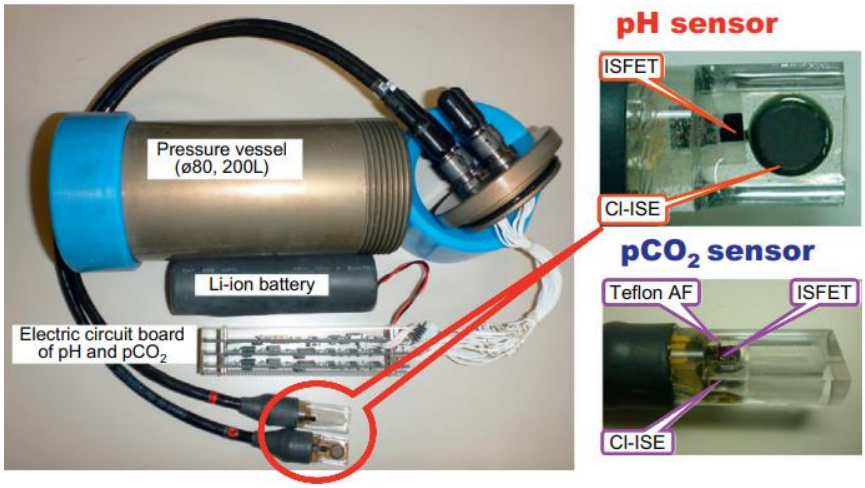

Figure 2.13: pH/pCO_2 sensor [61].

The pH/pCO_2 sensor was tested at 3000 m depth and 1.8 °C in the Mariana Trough basin and the Okinawa Trough at 1500 m depth and 4 °C [77, 78]. The results show that the sensor is an excellent instrument for in situ detection of pH and pCO_2 changes in the ocean environment.

According to modeling studies, the natural fluctuation of pH and pCO_2 in the North Sea ranged from less than 0.2 pH units in low biological activity regions to more than 1.0 pH units in high biological activity areas, and the effect of acidification caused by atmospheric CO_2 input was calculated to be 0.1 pH [79, 80]. HA. Botnen specified in his study 5 mol CO_2 per kilogram of seawater as an upper value for detecting rising CO_2 concentrations from subsea leakages [81].

2.5.8 Chemical tracers

J. Roberts proposed chemical tracers as an efficient method of detecting, attributing, and measuring any CO_2 leaks to the surface from geological CO_2 storage locations [82]. Chemical tracers, such as noble gas isotopes or radiogenic carbon, are preferred because they are easier to authorize and minimize the cost and dangers of obtaining and intentionally introducing a tracer. Yet, because of their unique composition and the ability to monitor and regulate concentrations, additional tracers provide more reliability. The most acceptable additional tracers are helium, xenon isotopes and artificial tracers such as perfluorochemicals (PFCs) and deuterated methane [82-84].

The main concept is to inject tracers with CO_2 at low concentrations where the tracers' interaction with CO_2 is limited. When a leak develops in the pipeline, the tracer ratio changes as CO_2 dissolves in the pore water of the sediment, and the residual gas becomes enriched in tracers; the tracer leakage ratio tells us how much CO_2 has dissolved in seawater [84]. By knowing the amount of tracer and CO_2 injected and the sampling and plume surface areas, the leakage rate of CO_2 can be estimated.

Tracer experiments were carried out in May 2019 as part of the STEMM – CCS project to provide methodology and technologies for effective environmental monitoring of offshore CCS sites [85]. The research tested performed near the depleted gas field Goldeneye in the North Sea, roughly 100 km Northeast of Aberdeen. During 11 days, a controlled mixture of CO_2 and tracer gases was delivered continuously into the shallow sediments 3 m below the seabed at a rate that gradually increased from 6 to slightly over 140 kg CO_2 per day. Consequently, the experiment effectively revealed that the approach could consistently identify emitted CO_2 from natural variability at low flow rates of roughly 18 kg CO_2 per day and high flow rates of around 140 kg CO_2 per day. Also, the concentration of emitted CO_2 that dissolved in the sampled seawater could be quantified. It can be concluded that with this method, even small leaks can be detected using existing measurement technology, even though seawater naturally contains a highly variable amount of inorganic carbon, which is difficult to distinguish from seepage CO_2.

2.5.9 Acoustic sensors

Autonomous underwater vehicles (AUVs) equipped with high – resolution imaging sonars may identify and observe seep – related characteristics on the seafloor, such as pockmarks, bacterial mats, or small topographical changes, which can help minimize the location of CO_2 leaks [79]. This allows the operating frequency range to be tuned to include the expected resonance frequencies of bubbles, optimizing their acoustic response, and using frequency – dependent information for leakage measurement. Figure 2.14 illustrates Kongsberg's Hugin AUVs, which can operate to 3,000 m, considerably above the ocean depths currently proposed for offshore CO_2 storage locations. Moreover, AUVs can be equipped with side scan sonar and multibeam echo sounders to improve mapping capabilities and resolution. Active sonar collects bathymetric data, with the collected reflections mapping the bottom topography. Due to the survey, high – quality images may be obtained, and small structures on a scale of 1 cm can be detected [62]. Even minor changes in morphology due to potential CO_2 seepage into the water column might be identified.

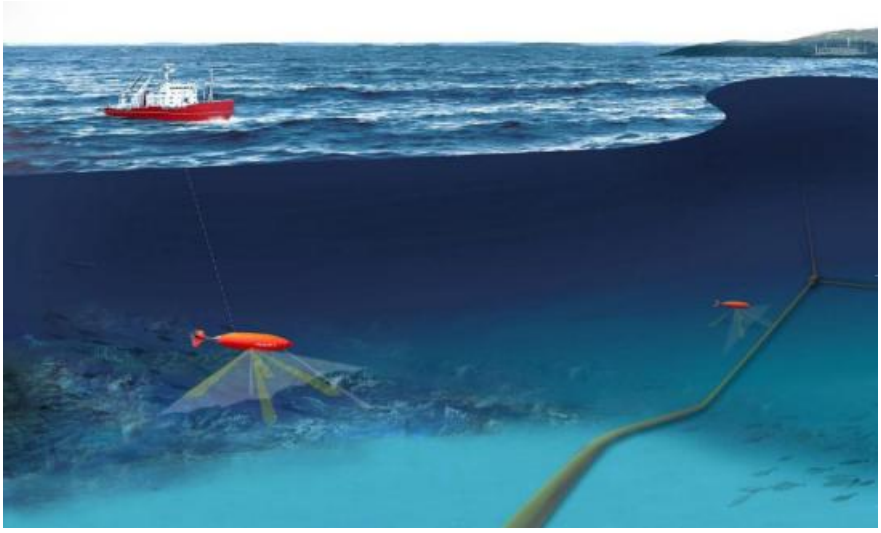

Figure 2.14: AUVs in operation [62].

Sonar systems have excellent sensitivity, particularly for gas, and have a significant potential for detecting subsea hydrocarbon leaks. P. Brewer illustrated the process by releasing CO_2 into the deep sea. The results showed that it could monitor the droplet cloud from the 1000 m CO_2 release for more than 30 minutes and more than 150 m of elevation, resulting in an average overall rise rate of roughly 5 m/min for the cloud [86].

K. Shitashima examined the REMUS 100 AUV produced by the Woods Hole Oceanographic Institution (WHOI) to identify the location of CO_2 leakage [61]. On the REMUS 100 platform, various in – situ chemical sensors have been installed. As a result, images of rising gas bubbles were taken with the AUV's side – scan sonar at the Taketomi underwater region, demonstrating the effective identification of rising gas bubbles from the seabed.

2.5.10 Seafloor – based acoustic tomography

The main working principle of the method is to deploy multiple transponders on the seabed so that sound may be relayed from one acoustic transponder to another [61]. If CO_2 leakage in the space between two acoustic transponders induces currents that flow upward from the seafloor acoustic dispersion, which could be due to the eruption of gas bubbles and droplets, temperature fluctuations, then the travel time of sound propagating between two acoustic transponders changes, allowing for the detection of leakages throughout the area. Considering sound travel time is crucial in such measurements, the detection periods at the seabed acoustic transponders must be synchronized. Figure 2.15 illustrates the prototype of the acoustic tomography transponder and the principle of the measurement.

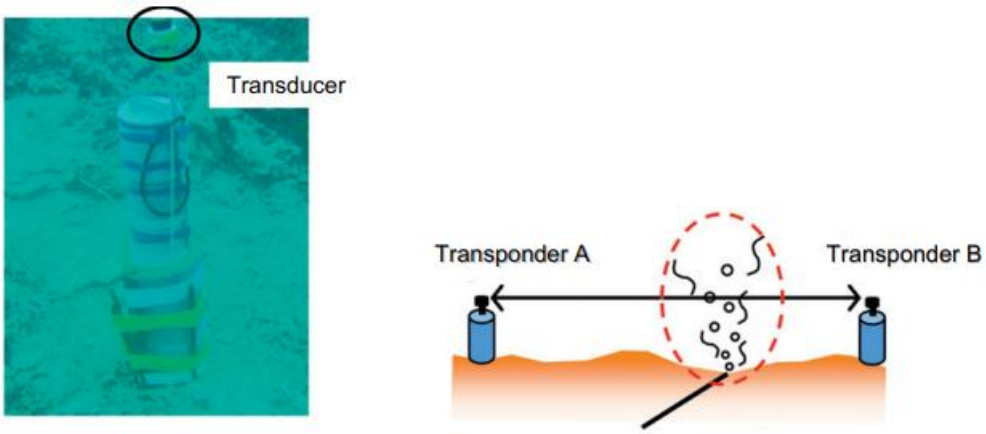

Figure 2.15: Acoustic tomography transponder and the principle of the measurement [61].

The approach was performed at the Taketomi subsea hot spring in Japan's southern Yaeyama Archipelago [87, 88]. Hot spring water with gas bubbles containing around 2 % CO_2 erupts from a depression 50 m in diameter on the seafloor in 20 m of water in this location. The density turbulence induced by hot spring water eruption and gas bubbles from the bottom was monitored using five acoustic transponders installed across a pentagonal region of 200 m in diameter centered on the subsea hot spring. The results demonstrated that this technology effectively identified and recorded the seabed hot spring water emerging from the bottom. In

other words, this system has the potential to detect density turbulence, temperature perturbation in this case, and acoustic dispersion, as well as CO_2 leakage in sub – seabed CCS.

Other approaches, such as subsea or onboard sonar, may have difficulty detecting and separating the bubbling sound from background noise. Additionally, subsea, and onboard sonar may identify gas bubble eruptions only while the research vessel is on the sub – seabed CCS site [61]. Real – time observation is not possible, unlike acoustic tomography.

2.5.11 Atmos Pipe method

Since 1995, Atmos International has been developing technologies to detect leaks from various types of pipelines, including CO_2 pipelines [89]. The sequential probability ratio test (SPRT) approach is used in the Atmos pipe and is effective for gas and liquid pipelines. The system may be customized to satisfy the sensitivity required for detecting a CO_2 leak on large, complicated pipelines by using flow and pressure data from control systems, including supervisory control and data acquisition (SCADA). The approach is applicable to large pipelines and networks and can operate in all conditions. When deployed offshore, Atmos Pipe is designed to account for the pipeline's hydraulic profile and the seawater outside the pipeline. Instead, the multi – method Atmos Wave Flow algorithm, which contains both a volume balance and a negative pressure wave (NPW) algorithm, can be employed.

2.5.12 Summary of other pipeline leakage methods

This section briefly presents other pipeline leak detection techniques based on information gathered from report presented by DNV GL [55, 90] and M.A Adegboye research study [91]. Table 2.4 represents a summary of leak detection methods and their short description.

Table 2.4: Summary of other pipeline leak detection methods [55, 90, 91]

Methods	Principle of Operation
Fibre Optics Sensing	The fibre – optic cable extends along the pipeline length or structure to be monitored. Detect leaks by identifying temperature variations in the line's optical quality caused by leaking.
Vapour Sampling	To detect trace amounts of certain hydrocarbon molecules, employ hydrocarbon vapor dispersed into the sensor tube.
Bio sensor	A live microorganism is used to detect the presence of pollutants. The biosensor's response is monitored by heart rate and the degree and frequency with which the clam is opened and closed.
Fluorescence	Proportionality between the amount of fluid discharged and the rate of light emitted at a particular wavelength. Employ a specific wavelength light source to raise the energy level of molecules in the target substance.
Optical camera	Video cameras are used to monitor the subsea system.
Volumetric collection	Volumetric measurements are used to detect leaks. When a specified volume is gathered, the system performs an action and generates an alarm.
Ground Penetration Radar	Use electromagnetic waves that are transmitted into the monitoring item by moving an antenna along a surface.
Negative Pressure Wave	Uses negative pressure waves caused by pressure reductions caused by leakage.
Dynamic Modelling	Detects leaks by comparing measured data to simulated values using conservation equations and the fluid's equation of state.
State Estimation	The missing variables are estimated using a set of algebraic equations that link a set of input, output, and state variables.

2.6 What is CO_2 storage?

CO_2 storage is the final step in the CCS chain; the idea is to isolate the CO_2 permanently from the atmosphere to avoid climate change. Therefore, geological locations suitable for CO_2 storage must be carefully selected. Basic requirements for geological CO_2 storage include suitable reservoir rock porosity, thickness, and permeability, a cap rock with good sealing capacity, and a stable geological environment [92]. Three key elements must be covered by summarizing: depth, location, and capacity.

Three different geological formations are usually considered for CO_2 storage: depleted (or nearly depleted) oil and gas reservoirs, unmineable coal beds, and saline aquifers. CO_2 can be injected into depleted (or nearly depleted) oil/gas reservoirs to increase their pressure and

provide the driving force to extract residual oil and gases [93]. In comparison, the process when CO_2 is injected into deep coal beds is called CO_2 – enhanced coal bed methane [94]. The purpose of the process is to recover methane which is trapped in the porous structure of coal seams. Lastly, injection of captured CO_2 into saline aquifers can be used for the CCS process.

Deep saline aquifers, which may be found both onshore and offshore, are considered to have enormous CO_2 storage capacity. As shown in the Figure 2.16 the depth has to be more than 1 km [95]; the reason is the behavior of CO_2. When CO_2 is stored in the rocks below this depth, the natural pressure and temperature earth compress the CO_2 to a dense phase. In this dense phase, CO_2 can be stored in significant amounts, and the movement of the CO_2 is minimum. It is buried under a layer of non – or low – permeability rocks that serve as a cap rock, preventing the fluid from rising to the surface [96].

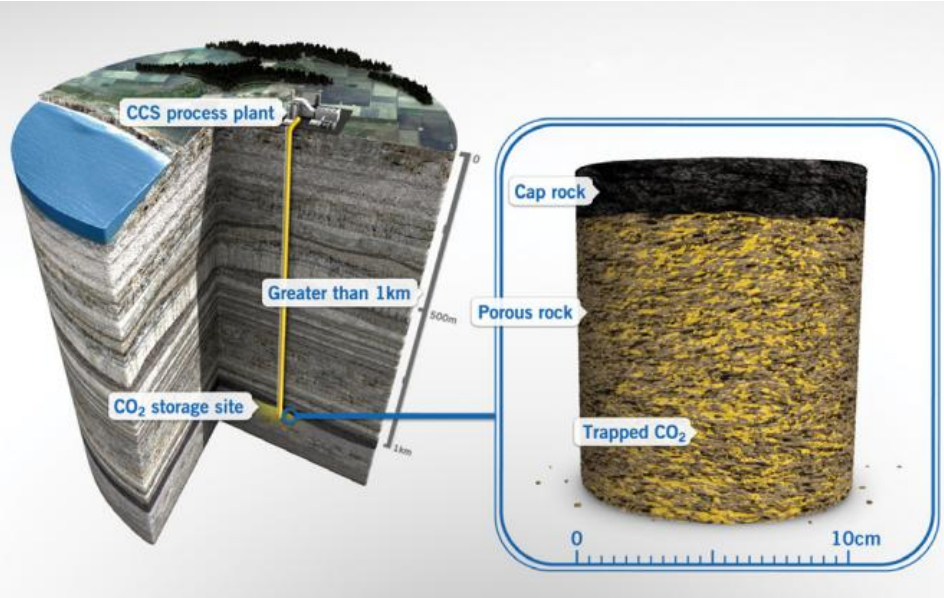

Figure 2.16: CCS plant overview and storage core sample [97].

It is estimated that the storage capacity of deep saline aquifers can reach up to 10000 Gt, for depleted oil and gas fields up to 900 Gt, and for unmineable coal seams up to 200 Gt [72]. Intergovernmental Panel on Climate Change (IPCC) has suggested that CO_2 storage must achieve rates of 10 Gt of CO_2 per year by 2050 to reach net zero for the global economy. Globally, cumulative CO_2 storage targets by 2100 have been identified by the IPCC to range between 348 Gt to 1218 Gt [98]. It means that storage locations for CO_2 will be in high demand.

2.7 International CCS projects

Several CO_2 storage and transportation projects are ongoing throughout Europe. For example, in Norway, there are two active CCS projects, Sleipner and Snøhvit, injecting at rates of about 1 million tons of CO_2 per year into saline aquifers which have been operational since 1996 and 2008 [99]. At the Port Jerome plant in France, CO_2 is captured from H_2 [100]. Another ongoing CCS project is OCAP in the Netherlands, where CO_2 is collected from industrial sources and

delivered to greenhouses [101]. Most CCS projects are located in the United States, with a combined capacity to capture more than 25 million tons per annum [102].

In addition, several CCS projects are being developed that connect onshore capture facilities to offshore geological storage locations. These include Northern Lights (Norway), Porthos and Athos (Netherlands), ERVIA (Ireland), ACORN and HyNet (UK), Carbon connect Delta (Belgium), ANRAV (Bulgaria), Preem CCS and Slite CCS (Sweden) etc. [103]. Several of these new projects plan to start transportation and injection activities well before 2030 and are designed to operate at a scale of 1 million tons of CO_2 captured annually.

Carbon dioxide emissions can be reduced or removed from the atmosphere. CCS is the method to remove CO_2 from the atmosphere, where emissions are permanently stored underground for a very long time. However, for a reduction term, carbon dioxide is used to make things such as building materials (utilization) or in the production of fuels and chemicals. Technology that combines carbon capture, utilization, and storage is known as CCUS. The term "CCUS" refers to a group of technologies that capture CO_2 from significant point sources, such as industrial or power plants that burn either fossil fuels or biomass as fuel [104]. Another option is to capture CO_2 directly from the air. The captured CO_2 is compressed and further injected into deep geological formations (like depleted oil and gas reservoirs or saline formations) that trap the CO_2 for long – term storage. Then, it is delivered by pipeline, ship, rail, or truck to be used in various applications. For CCUS facilities, using CO_2 for industrial purposes potentially results in a source of revenue. There are numerous other possible applications for CO_2, such as a feedstock for manufacturing synthetic fuels, chemicals, and construction materials. Until now, the great majority of CCUS projects have relied on income from the sale of CO_2 to oil companies for enhanced oil recovery (EOR) [105].

Figure 2.17 illustrates the list and map of existing and planned CCUS projects in Europe. Projects listed in bold are in operation. The total number of projects is 72. According to the report presented by IOGP (International Association of Oil & Gas Producers), around 80 million tons of CO_2 per year will be stored by 2030 [103].

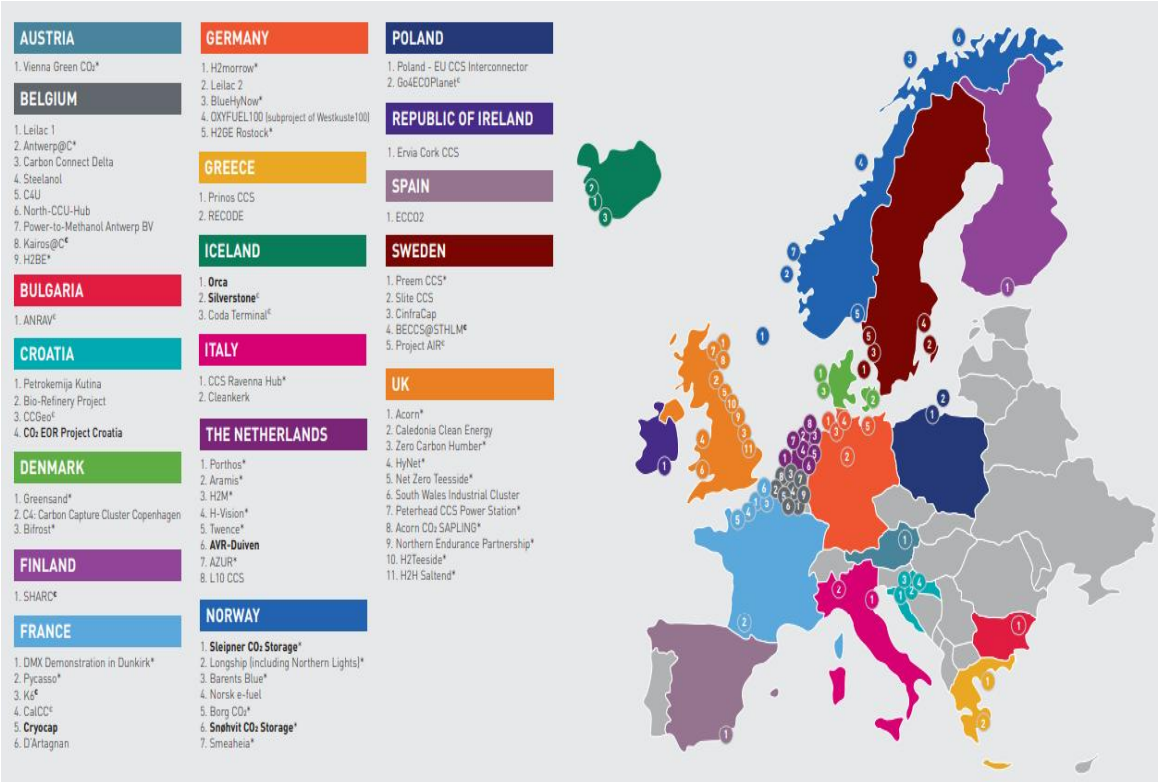

Figure 2.17: Overview of existing and planned CCUS facilities [103].

2.8 CCS projects in Norway

2.8.1 MACON CCS

MACON CCS is a project coordinated by SINTEF Energy Research, which includes industry partners such as TechnipFMC, Roxar, KROHNE, and Norsk Elektro Optikk. The project's duration is from 2021 to 2025, and it aims to help CCS become a widely used and efficient climate policy tool. The research focuses on demonstrating sensor capabilities for CCS and flow experiments to advance the development of dynamic simulation models to transport pure CO_2 and with impurities under different operational conditions [106, 107].

MACON CCS will fill gaps in thermodynamic data on species that, even at low concentrations, can significantly impact phase behavior and develop efficient and robust thermodynamic models. The thermodynamic models and sensor expertise will be used to design leak detection and mass balance concepts for intelligent monitoring and control systems. In addition, CO_2 network flow assurance and operability issues will be investigated. MACON CCS's scientific results have the potential to enable large – scale deployment of CCS from industrial sources, as well as the long – term business case of the Norwegian large – scale project for CO_2 transport and storage infrastructure, such as Northern Lights [106].

2.8.2 The Northern Lights

The Northern Lights project is the Norwegian full – scale CCS project, resulting from the Norwegian government's ambition to establish a full – scale CCS value chain in Norway by 2024. The project is ongoing in a partnership between Equinor, Shell, and Total. It can store 1.5 million tons annually, planning to increase capacity as demand rises throughout Europe.

Northern Lights will receive captured CO_2 from Oslo Fortum Varme and Norcem in Brevik. The pipeline transporting CO_2 from the onshore facility to the storage location is designed to transport up to 5 million tons of CO_2 annually. However, Norcem and Fortum Oslo Varme will only use 0.8 of the 1.5 – million – ton capacity, which is about 53 % at the onshore facility in Naturgassparken. As a result, up to 700 000 tons of spare capacity per year may be utilized to store CO_2 from other capture companies. In addition, there has been extensive discussion with possible foreign suppliers of CO_2 for permanent storage as part of the Northern Lights project. In September 2019, seven international industrial companies and Equinor signed an agreement to deliver and store CO_2 on the Northern Lights [71].

As seen from the Figure 2.18, captured CO_2 will be transported from two facilities in the liquid phase, then shipped to an onshore facility on the Norwegian West coast. From there, the liquefied CO_2 will be transported by pipeline to an offshore storage location in the North Sea for permanent storage 2500 meters below the seabed [108].

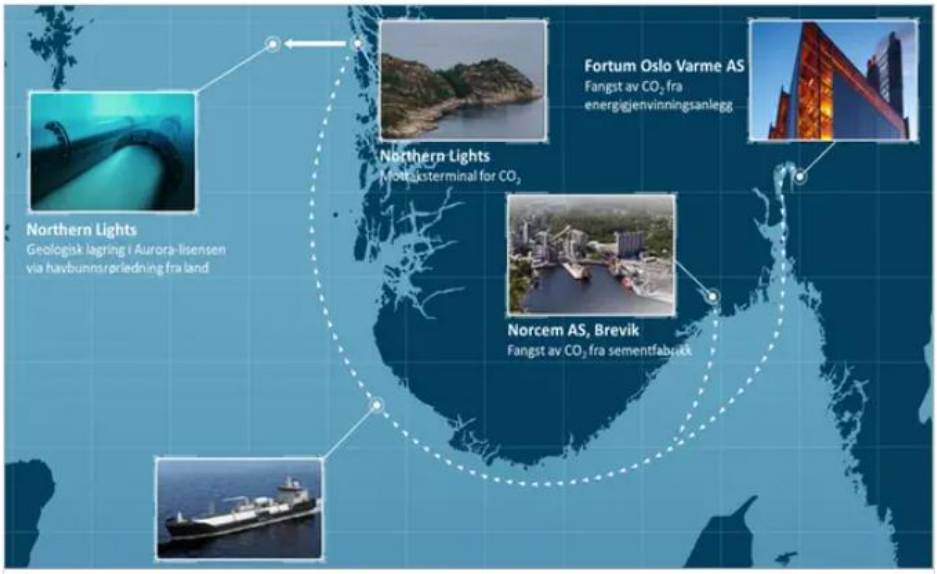

Figure 2.18: Northern Lights CCS chain [109].

The project will be carried out in 2 phases. Phase 1 includes the capacity to transport, inject and store up to 1.5 million tons of CO_2 annually with an operating period of 25 years. From the CO_2 capture facility, liquefied and pressurized CO_2 will be loaded onto ships and transported to the Northern Lights onshore terminal at Naturgassparken in Norway. CO_2 will be transferred from the ships to onshore intermediate storage tanks at the terminal. Then it will be pumped via pipeline to a subsea structure at the seabed and injected into a geological formation [110]. The project has completed the FEED (Front End Engineering Design) phase for this phase and

got a license from the Norwegian government to inject CO_2 into their designated reservoir, which is called Aurora.

Implementation of Phase 2 depends on the market demand for more CO_2 storage. Phase 2 is expected to have a capacity of up to 5 million tons of CO_2 annually, with realization dependent on access to CO_2 under contract for geological storage [108]. An approximately 100 – km – long pipeline will be installed from the onshore facility to the injection well, which will be jetted into the seabed in the fishery – intensive area southwest of Troll A. The pipeline's transport capacity is enough to accommodate the project's Development Phase 2 [111].

The port for receiving CO_2 on ships must be secured within the archipelago to allow reasonable access for the planned large number of port calls. Factors such as wind, waves, and swell on the approach to the port and the pier are crucial to ensuring high regularity and safety in all operating scenarios. Figure 2.19 shows that apart of Naturgassparken 18 locations have been evaluated along the coast, from Kårstø to the South and Lutelandet to the North. Location of choice is highlighted in red.

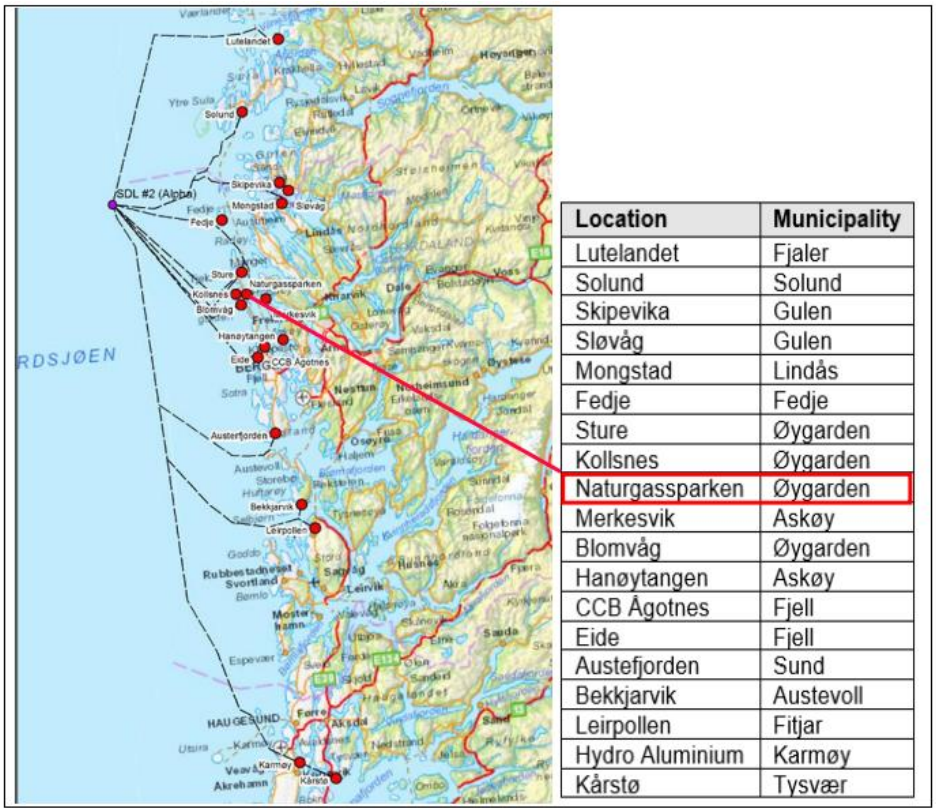

Location	Municipality
Lutelandet	Fjaler
Solund	Solund
Skipevika	Gulen
Sløvåg	Gulen
Mongstad	Lindås
Fedje	Fedje
Sture	Øygarden
Kollsnes	Øygarden
Naturgassparken	Øygarden
Merkesvik	Askøy
Blomvåg	Øygarden
Hanøytangen	Askøy
CCB Ågotnes	Fjell
Eide	Fjell
Austefjorden	Sund
Bekkjarvik	Austevoll
Leirpollen	Fitjar
Hydro Aluminium	Karmøy
Kårstø	Tysvær

Figure 2.19: Map of expected locations for an onshore facility for CO_2 storage [71].

Four potential locations, including Naturgasparken, Skipevika, Mongstad, and Sture, were chosen for a more thorough review in Phase 2 [71].

2.8.3 Snøhvit

CO_2 storage at Snøhvit started in April 2008 by injecting into the Tubåen formation at a depth of around 2600 – 2700 m below the sea surface [112]. The Snøhvit unit consists of three major gas fields, Snøhvit, Albatross, and Askeladd fields, which were discovered in 1984, 1982, and 1981, respectively. The Snøhvit Liquified Natural Gas (LNG) project is the first oil and gas development project in the Barents Sea and the first LNG – based gas field in Europe [113].

The field consists of a fully subsea offshore development in the Barents Sea, a 160 – kilometer pipeline to shore, and a liquification plant for LNG. The separation of carbon is necessary for the LNG process, and the plant includes an installation to capture CO_2 from natural gas. Furthermore, a 160 km pipeline has been built back to the field to store 0.7 million tons of CO_2 annually [114]. Approximately 12 GSm^3 or 23 million tons of CO_2 will be removed and deposited from the well stream during the Snøhvit LNG project's 30 – year lifespan [115]. The separated CO_2 is then dried and recompressed to ensure that free water does not form and that the CO_2 remains in the liquid region during transportation [116].

Until April 2011, CO_2 was injected into the Tubåen Formation, which is dominated by fluvial sandstone. After some time, the pressure increased more quickly than expected, requiring a method to prevent the seal from fracturing. The injection into the Tubåen Formation was stopped in 2011, and the shallower Stø Formation was perforated as the new Formation for CO_2 storage. All CO_2 from the Snøhvit Field was injected into the water zone of the Stø Formation [116]. On the field, 16 wells have been drilled, 14 producers, and two wells for CO_2 re – injection [117]. The Snøhvit CO_2 transportation and injection system consist of around a 153 – kilometer – long pipeline with a 200 – mm ID (inner diameter) that operates at pressures ranging from 80 to 140 bar [118].

In December 2022, Equinor submitted a plan for development and operation for Snøhvit Future to the Minister of Oil and Energy in Hammerfest. According to it, it planned to invest NOK 13.2 billion (2022) to upgrade the plant with gas compression and electrification [117]. Onshore gas compression will provide sufficient reservoir supply to continue plateau production and maintain high LNG gas exports beyond 2030. In addition, electrification will reduce the emissions from LNG production, leading to a CO_2 emissions reduction of about 850 000 tons per year.

2.8.4 Sleipner

Since 1996, Equinor, as an operator, and several partnering companies have operated the Sleipner field in the Norwegian North Sea as a facility for carbon capture and storage. This is the world's longest running CO_2 storage project. CO_2 separated from the Sleipner vest’s and the Gudrun field’s natural gas and injected into the Utsira Sand, a significant saline aquifer [119]. CO_2 is injected through a single near horizontal well (Figure 2.20) at a depth of approximately 1012 m below sea level. Around 1 million tons of CO_2 is captured from natural gas and stored at Sleipner annually [120].

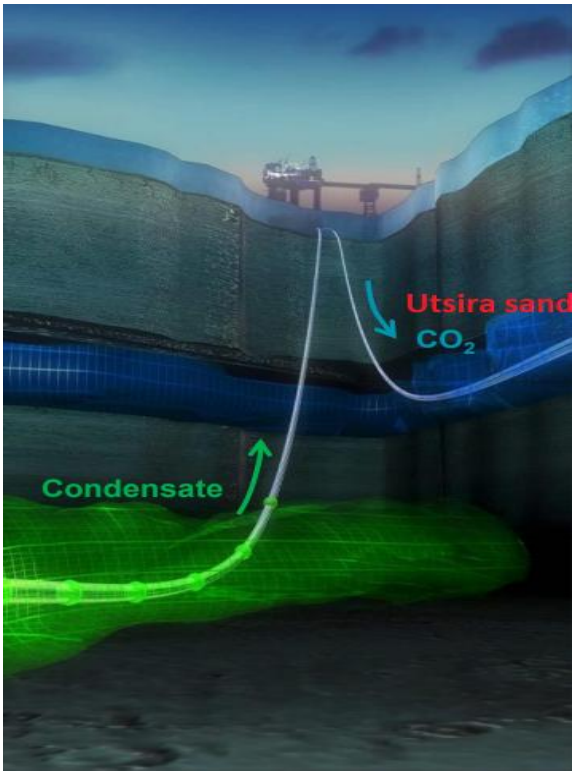

Figure 2.20: Representation of the Sleipner CO_2 injection operation [121].

The Utsira Formation is estimated to store 600 billion tons of CO_2 and covered by a thick layer of shale rock, preventing CO_2 from migrating upwards [122]. In terms of long – term preservation, the injected CO_2 will be stored in the Utsira sandstone for thousands of years, like natural gas and oil stored for millions of years in similarly deep geological formations.

The injected CO_2 is in a two – phase flow condition, with a single liquid phase maintained at the well's bottom section and containing up to 2 % methane [123]. The injection well is highly deviated, with an angle of 83 at the injection point. CO_2 is injected directly from the platform into the well without subsea installations. The wellhead temperature is mostly about 25 °C, and the wellhead pressure is from 63 to 66 bar. The bottom hole temperature and pressure could vary from 90 to 140 bar and 49 °C to 51 °C, respectively [124].

For the last decades, the Sleipner project was a first – hand experience of safely storing CO_2 in a reservoir and stepping into the future decarbonization path. For the past 15 years, Equinor has shared CO_2 storage and monitoring data with the research community [125]. Sharing data and experience from the very first CCS project played a vital role in the development of future projects. Such as improving reservoir characteristics, understanding flow processes, developing new technologies, verification, and prediction. The CO_2 Storage Data Consortium was founded in 2017 as an international network to make datasets for CO_2 data exchange available to everyone, and it was opened for public access in 2020 [126]. From 2023 CO_2 Datashare is part of the NCCS (Norwegian CCS Research Centre). The value of the Sleipner project is unique and will continue to be used to strengthen and build up CCS globally.

2.8.5 Barents Blue

The Barents Blue project is an ammonia production facility cooperation project with Horisont Energi, Equinor, and Vår Energi. The project is planned to start operation in 2026. The project's concept is to use natural gas from the Barents Sea to produce ammonia. It will be Europe's first large – scale clean ammonia manufacturing facility in Finnmark, Northern Norway [127]. Figure 2.21 demonstrates illustration of the plant.

The plant will specifically manufacture blue ammonia from blue hydrogen, which will be generated at a rate of 600 tons per day from clean water and natural gas. In addition, CO_2 will be captured in high quantities during synthesis with nitrogen extracted from the air. The production of ammonia is expected to be up to 3000 tons per day. Annual output will be between 1 and 3 million tons by 2030 [128].

Polaris is also planned to become the Norwegian shelf's second commercial CO_2 storage reservoir. The project will capture carbon throughout the manufacturing process and permanently store it in the Polaris reservoir. Approximately 2 million tons of CO_2 will be injected into the reservoir for storage [128]. The reservoir's estimated storage capacity is more than 100 million tons [127].

Figure 2.21: Illustrative picture of the operational zone of the plant [129].

By the middle of 2023, the project will complete the FEED (Front End Engineering Design) phase. Then until the year 2025, it has the Civil & Construction phase. And as it has been mentioned earlier, the operation phase starts in 2026 [129].

2.8.6 Norsk e – fuel

The Norsk e – Fuel project's main idea is not CO_2 storage but the usage of captured CO_2. The project aims to create synthetic, renewable aviation fuel from CO_2 and H_2. Captured CO_2 will be provided by Climeworks, the company that captures CO_2 directly from the atmosphere through direct air capture technology. To manufacture H_2, electrolysis will be used from H_2O using 100 % renewable electricity [130].

This alternative fuel will allow travel using current infrastructure without negatively impacting the environment. The project will effectively reduce the present flight emissions of Norway's top five most frequently served air routes by around 50 % [131].

The first e – Fuel facility is planned to be built in Mosjøen, Norway, in 2023. By the end of 2024, the first manufacturing line will be completed, producing 12.5 million liters of renewable fuel annually. The factory will achieve total capacity in 2026, doubling output volume to 25 million liters per year. A plant with a production capacity of 100 million liters per year will be developed till 2029 [130].

In addition to the Mosjøen Industrial Zone, the plant will be in Herøya Industrial Park, 150 kilometers south of Oslo. Other places in Norway's north are being investigated, including suitable collaboration with governmental and industrial partners along the supply chain.

2.8.7 Borg CO_2

Borg CO_2 is a company working with 18 partners to develop CCS technology, particularly for industrial facilities near Viken (Østfold), Norway. The project aims to build a CCS cluster at the port of Borg with a CO_2 capture capacity of 630 000 tons per year from 5 industrial facilities [132]. Emissions will be stored from industrial facilities in Fredrikstad, Sarpborg, and Halden (Figure 2.22).

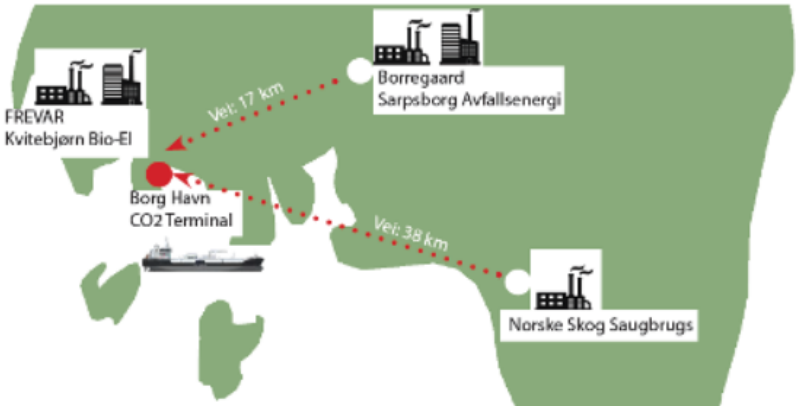

Figure 2.22: CCS cluster at Borg CO_2 terminal [132].

CO_2 will be transported to the Borg terminal through onshore pipelines, where it will be liquefied and loaded onto ships for further storage at the terminal at Øygarden on the Norwegian west coast. Borg CO_2 and Northern Lights are collaborating in the project, so captured CO_2 will be injected into the Aurora aquifer for long – term storage through a 100 – kilometer pipeline [133].

It has been studying the possibilities of building CCS for an industrial cluster since 2018 and completed a full feasibility assessment in June 2021 [134]. Borg CO_2 completed a pre – FEED phase and expected to be in operation in the first half of 2026 [135].

2.8.8 Smeaheia

The Smeaheia project is another full – scale CCS project in Norway operated by Equinor, which might serve as a CO_2 storage site. In 2022, Equinor was awarded the license to develop CO_2 storage in the Smeaheia field [136]. The Smeaheia area is located east of the Troll field in the Bjørgvin Arch and Stored Basin in the Northern North Sea. The field includes two central structures, Alpha, and Beta, with a storage capacity might be around 100 Mt each, and the primary reservoir sandstone is the Sognefjord Formation [137].

The transport ships will transfer cold, pressurized, and liquid CO_2 from two facilities such as the Norcem cement factory in Brevik and the EGE Energy recovery plant (see Figure 2.23) in Oslo, to a receiving and intermediate storage facility on land in western Norway. Yara ammonia factory in Herøya in Porsgrunn withdrew from further work in the spring of 2018 [71]. Cold and liquid CO_2 is intermediately stored onshore before being transported by pipeline transportation to a subsea injection site at Smeaheia.

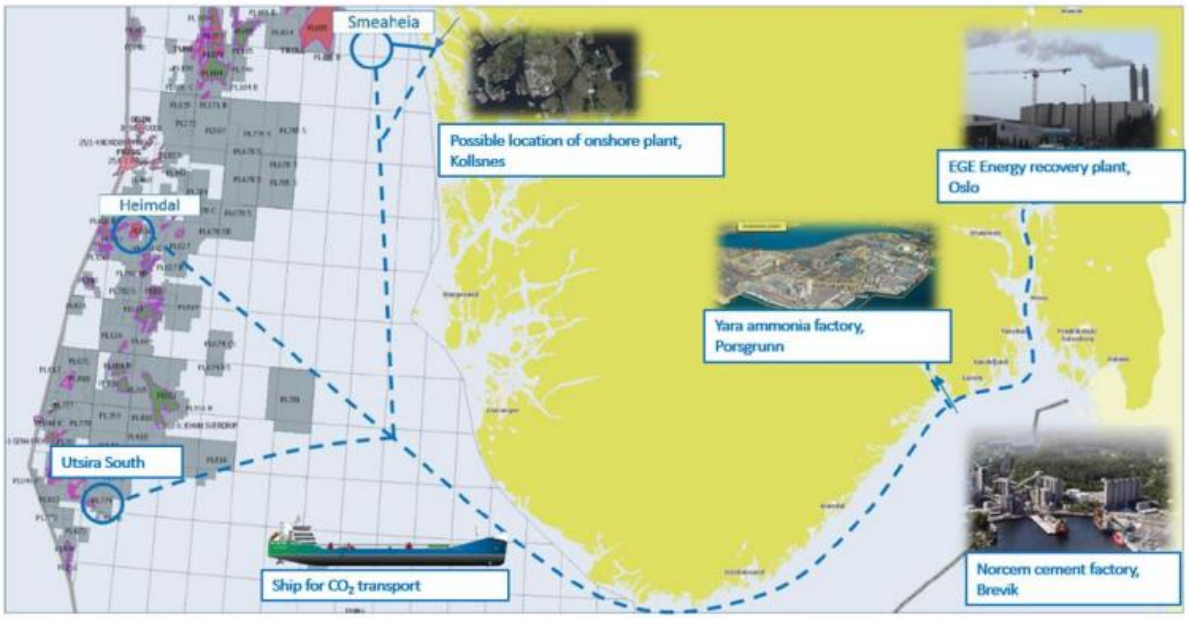

Figure 2.23: CO_2 chains considered in the feasibility study of the Smeaheia field [71].

The operation start of the project is still being determined since the field needs more subsurface work and confirmation to establish the reservoir segment's presence and quality with leakage risk analyses. In addition, the facility scope is impacted since the new location is further away from Naturgassparken, and the reservoir pressure is more significant owing to increased reservoir depth [33]. The long – term production of enormous amounts of oil and gas from the Troll field has lowered pressure in the Troll reservoir. Pressure connection between the Troll reservoir and Smeaheia is therefore quite likely. This also implies that Smeaheia's reservoir pressure may decrease over time [71].

Equinor and Gassanova developed a reference dataset for the Smeaheia field that includes subsurface data, reports, and geomodels related to the assessment of a proposed CO_2 storage site and is now publicly available online via the digital portal CO2DataShare [138].

3 PVT properties of CO_2

This chapter gives an overview of carbon dioxides PVT parameters such as pressure, temperature, density, viscosity, and enthalpy. The pure concentration of CO_2 was compared to impurity – containing CO_2. The software Multiflash and Thermopack were used to perform simulations for research analysis. The calculated viscosity parameter was compared to experimental data from previously published research. The primary goal of this review has been to investigate the PVT characteristics of CO_2 during injection and transportation operations and its phase diagram with critical and triple points, differentiate between three existing CO_2 phases and determine the influence of impurities on the phase envelope.

3.1 Phase diagram of pure CO_2

Pure CO_2 is CO_2 without impurities. Understanding the physical properties and behavior of CO_2 will improve safe and long – term CO_2 storage. CO_2 is an odorless and colorless gas at room temperature and atmospheric pressure. CO_2's physical properties will vary with pressure and temperature, causing a change in the phase diagram (Figure 3.1) which was built by using the software Multiflash. The phase diagram for CO_2 shows the transition between the different physical phases. It can also explain the thermodynamics of phase transitions between the solid, liquid, and gaseous phases of CO_2.

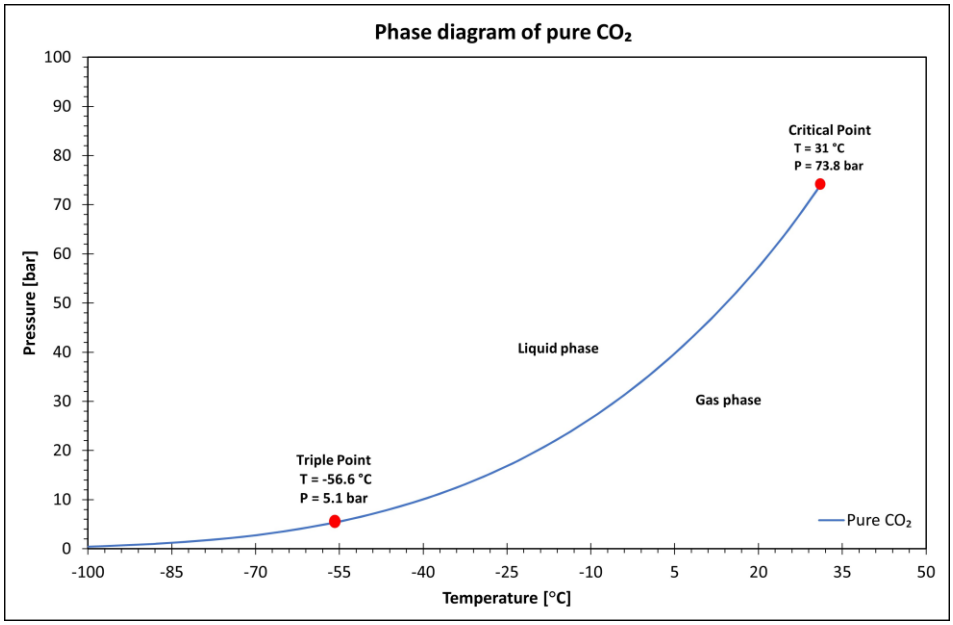

Figure 3.1: Phase diagram of pure CO_2.

As the phase diagram shows, pure CO_2 does not have a two-phase region; below the line, it is present in gas form, while above the line is in liquid form. CO_2 may be turned from a gas into a liquid by compressing it to the corresponding liquefaction pressure [72]. The phase diagram has two important points: the triple and critical points. The point at a low temperature of

-56.6 °C and pressure of 5.1 bar is called the triple point, where CO_2 is in the solid form, acting like snow or dry ice, and liquid and gas coexist. The critical point is located at a temperature of 31 °C and a pressure of 73.9 bar. Above the point, CO_2 presents in a supercritical phase with properties between gas and liquid with low viscosity, such as gases, and high density, like liquids.

3.2 Effect of impurities in CO_2

Captured CO_2 brought into a pipeline may contain impurities that result from the energy conversion and capture process. The type and amount of impurities introduced in the CO_2 depend on the fuels used and the type of capture process. The major impurities in captured CO_2 are H_2O, H_2S, O_2, H_2, CH_4, N_2, Ar, NO_x, SO_x, CO. Unfortunately, impurities in the CO_2 stream negatively affect the transport, injection, and storage of CO_2. For example, non – condensable impurities such as N_2, O_2, and Ar would increase the saturation pressure of liquid CO_2 and decrease the critical temperature. As a result, lower temperatures and additional overpressure are required to avoid two – phase flow in CO_2 pipeline transport. Non – condensable impurities would also increase the injection pressure and reduce the capacity of the storage sites by decreasing the density of the CO_2 stream. Moreover, acid impurities like SO_x and NO_x can react with formation and cap rocks and affect the injectivity and storage integrity [6]. Furthermore, the outcome of dangerous pollutants, which may be released into the environment in the case of CO_2 leakage, is of particular concern.

The amount and type of impurities must be known to ensure the safe and effective transportation of CO_2. Pipes, valves, measuring instruments, pumps, injection, and well equipment throughout the receiving, intermediate storage, export, and injection chain must be planned and built using materials suitable for the physical and chemical properties of the expected CO_2 composition. It will help to minimize corrosion and material quality degradation in the receiving, process, transport, and injection systems [139, 140].

The integrated European project DYNAMIS and the National Energy Technology Laboratory (NETL) have released studies with suggestions for the most aggressive impurity limits to be applied from both storage and transportation perspective [139], [141]. The recommendations' limits presented in the Table 3.1 are based not only on the risk of corrosion and the production of corrosive phases but also on HSE (toxicity limits) and reservoir requirements.

Table 3.1: Recommendations for maximum impurity concentration in captured CO_2.

Impurities, ppmv	DYNAMIS	NETL
H_2O	500	500
H_2S	200	100
CO	2000	35
O_2	< 40 000	40 000
N_2	< 40 000	40 000
H_2	< 40 000	40 000
NO_x	100	100
SO_x	100	100

The CO_2 concentration must be greater than 95.5 % [139].

3.3 Phase diagram for CO_2 with impurities

In this subsection, analyses performed for binary and ternary CO_2 mixtures are illustrated in Table 3.2 and Table 3.3. The concentration and type of the impurities have been selected for comparative and study purposes to illustrate how major impurities impact the phase envelope and critical points. Phase behaviors of CO_2 mixtures are based on the Vapor – Liquid Equilibrium (VLE) and critical points of mixtures. Therefore, the predictions of VLE are essential to designing and operating CO_2 mixture pipelines.

Table 3.2: CO_2 with nitrogen.

Component	Concentration mol %
$CO_2 + N_2$	90 + 10
$CO_2 + N_2$	80 + 20
$CO_2 + N_2$	70 + 30

Table 3.3: CO_2 with methane and nitrogen.

Component	Concentration mol %
$CO_2 + CH_4 + N_2$	90 + 5 + 5
$CO_2 + CH_4 + N_2$	80 + 10 + 10
$CO_2 + CH_4 + N_2$	70 + 15 + 15

Figure 3.2 shows the binary mixture of CO_2 with nitrogen with different mole concentrations built in Multiflash using GERG – 2008 EoS. For comparison reasons, pure CO_2 also have been added. It can be seen that the critical temperature and pressure of the mixtures are quite different from that of pure CO_2. As the phase envelope shows, the higher the nitrogen concentration in CO_2, the larger the phase envelope, implying a more comprehensive range of two – phase flow regimes. In addition, the pressure at the critical point increases depending on the nitrogen concentration in the captured CO_2. The higher the concentration, the higher the pressure. For each scenario with different nitrogen concentrations, the critical temperature drops by over 10 °C compared to pure CO_2.

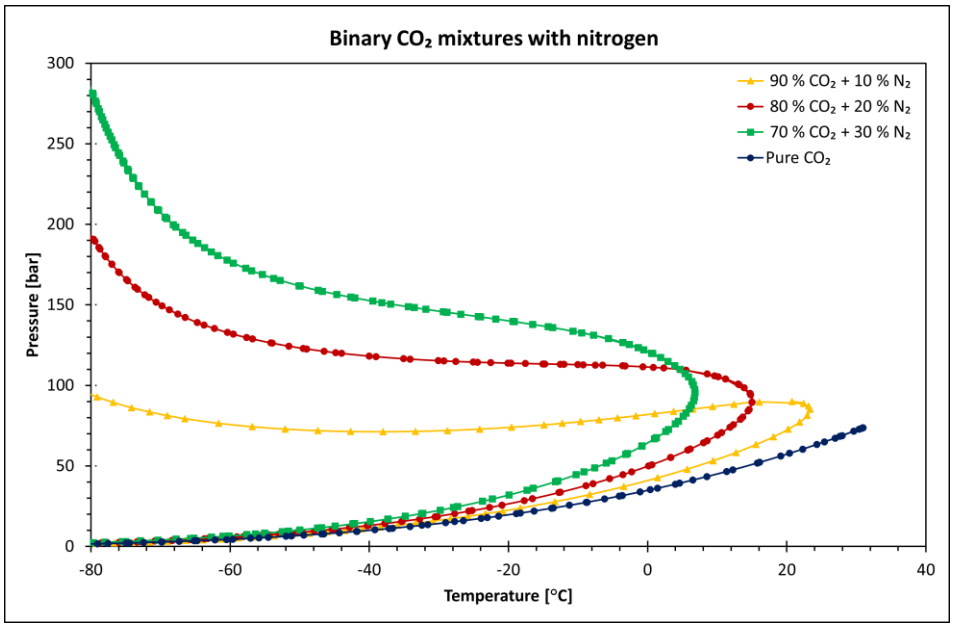

Figure 3.2: Phase diagram of pure CO_2 and binary CO_2 mixtures.

Figure 3.3 represents analyses for ternary CO_2 mixtures with nitrogen and methane with different mole concentrations. It can be concluded from the pattern of the phase envelope that the more impurities, the wider the range of the two – phase flow regime. As a result, escaping a two – phase flow while injecting and transferring CO_2 in pipes would be challenging since

the presence of impurities shifts the boundary of the two – phase area towards higher pressures, requiring higher operating pressures to maintain CO_2 in the dense phase.

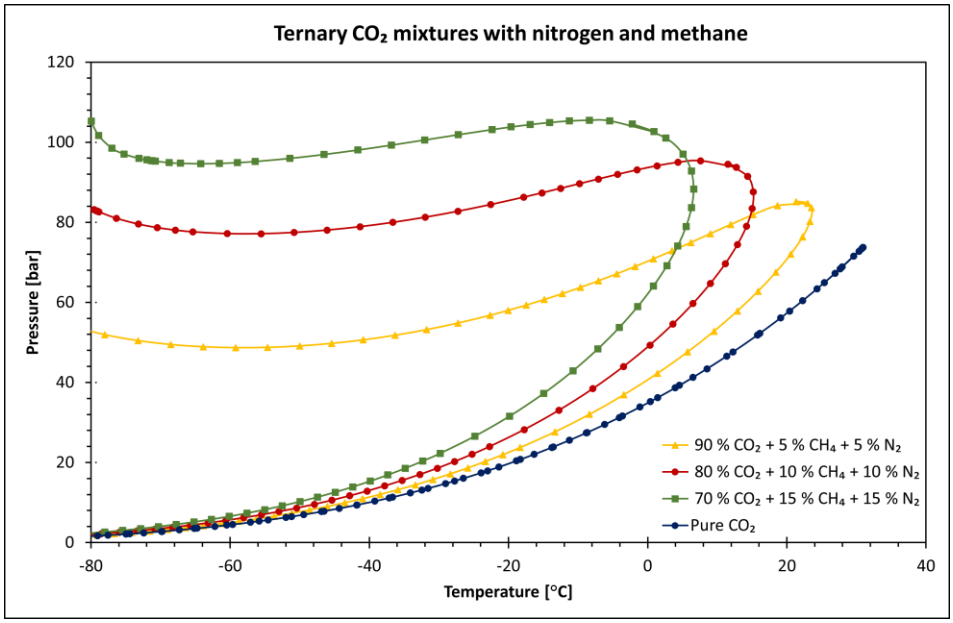

Figure 3.3: Phase diagram of pure CO_2 and ternary CO_2 mixtures.

3.4 Density

3.4.1 Density of pure CO_2

The density of CO_2 is another essential parameter in determining whether CO_2 has a high density and is in a dense phase or is lighter in a gas phase. The information is also helpful during transportation since the diameter and type of pipelines are chosen based on it. Knowing the volume of CO_2 is also beneficial for the optimum use of storage facilities. The efficiency of CO_2 storage in geological sites, defined as the amount of CO_2 stored per unit volume, increases with high CO_2 density. Study analyses were done in Multiflash to better understand density change as a function of temperature and pressure.

The density of pure CO_2 changes as a function of pressure in isothermal cases with temperatures of 5 °C, 20 °C, and 35 °C, as shown in Figure 3.4. The pressure was selected from 0 to 210 bar. It can be observed that an increase in temperature causes a decrease in density. In addition, the range of the two – phase flow regime is considerably smaller than the cases where the temperature is lower. Above the critical pressure of 73.9 bar and at temperatures lower than 20 °C, CO_2 would have a density between 930 to 1005 kg/m^3.

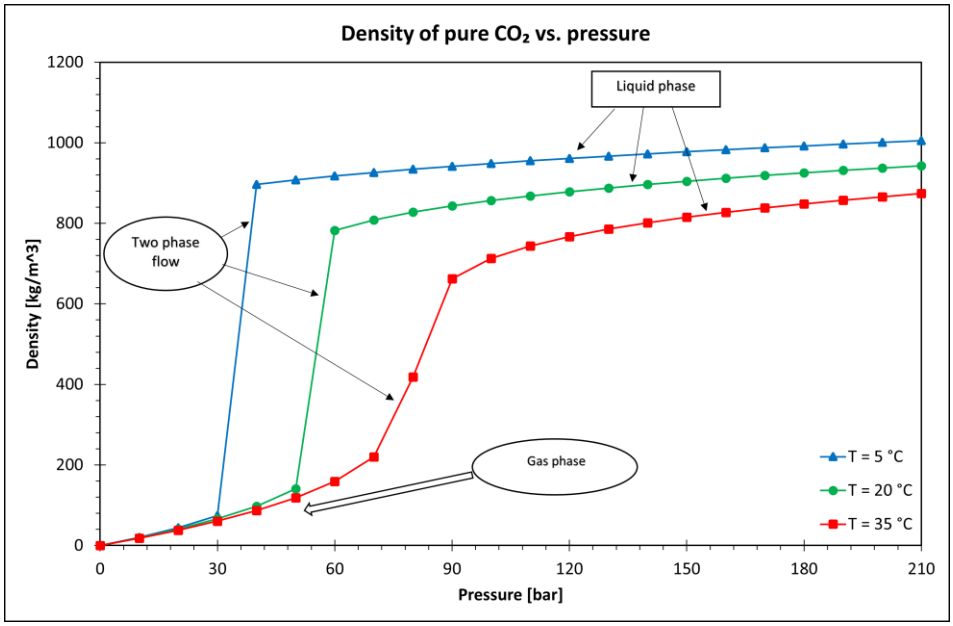

Figure 3.4: Density of pure CO_2 as a function of pressure.

While transporting CO_2, a higher density is advantageous since it is favorable to transport CO_2 in a dense phase [142]. Moreover, the dense phase has a viscosity similar to a gas but a density closer to that of a liquid. The liquid's density is comparable to that of water, 1000 kg/m^3.

Figure 3.5 represents the change in the density of pure CO_2 as a function of temperature at isobaric pressures of 40, 80, and 120 bar. Temperature ranges from -5 °C to 40 °C. The graph demonstrates that raising the pressure causes the density to rise.

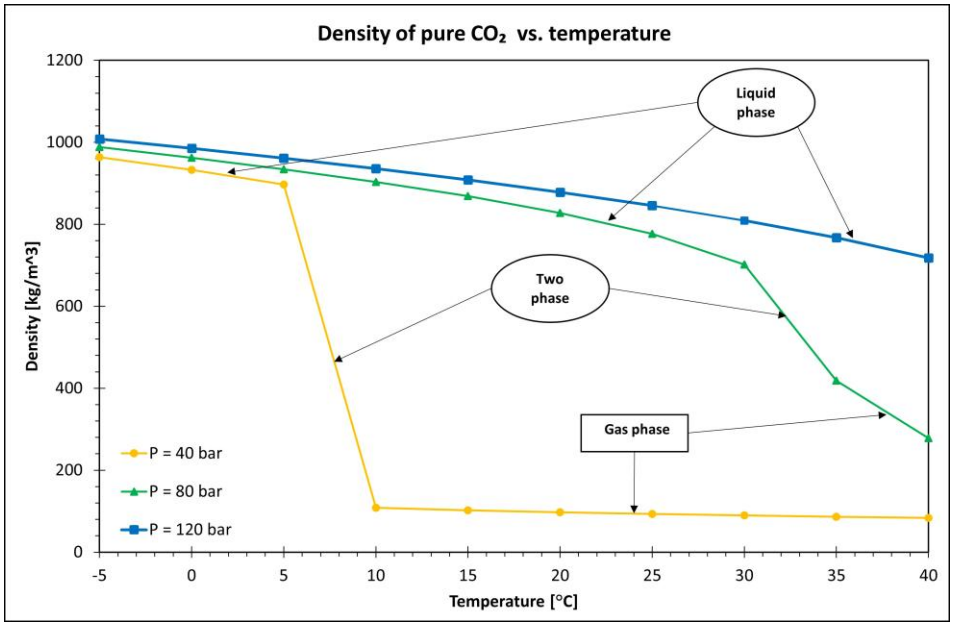

Figure 3.5: Pure CO_2 as a function of temperature.

Looking at the scenario with a pressure of 120 bar, it is clear that CO_2 will exist in just one phase: liquid. As previously stated, the dense phase is the most advantageous CO_2 transporting phase. In addition, the two – phase flow regime will be avoided. When the pressure reaches 80 bar, it is not recommended to raise the temperature over 30 °C since this results in a two – phase flow regime and significantly reduces the density of CO_2. When the pressure reaches 40 bar, keeping the temperature at 5 °C or even less is preferable.

3.4.2 Density of CO_2 with impurities

The presence of impurities in the CO_2 will affect the volumetric properties of injected CO_2. The Figure 3.6 shows the density vs. pressure graph for pure CO_2 and CO_2 with impurities, 10 % methane, for isothermal cases with temperatures 5 °C (a), 20 °C (b), and 35 °C (c).

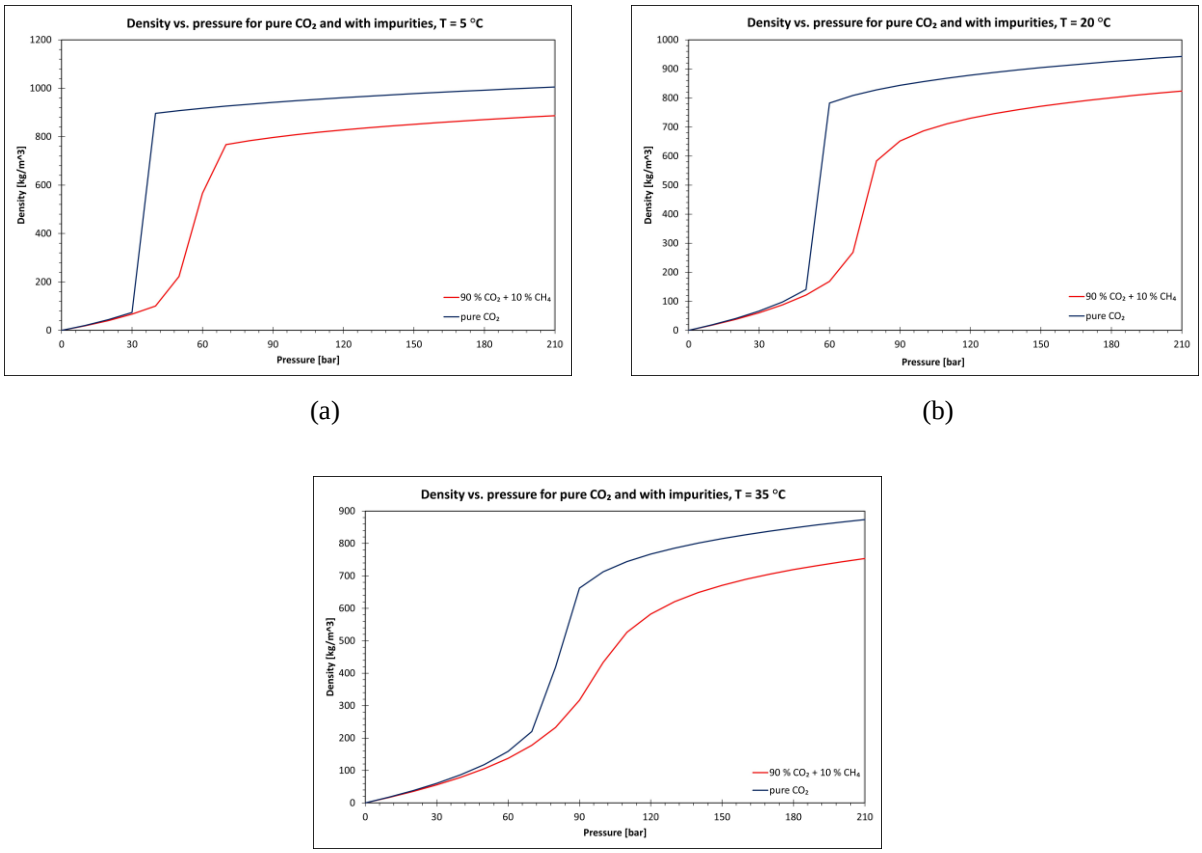

Figure 3.6: Density for pure CO_2 and with impurities as a function of pressure.

As observed, impurity considerably reduces the density in all three scenarios. The reduced density is primarily related to increased volume. As a result, under standard temperature and pressure (STP), impurity components in CO_2 would cause a volume increase higher than their molar or volume fractions [6]. This is understandable since non – condensable impurities are less dense than CO_2 and have a lower molecular weight, requiring larger amounts. The density of a gas at STP can be calculated as shown in Equation 3.1:

$$\rho = \frac{M}{V} \tag{3.1}$$

where ρ is density, M is molar mass and V is molar volume of a gas. Based on Avogadro's Principle for Gases - equal volumes of all gases at the same condition (STP) contain the same number of molecules; the molar volume of CO_2 and methane is 22.4 liter/mole.

Hence the density of CO_2 can be calculated as in Equation 3.2:

$$\rho = \frac{44.01}{22.4} = 1.96\ g/l \tag{3.2}$$

The density of methane is calculated using Equation 3.3:

$$\rho = \frac{16.04}{22.4} = 0.72\ g/l \tag{3.3}$$

Figure 3.7 represents the density of pure CO_2 and methane at the same concentration as discussed earlier but as a function of temperature for isobaric cases of 40 bar (a), 80 bar (b), and 120 bar (c). As can be seen, the density of CO_2 with methane is significantly lower, as previously found in Figure 3.6. However, at a constant pressure of 40 bar, the density lines nearly overlap by displaying slight differences from 10 °C to 40 °C. This is because pure CO_2 and CO_2 with impurities will be in the gas phase at these temperatures and pressure. As a result, there will be little changes in density. However, raising the pressure causes CO_2 to move to a dense phase with significant changes in density between pure CO_2 and with impurities.

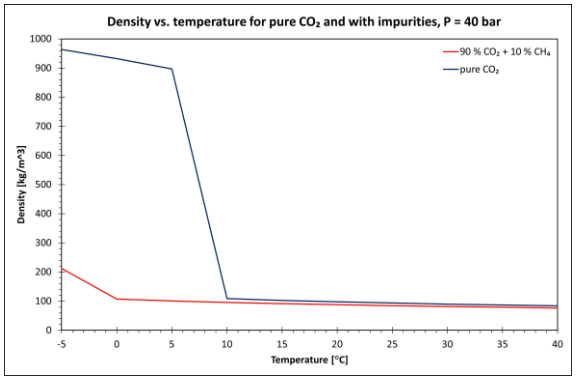

(a)

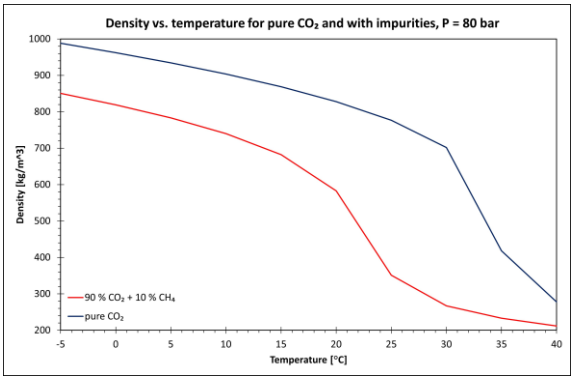

(b)

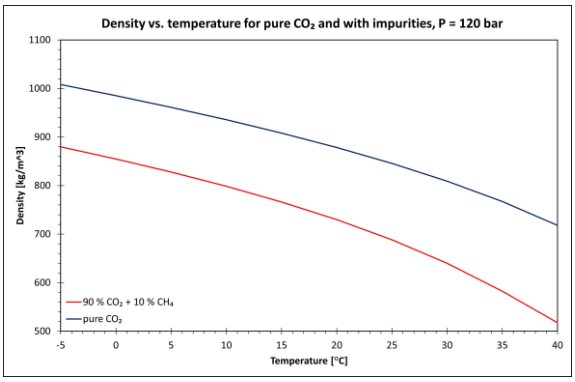

(c)

Figure 3.7: Density for pure CO_2 and with impurities as a function of temperature.

As it has been observed, impurities play a vital role in the whole CCS process, especially during transportation and storage issues regarding density reduction. It should also be noted that keeping the CO_2 stream in a dense phase requires reducing impurities in the stream since these accidental compounds might cause the phase diagram to shift.

3.5 Viscosity

3.5.1 Viscosity of pure CO_2

Viscosity is another essential property in the CO_2 transportation and injection process. Therefore, in Multiflash, the viscosity model must also be chosen in addition to the primary model, GERG – 2008. Viscosity models in Multiflash include SuperTrapp, Mixing Rules, Pedersen, and Lohrenz – Bray – Clark (LBC) [143]. Figure 3.8 compares each model with NIST (National Institute of Standards and Technology) experimental data [144] for the constant temperature 5 °C and pressure range from 0 to 210 bar. As can be shown, the Pedersen model provides the best results when compared to the NIST data. As a result, further simulations will be carried out using this viscosity model.

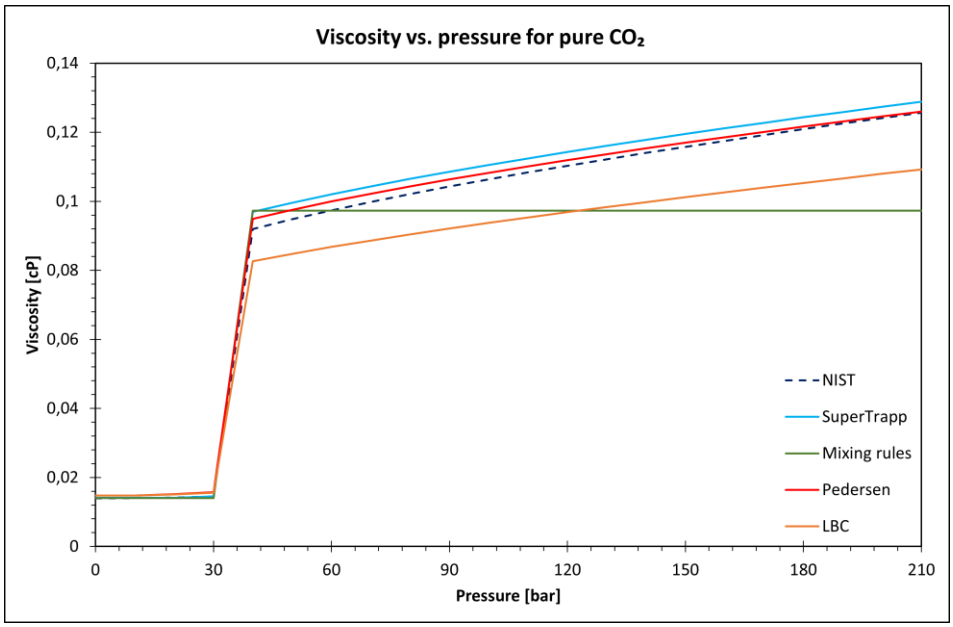

Figure 3.8: Viscosity vs. pressure for pure CO_2 with T = 5 °C.

The viscosity is dependent on both temperature and pressure. Therefore, it will vary with the pipe's inlet pressure and pressure drop. Figure 3.9 represents calculated viscosity as a function of pressure and temperature for pure CO_2. As the graph shows, increasing pressure causes a rise in viscosity. Consequently, the CO_2 stream will be thicker and flow at a lower rate when the pressure increases. However, when the temperature rises, viscosity decreases, allowing the CO_2 stream to become less viscous and flow more quickly. As mentioned earlier in the thesis, the viscosity will be low and vapor – like when CO_2 is in the supercritical phase. Hence, in CO_2 transportation processes, keeping it in a supercritical phase with low viscosity by increasing temperature and keeping pressure above the critical point of 73.9 bar is beneficial.

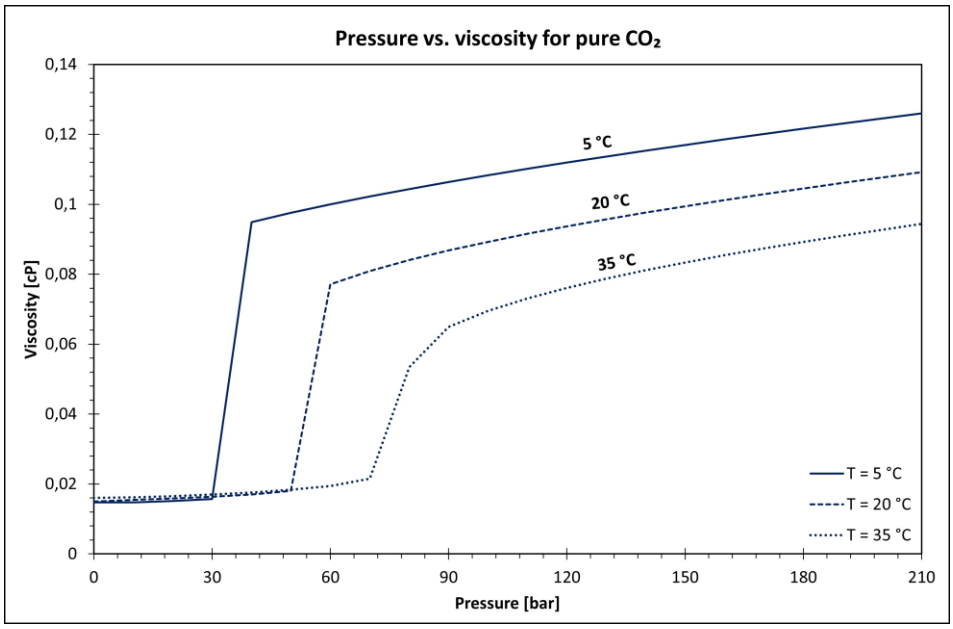

Figure 3.9: Pure CO_2 viscosity as a function of pressure and temperature.

3.5.2 Viscosity of CO_2 with impurities

To investigate how impurities impact CO_2 viscosity, 10 % methane was used in further analyses. Figure 3.10 shows the calculated viscosity of 90 % CO_2 and 10 % methane as a function of pressure and temperature. It is also noticeable that the viscosity of CO_2 with impurity decreases with increasing temperature, as for the case with pure CO_2. The VLE graph demonstrates a significant discontinuity in viscosity, and the impact of temperature on viscosity is stronger in the liquid phase than in the gaseous phase. Adding methane does not significantly impact the fluid's viscosity in the gaseous phase. However, in the liquid and supercritical phases, the viscosity is dramatically affected by adding an impurity, with a drop in viscosity over pure CO_2. Hence, reduced viscosity reduces the pipeline's resistance to fluid flow.

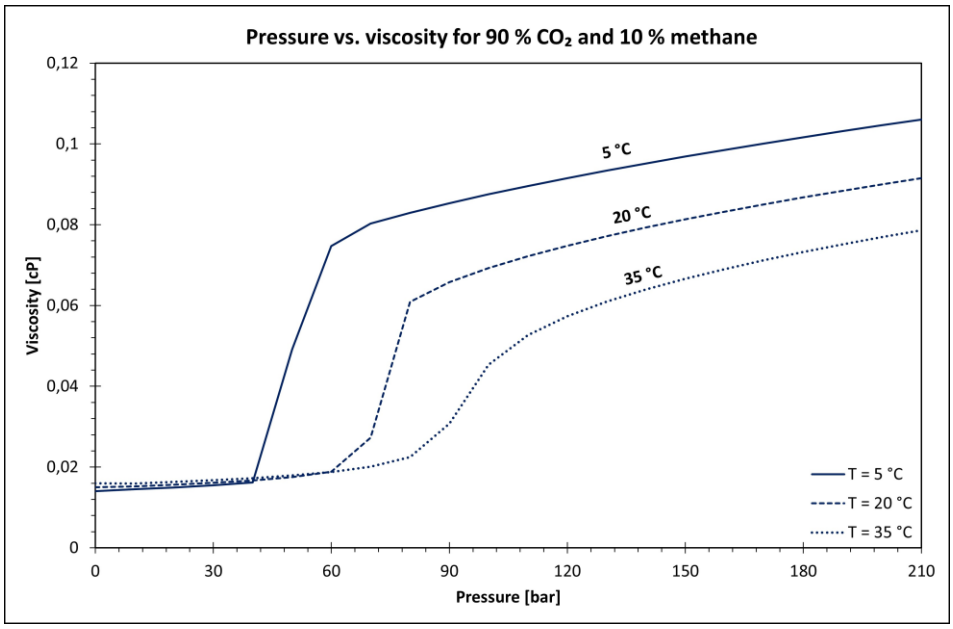

Figure 3.10: Viscosity of CO_2 with methane as a function of pressure and temperature.

It should be noted that the viscosity is highly dependent on the type of impurity and the amount of it present in CO_2. Some impurities can highly reduce the viscosity of CO_2 due to lower molecular weight, resulting in a lower CO_2 mixture density, while others may increase the viscosity over pure CO_2.

In the literature source, some available experimental data for CO_2 viscosity in the presence of impurities was measured at different temperatures and pressures. I. Al – Siyabi [145] published the experimental viscosity measurements conducted using an in-house capillary tube viscometer with a maximum working pressure of 200 MPa and a temperature of 520 K. Experiments were carried out with various binary components and multi – component combinations. In addition, CO_2 with methane was added; however, the methane concentration was just 5 % mole. Hence, for the comparison reason to investigate how the experimental measurement of viscosity differs from the estimated viscosity in Multiflash with Pederson viscosity model, it was chosen to simulate 95 % CO_2 and 5 % methane. Figure 3.11 shows that the simulated Multiflash results overestimate the viscosity compared to the measured data. The mean absolute deviation (MAD) between measured and simulated data is around 6.6 %.

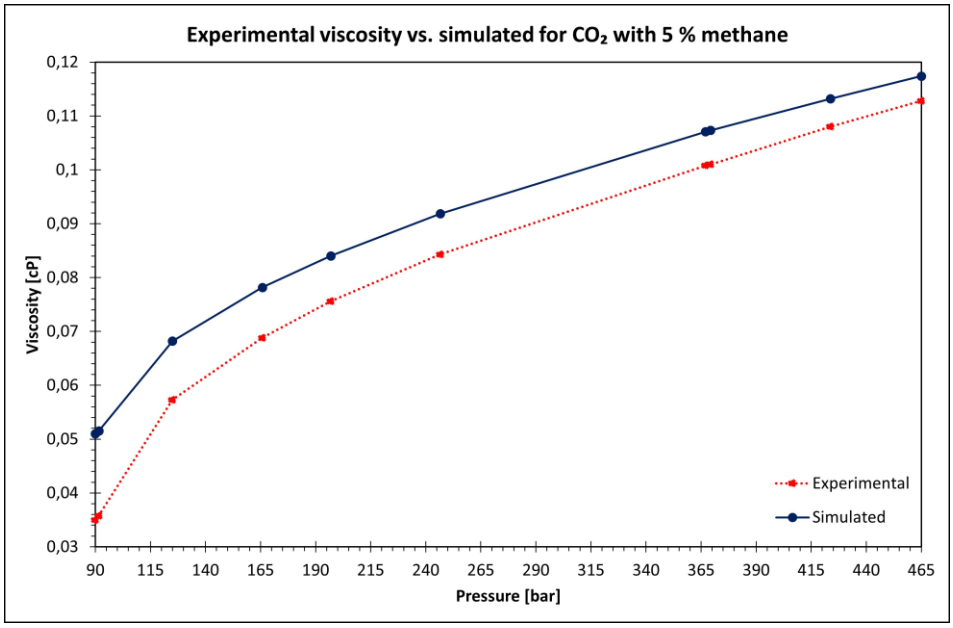

Figure 3.11: Experimental viscosity vs. simulated for 95 % CO_2 and 5 % methane.

3.6 Enthalpy

3.6.1 Mollier diagram for pure CO_2

Enthalpy is another essential property in CO_2 transportation processes because it shows how much heat (energy) is in the system. Heat is crucial because it allows for generating productive work. An enthalpy shift or "change in enthalpy" indicates how much energy was lost or gained during the chemical reaction. Simply, it shows the energy change in the system due to moving from point A to B in the P – T diagram. Pressure and temperature completely represent the fluid conditions for a pure CO_2 component in a single phase. However, when a two – phase flow occurs, the temperature at which the phase change occurs correlates to a certain pressure. As a result, there are many possible equilibrium states during phase transition for a given pressure and temperature. In this case introducing the P – H diagram, also known as the Mollier diagram, may be required to define the system entirely.

The Mollier diagram of pure CO_2 has been generated using the software Thermopack [146] developed by SINTEF Energy Research with constant temperature lines -10 °C, 0 °C, 10 °C, 20 °C, 30 °C, and 40 °C which is shown in the Figure 3.12. When the system has reached thermodynamic equilibrium, the pressure – enthalpy relationship is valid. The solid black curve represents the two – phase flow region where the pressure range is from 0 to 73.7 bar and the temperature scale is from -10 °C to 30 °C. Above the critical point where the pressure is 73.8 bar, and the temperature is 31.1 °C CO_2 will be in the supercritical phase. However, when the temperature is 40 °C, the line exits the black curve zone, indicating that CO_2 will be in the vapor phase while the pressure range is from 0 bar to 73.7 bar; above this pressure, it will enter the supercritical phase.

.

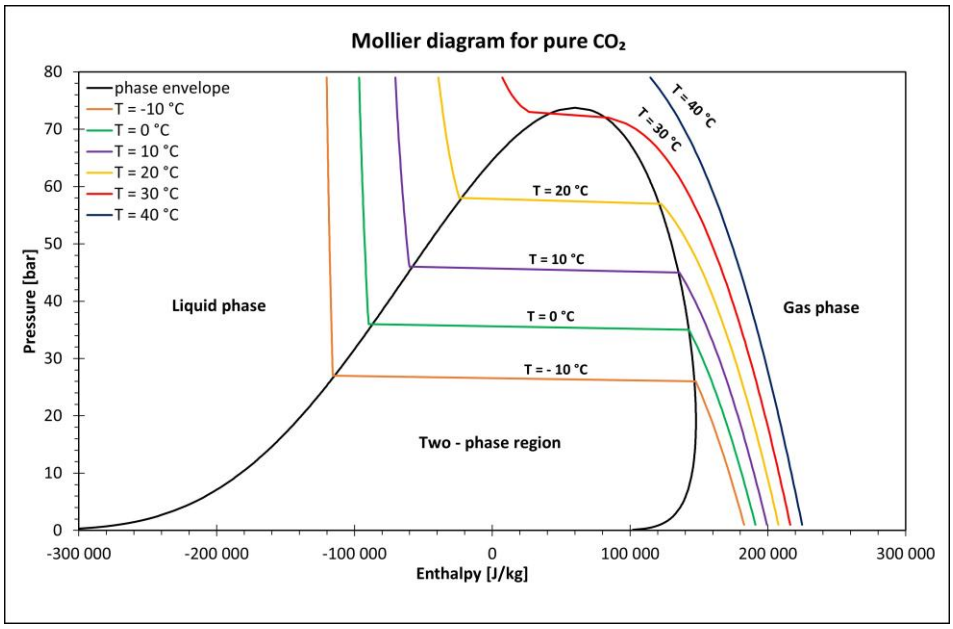

Figure 3.12: Mollier diagram for pure CO_2 with constant temperature lines.

The pressure and temperature of the flowing fluid change throughout the well path. The fluid's thermodynamic equilibrium conditions are thus constantly changing as it flows. Therefore, the calculated Gibbs energy for each phase may be used to determine if the fluid is in equilibrium. Gibbs energy, also known as free enthalpy, is a variable used to calculate the maximum amount of work done in a thermodynamic system with constant temperature and pressure [147]. Gibbs free energy can be expressed as in Equation 3.4:

$$G = H - TS \tag{3.4}$$

where G is Gibbs free energy, H is enthalpy, S is entropy, and T is the absolute temperature. When two fluid phases coexist and are in thermodynamic equilibrium, the Gibbs energy of the liquid equals the Gibbs energy of the gas. In disequilibrium, the more stable phase has a smaller Gibbs energy. But it should be noted that CO_2 phase change and thermodynamic disequilibrium do not always indicate unstable rate, temperature, or pressure conditions during injection operations [148].

3.6.2 Mollier diagram for CO_2 with impurity

It was chosen to simulate Thermopack with 90 % CO_2 and 10 % CH_4 to see how impurities impact the P – H diagram. As a result, the Mollier diagram, as shown in Figure 3.13, has been completely changed as compared to the case for pure CO_2 concentration. This is because the range of the energy amount is shifted in addition to the critical point of CO_2 with impurity. CO_2 will be in a two – phase flow regime at temperatures ranging from -10 °C to 20 °C and pressures ranging from 0 to 78.9 bar. However, when the temperature is between 30 °C and 40 °C and the pressure is between 0 and 78.9 bar, CO_2 is in the vapor phase. Above that pressure, it changes to the supercritical phase.

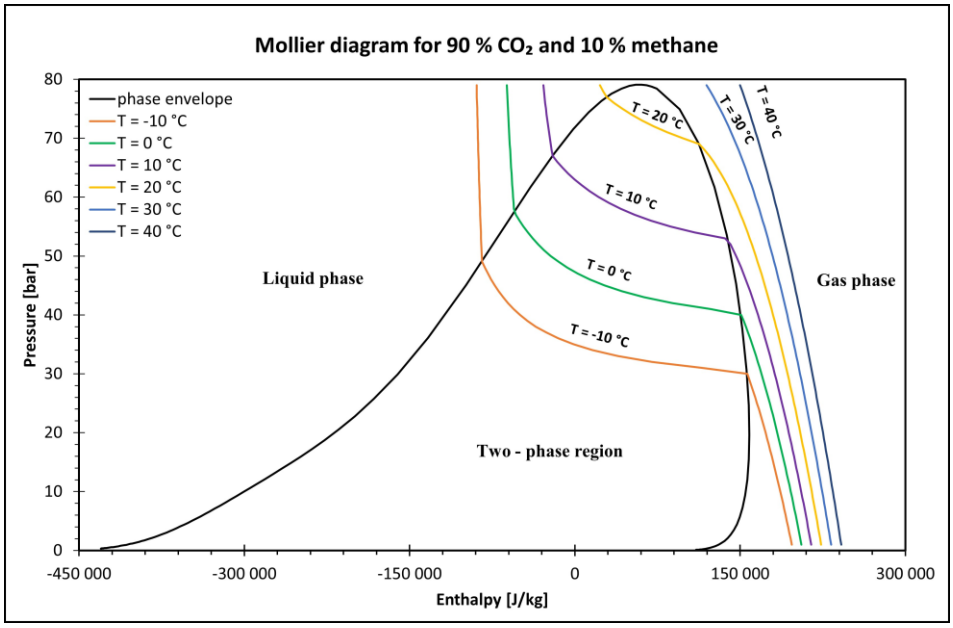

Figure 3.13: Mollier diagram for 90 % CO_2 and 10 % CH_4 with constant temperature lines.

It should be noted that the Mollier diagram will change and be unique depending on the type of impurity and its concentration. As a result, determining the exact amount of each component is critical in CO_2 injection operations.

4 Methodology

This chapter describes the current project's methodology, such as the behavior of pure CO_2 in a 1D pipeline, which aids in understanding the flow pattern during CO_2 injection processes, applied software, and their specification and description of how the model is setup in the simulator. A key element in the CO_2 injection processes is the interface between transportation and storage, namely the injection well, where various transient scenarios involving multiphase flow will occur. The study primarily aims to compare experimental and simulated data from FlowManager™ and OLGA. Therefore, it has been decided to complete the same model configuration in both simulators to verify and compare the results from simulations and experiments. The pressure drop and liquid volume fraction, and densities are the values of interest to compare across experiments and models.

The data in this thesis represents two independent experimental setups. It will be referred to as experimental setups 1 and 2 for simplicity of understanding of the experimental data and results. Both experimental models simulated to steady state.

The first experimental data are available in [7]. Pure CO_2 was tested in a two – phase flow region in a 13.7 m long vertical pipeline for upward and downward flow at a pressure of 6.5 MPa. The pressure was adjusted so that the pressure in the experiments was near the critical pressure of CO_2, 73.8 bar. There were 35 experiments conducted consisting of both upwards and downwards flow. The cases in this thesis were modeled with no slip, as it was found in the paper that the no – slip correlation best matched the experimental data.

SINTEF provided the second set of experimental data, and the experiments were carried out in a horizontal flow loop geometry known as DeFACTO [149]. The studies were carried out using pure CO_2, in different phases. It includes 5 cases: 2 in the gas phase, 2 in the liquid phase, and 1 in the two – phase region.

4.1 Software

Simulations were performed using the following version of the software:

- FlowManager™ 2.2.1
- OLGA 2021.1.0
- Multiflash 6.1

4.1.1 FlowManager™

FlowManager™ is a multiphase flow simulator developed by TechnipFMC. The software combines steady – state and transient models for a complete field layout with powerful optimization methods. It has a robust and fast network solver that ensures the overall convergence of the model components. The simulator covers all operational scenarios such as production, shut – in, and restart for a complete subsea field layout (reservoir, wells, pipelines, subsea process equipment). In addition, the software provides online or offline monitoring and represents all relevant subsea components, which allows monitoring of the entire field layout from the bottom hole to the topside [150].

To complete the simulations in the FlowManager™ following input is required:

- Model configuration including inlet and outlet boundary conditions and flow path geometry.
- PVT library, which can be built by using Multiflash or PVTsim, in the thesis has been generated using Multiflash. The file is in .tab format.

Two mass balances for gas and liquid and one momentum balance are required to solve the model for one – dimensional multiphase pipe flow. Separate mass equations are applied for each phase in Equation 4.1

$$\frac{\partial}{\partial t}\left(m_f\right) + \frac{1}{A}\frac{\partial}{\partial x}\left(A m_f u_f\right) = Q_f \tag{4.1}$$

where m_f is the mass, A is the cross – sectional area of the pipe, u_f is the average velocity, and Q_f is a source term that considers mass transfer and sources of the phase or component f.

Equation 4.2 is the one total momentum equation.

$$\frac{\partial}{\partial t}\sum_f I_f + \frac{1}{A}\frac{\partial}{\partial x}\sum_f A I_f u_f + \frac{\partial p}{\partial x} + \sum_f \alpha_f \rho_f g' + F_{tot} + W = 0 \tag{4.2}$$

where I_f is the momentum, p is the pressure, g' is the gravity and level gradient term, F_{tot} is the total wall friction, W is the source term that considers mass transfer and sources.

The energy equation can be expressed in terms of specific total energy E_f, described in the Equation 4.3, to determine a common temperature T for the phases.

$$\frac{\partial}{\partial t}\sum_f m_f E_f + \frac{1}{A}\frac{\partial}{\partial x}\sum_f A m_f u_f E_f + \frac{1}{A}\frac{\partial}{\partial x}\sum_f A\frac{m_f}{\rho_f} u_f p + U = 0 \tag{4.3}$$

where U is a source term that takes into account heat flux to the surrounding pipe wall, mass transfer and sources.

Summarizing the mass equations for all phases yields a pressure evolution equation [151, 152] described in Equation 4.4

$$\frac{\partial p}{\partial t} = \kappa \sum_f \frac{1}{\rho_f}\frac{\partial I_f}{\partial x} + G \tag{4.4}$$

where G is a source term that takes into consideration mass transfer and sources. The numerical scheme highly depends on coupling this pressure development equation to the momentum equation. Coefficient κ is calculated by using Equation 4.5

$$\kappa = \left[\sum_{f} \frac{\alpha_f}{\rho_f} \frac{\partial \rho_f}{\partial p} \right]^{-1} \tag{4.5}$$

where α_f is the volume fraction, ρ_f is the density.

4.1.2 OLGA

OLGA is the dynamic multiphase flow simulator models time – dependent behaviors, or transient flow, to maximize production potential. Deepwater development relies heavily on dynamic modeling, widely used in offshore and onshore developments, to explore transient behavior in pipelines and wellbores. The OLGA simulator provides an additional perspective to steady – state analyses by predicting system dynamics such as time – varying flow rate changes, fluid composition, temperature, solids deposition, and operational changes [153].

The OLGA simulator accurately predicts essential operating conditions involving transient flow, from wellbore dynamics for any well completion through pipeline systems with all process equipment. The software began as a project for Statoil to simulate slow transients associated with mass transfer rather than the quick pressure transients familiar from the nuclear sector. Terrain slugging, pipeline starting and shutdown, varying production rates, and pigging were all issues of interest. In extreme circumstances, this meant simulations with time periods extending from hours to weeks. As a result, the numerical approach must be stable throughout long timesteps and not be constrained. The first version of OLGA based on this method was operational in 1983 [152]. However, the primary development was in a cooperative research program financed by Conoco Norway, Esso Norge, Mobil Exploration Norway, Norsk Hydro A/S, Petro Canada, Saga Petroleum, Statoil, and Texaco Exploration Norway. The model is still under continuous development and improvement, with Schlumberger being the current license holder.

4.1.3 Multiflash

Multiflash is a powerful and flexible system for modeling physical properties and phase equilibria. It can be used as a stand-alone program or with other software. Multiflash can supply:

- All thermodynamic and transport properties are required for engineering studies.
- Integrated fluid characterization and model setup for petroleum fluids.
- Flash calculations to identify phases present at given conditions, their type, composition, and quantity.
- Complete phase envelopes showing phase boundaries and critical points.
- Simulation of solid formation includes pure solids, halide scales, hydrates, waxes, and asphaltenes.

Multiflash provides a comprehensive set of equations of state (EoS) for PVT calculations. There are around 17 EoS available in Multiflash. The most used and well-known are Peng – Robinson (PR), Redlich – Kwong (RK), GERG-2008, Soave – Redlich – Kwong (SRK) and Perturbed Chain Statistical Associating Fluid Theory (PC-SAFT) [154].

4.2 Experimental setup 1

Experimental data have been gathered for two – phase pure CO_2 saturated at 6.5 MPa in FALCON, represented in Figure 4.1, IFE's (Institute for Energy Technology) flow assurance loop for CO_2 transport. The saturation temperature is 24.4 °C. The pipe has an inner diameter of 44 mm, a length of 13.7 m, an estimated effective surface roughness of 17 micrometers, and a relative pipe roughness is 3.9×10^{-4} [7].

The position of the broad – beam gamma densitometer and the inlet and outlet sections are the primary differences between the up – flow and down – flow designs. The broad – beam gamma densitometer is located at the inlet (top) of the pipeline for downward flow and at the outlet for upward flow. A pre – separator is included in the vertical down setup, but there is no outlet pre – separator in the vertical up setup (see Figure 4.1 for an outline).

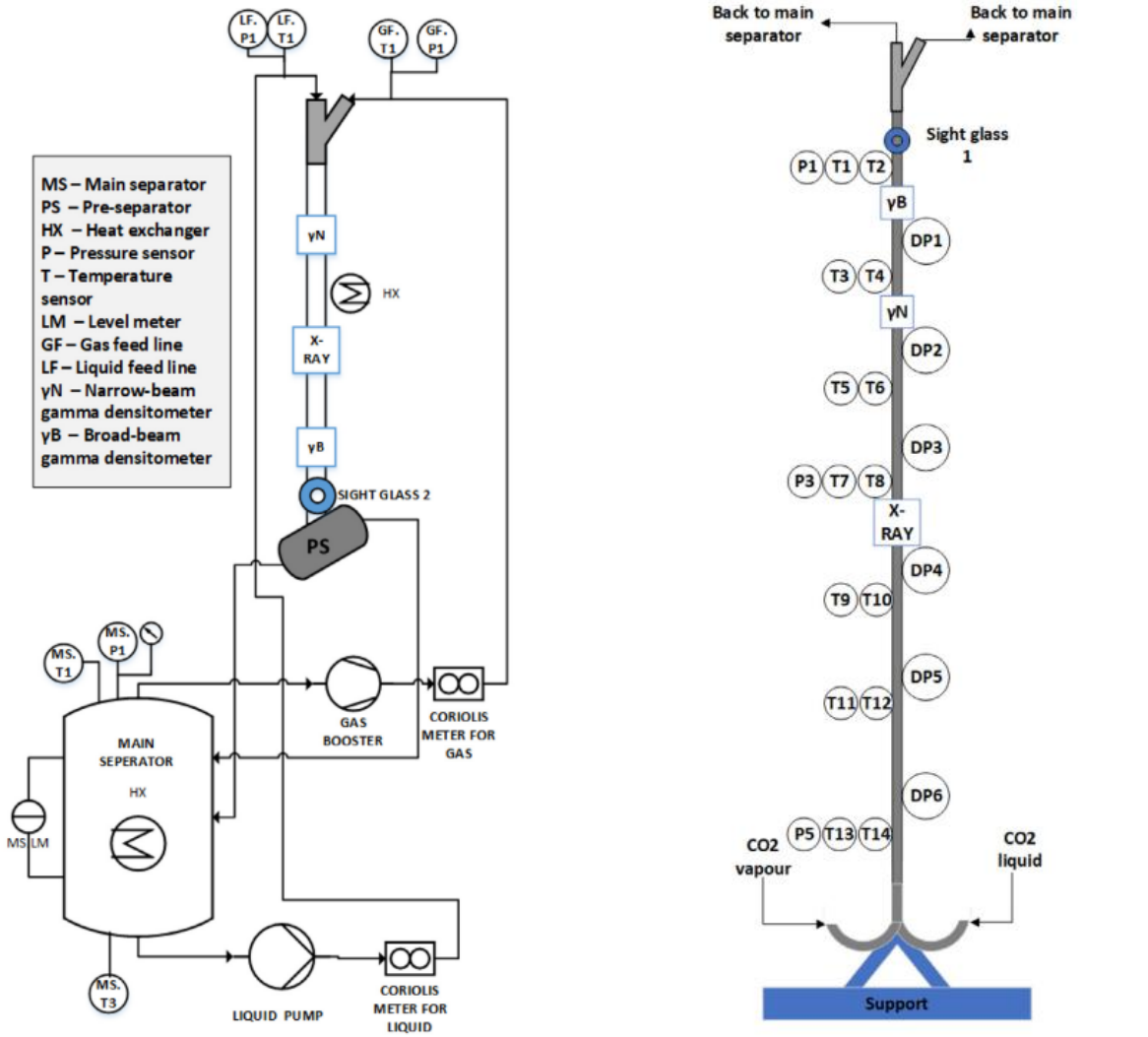

a) Process design for vertical downward flow

b) Process design for vertical upward flow

Figure 4.1: Schematic of the FALCON test facility [7].

The gas and liquid phases are extracted from the top and bottom of the main separator, respectively, and transported as single – phase fluids to the test section's inlet merger through separate feed lines. A combined heating/cooling system controls the temperature. A coolant circulates via copper – tubing heat exchangers that are coiled onto the main separator and the test section. The coolant temperature is adjusted, so that heat transmission to the system via heat exchangers balances the heat contributed by the pumps and heat loss to the ambient, validating the assumption of an adiabatic system. The temperature and pressure are therefore managed stably and precisely. The ambient temperature is approximately 10 °C, and the impact of the electrical heater and the cooling plant allows for steady working temperatures of -10 °C to 40 °C.

Both the vertical upward and vertical downward pipelines are built of stainless steel and are supplied with 14 mean temperature sensors and 3 mean pressure sensors. The pipe is inclined at 90 degrees. The experiment included 35 cases, and all measurements were obtained on the same day. The values of superficial liquid velocity and superficial gas velocity were calculated using Equations 4.6 and 4.7, respectively.

$$u_{SL} = \frac{m_{SL}}{A \cdot \rho_l} \tag{4.6}$$

where m_{SL} is the mass flow rate of liquid, A is the area of the pipe, ρ_l is the density of liquid.

$$u_{SG} = \frac{m_{SG}}{A \cdot \rho_g} \tag{4.7}$$

where m_{SG} is the mass flow rate of gas and ρ_g is the density of gas.

The liquid fraction can be calculated using the values of superficial liquid and gas velocity through Equation 4.8

$$x = \frac{u_{SL}}{(u_{SL} + u_{SG})} \tag{4.8}$$

Moreover, measurements for gas mass flow rate, liquid mass flow rate, and liquid and gas densities have been completed. Pressure and temperature measurements for the main separator at the top and bottom and the pressure and temperature for the gas feeding line before the merger and for the liquid feeding line before the merger have been performed. The flow is assumed adiabatic ($Q = 0$).

4.3 Experimental setup 1 in FlowManager™

The main input file for the simulation in FlowManager™ includes an inlet boundary, a flowpath and outlet boundary. The inlet boundary conditions are specified for all 35 cases: pressure, temperature, gas, and liquid mass flow rates. A schematic picture of the process for

vertical upward flow is shown in the Figure 4.2. It is a straightforward model with one inflow, a flowline, and one outlet.

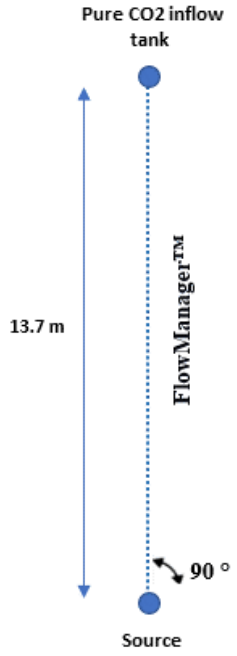

Figure 4.2: Schematic overview of the process for vertical upward flow in FlowManager™.

The pipe as an input for the model is divided into 10 control volumes. PVT table has been generated in Multiflash as an input. It includes standard pressure and temperature (1.01325 bar, 15.55 °C) and goes up to 67 bar, which is relatively close to the critical pressure point (73.8 bar) and 27 °C, at the transition between gas and liquid. As the fluid property tables are limited to a maximum of 200 grid points, it is essential to determine the pressure and temperature span to get a good resolution of the tabulated values while using linear interpolation during the simulations.

CO_2's density is highly sensitive to even the slightest variations in temperature and pressure; choosing accurate EoS for calculating the thermodynamical properties of CO_2 is very important. Therefore, several EoS have been tested to obtain a more accurate pressure drop value with the experimental data. Calculations were performed for all 35 cases for upward vertical flow to see how each EoS deviates from the measured data. The results of the calculations are performed in Chapter 6.

4.4 Experimental setup 1 in OLGA

The numerical method used in OLGA is created for fluids that contain multiple hydrocarbon components. When the operational range is within the two-phase area, such fluids usually have broad phase envelopes that enable the gradual transition. However, single-component fluids are generally sensitive to rapid changes in thermophysical properties when operating near the

critical area or crossing the saturation line. It also occurs for multi-component fluids with narrow-phase envelopes. This is because one component predominates in such fluids, and the behavior is similar to that of a single component. As a result, when simulating such fluids, the numerical strategy used in standard OLGA may become unstable because standard OLGA uses PT-flash formulation, which breaks down for single component fluids crossing the saturation line. Furthermore, even a slight change in pressure can result in entirely different conditions depending on whether the temperature is assumed to be constant. According to that, for H_2O and CO_2, the fluid property calculations have been hard coded into OLGA.

OLGA creates a PVT table for the single component fluid properties by default. The properties are evaluated on a grid of pressure and temperature values constrained by the lowest and maximum pressure and temperature values specified in the input. The gridding is adjusted so that a grid point is near the critical point. During the simulation, linear interpolation between grids is used. The CO_2 single component applies a PH formulation with pressure and mixture enthalpy as independent variables. During calculations, the enthalpy is considered stable for minor changes in pressure but with greater precision than the corresponding temperature assumption. Figure 4.3 represents the model setup in OLGA for vertical upward (a) and vertical downward (b) flow. It has one inlet, flowline, and output, as shown in the picture below.

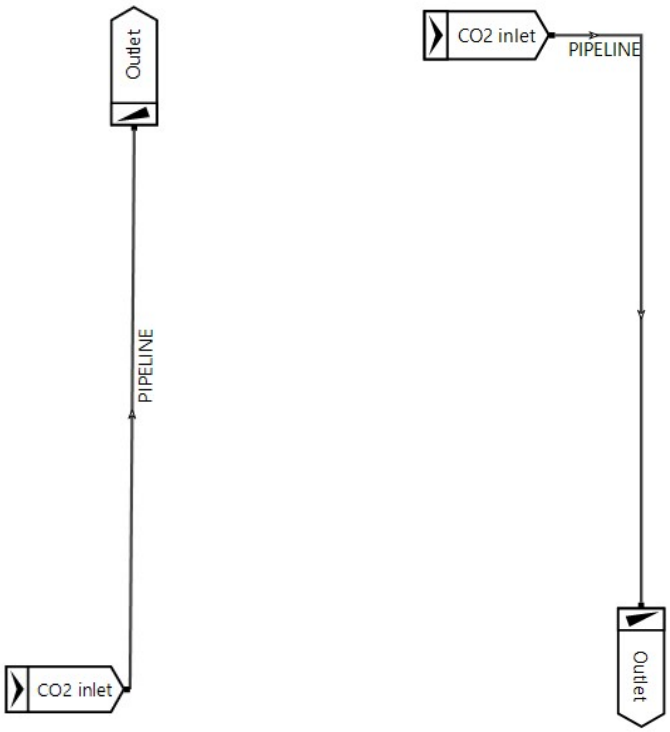

a) Model for vertical upward flow b) Model for vertical downward flow

Figure 4.3: Schematic overview of the process for vertical upward and vertical downward flow in OLGA.

4.5 Experimental setup 2

SINTEF performed the experiment in a setup called DeFACTO. DeFACTO is a vertical flow facility that allows CO_2 to be circulated through a 90 – meter – deep U – tube loop. The loop is outfitted with over 100 high precision – fast response pressure and temperature sensors, allowing for precise pressure measurement. The vertical flow loop is connected to a ~138 – meter – long horizontal flow loop located on the facility's roof (depicted in the Figure 4.4.).

The horizontal flow loop allows CO_2 to be circulated with precisely controlled parameters. DeFACTO can operate at pressures ranging from 0 to 160 bar and temperatures ranging from -60 °C to +60 °C, which covers the typical range for CO_2 injection in depleted reservoirs or aquifers.

The pipeline has a roughness of 1.57 micrometers and is horizontal with an inner diameter of 0.01 m and an outer diameter of 0.012 m. The total length of the pipeline is 138 m and the change in elevation is -0.24 m. The material of the pipeline is AISI316, which is stainless steel. The data were collected when CO_2 was in the gas, liquid, and two – phase flow states. The thesis covers five cases: two for gas, two for liquid, and one for two-phase flow.

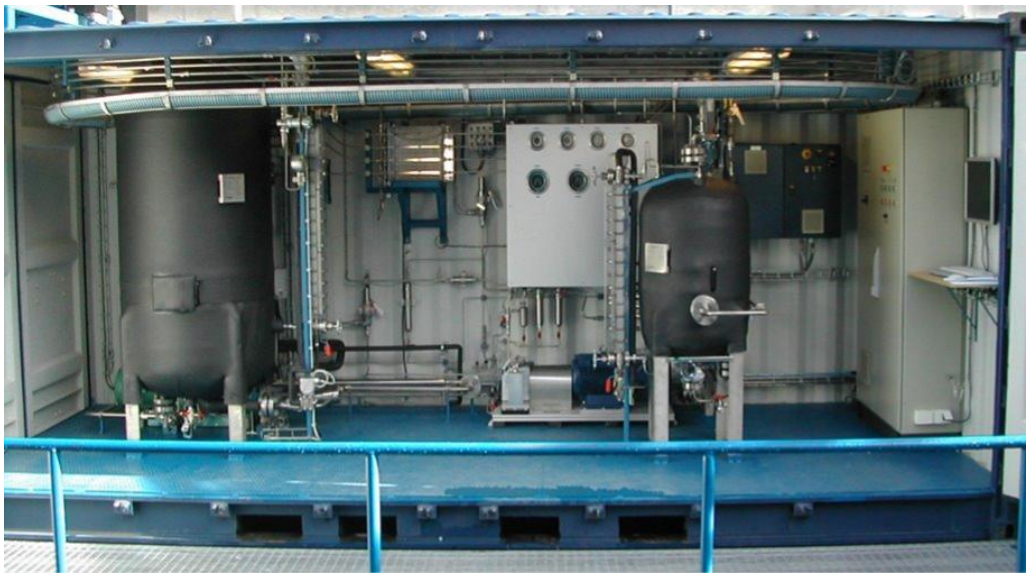

Figure 4.4: Experimental setup DeFACTO [149].

The pipeline has four temperature and pressure sensors, namely TI30, TI40, TI50, TI60, and PI30, PI40, PI50, and PI60, respectively. The pressure drop analyses were performed from the pressure sensor PI30 to PI50. The temperature and mass flow rate of CO_2 in a single gas, single liquid, and two – phase flow phases applied as input parameters are shown in Table 4.1.

After receiving experimental data from SINTEF, the inlet pressure from sensor PI30 required to be corrected. The cause for this and the new corrected inlet pressure values will be covered in Chapter 6.

Table 4.1: Inlet temperature and mass flow of 5 cases.

Cases	Temperature [°C]	Mass flow rate of gas [kg/s]	Mass flow rate of liquid [kg/s]
Gas phase_1	6.50	0.015	[-]
Gas phase_2	10.06	0.018	[-]
Liquid phase_3	-0.40	[-]	0.089
Liquid phase_4	-1.34	[-]	0.060
Two – phase_5	9.12	0.018	0.051

4.6 Experimental setup 2 in FlowManager™

Pressure, temperature, gas, and liquid mass flow rates are the inlet boundary conditions for the 5 cases defined in FlowManager™. The model has a single inflow, a single flowline, and a single output. Because of differences in length, elevation, and the number of control volumes, the pipe geometry used as an input for the model is divided into 12 sections (Figure 4.6). A PVT table with 200 grid points was generated as an input in Multiflash. The temperature ranges from -3 °C to 15.55 °C, while the pressure ranges from 1.01325 bar to 45 bar. The heat transfer coefficient from the pipe to the surroundings was estimated at 13.1 W/m^2·°C [155]. Separate simulations were run for 5 scenarios with different input parameters but the same pipeline geometry.

4.7 Experimental setup 2 in OLGA

Compared to the FlowManager™, OLGA requires information on the material and wall of the pipeline as input parameters since the flow is not adiabatic as in the experimental setup 1. AISI 316 is a stainless steel that can be employed in harsh environments, is corrosion resistant, and can be operated at higher temperatures. Physical properties of AISI 316: material density 8000 kg/m^3, thermal conductivity 18.9 W/m·K, specific heat capacity 500 J/kg·K [156]. The thickness of the wall is 0.001 m and has been calculated using Equation 4.9

$$\tau = \frac{OD - ID}{2} \tag{4.9}$$

where τ is the thickness, OD is the outer diameter, and ID is the inner diameter of the pipe.

Simulations in OLGA were performed for a single CO_2 component with PH formulation for 5 cases. Each case was run independently, using the same pipeline geometry but with different input parameters. Input pressure, temperature, gas and liquid mass flow rates, and measured inlet and outlet ambient temperatures were given OLGA. Furthermore, because the process is not adiabatic, the heat transfer coefficient and material of the pipeline wall must be provided. The schematic overview of the process is presented in the Figure 4.5.

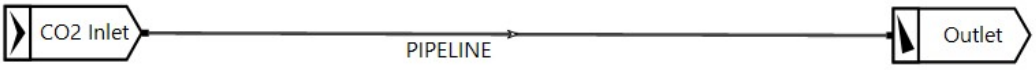

Figure 4.5: Schematic overview of the process.

The flow path geometry is illustrated schematically in Figure 4.6. Because of the varying elevations and lengths, the horizontal flowline is divided into 12 sections (pipe -1 to pipe -12), as seen in the picture below.

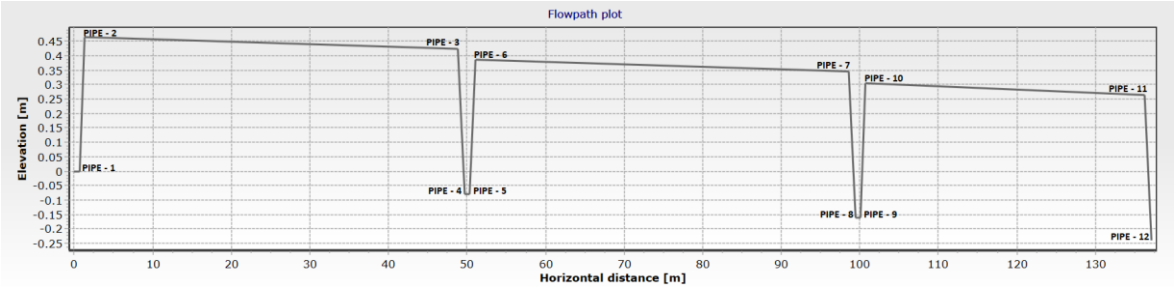

Figure 4.6: Flow path geometry generated in OLGA.

5 Experimental setup 2 results analysis

After receiving raw data from SINTEF for experimental setup 2 and pressure data from four pressure sensors, it was necessary to apply pressure corrections to the data acquired by the sensors. This is because various factors can impact pressure sensors, resulting in inaccurate values.

Temperature and humidity changes, for example, could cause pressure sensors to generate inaccurate readings. Furthermore, external influences such as vibrations or electromagnetic interference might impact pressure sensors. As a result, pressure readings must be corrected to ensure the data collected is as accurate as possible.

Pressure correction can be performed through various methods, including calibration curves or mathematical models. A mathematical model was used in the thesis work. Data from four sensors with zero flow for the gas and liquid cases were specified to do this. The average value for the gas case with zero flow was around 18 bar, and the value for the liquid case was about 38 bar. Next, a linear trendline between the data points determines the k and m coefficients required to adjust the pressure sensors. The k and m values used to adjust the sensors are shown in Table 5.1.

Table 5.1: k and m values to adjust the pressure sensors.

Sensors	k	m
PI30	1.0101	-0.0779
PI40	0.9999	-0.0085
PI50	0.9923	0.0234
PI60	0.9979	0.0619

Pressure correction was performed by using Equation 5.1 (shown here only for pressure sensor PI30).

$$PI30^{*} = PI30 \cdot k + m \tag{5.1}$$

where $PI30^{*}$ is corrected pressure, $PI30$ is the raw data.

Figure 5.1 demonstrates the corrected values and position of the four pressure sensors for 5 cases. As can be seen from the graphs, sensors are located at 0 m, 50 m, 100 m, and 138 m, accordingly.

It is expected that the average corrected pressure sensor reading vs. sensor position should result in a constant slope. The constant slope indicates constant pressure gradient in the experimental flow loop. Especially for case (a) and (b), a change in pressure gradient was

observed for sensor PI60. Due to this unexpected behavior, SINTEF advised to exclude sensor PI60 from comparisons with simulated results.

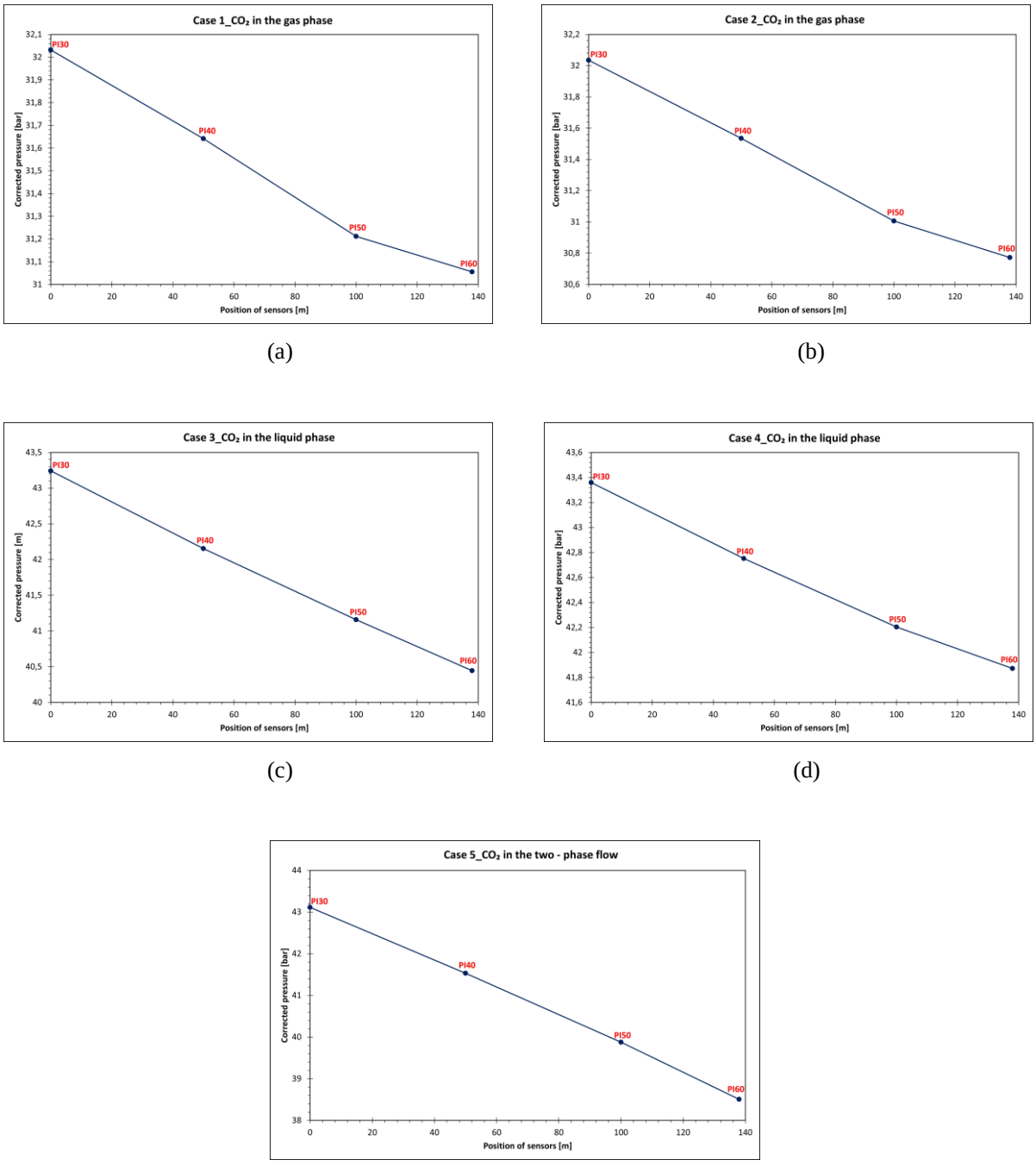

Figure 5.1: Corrected pressure values vs. positions of sensors for case 1 (a), case 2 (b), case 3 (c), case 4 (d), case 5 (e).

Table 5.2 represents measured pressure values from the PI30 sensor and after correction PI30* when a mathematical model is applied. The corrected values from PI30* have been used as the input parameters in simulators.

Table 5.2: Measured pressure values from PI30 and after correction PI30*.

Cases	**PI30**	**PI30***
Case_1	31.79	32.03
Case_2	31.79	32.03
Case_3	42.89	43.24
Case_4	43.00	43.36
Case_5	42.76	43.11

6 Results and discussion

This chapter contains the results and discussion of experimental setups and the experimental data for pure CO_2 compared with the calculated data from FlowManager^{TM} and OLGA software. Different EoS have been evaluated to calculate the PVT properties of pure CO_2 and CO_2 with impurities. From sections 6.2 to 6.6 it summarize the results for experimental setup 1, where CO_2 exists in a two – phase flow. Finally, section 6.8 combines the experimental setup 2 results from both software when CO_2 is in a single gas phase, single liquid phase, and two – phase flow phase.

6.1 Evaluation of different EoS for experimental setup 1

Calsep, a specialist company within an oil and gas properties and phase equilibria [157], completed a validation project evaluating the performance of four industry – standard equations of state for modeling of pure CO_2 and CO_2 with impurities, such as SRK – Peneloux, PR – Peneloux, GERG – 2008, and PC – SAFT [158]. As a result, the GERG – 2008 equation was demonstrated to be an excellent choice as a fluid model in CCS engineering calculations, providing accurate predictions of all examined parameters. Due to this first EoS used to calculate PVT properties of pure CO_2 was GERG – 2008. Then it was decided to do a parameter study on EoS to see which EoS gave the best simulated pressure drop results compared to the experiments from experimental setup 1.

The relative error (Equation 6.1) between calculated and measured pressure gradients for all 35 cases was used to determine which EoS simulation compared best with the experiments.

$$Relative\ Error = \frac{(calculated - measured)}{measured} \tag{6.1}$$

Table 6.1 displays the findings from various EoS values. As observed, the closest value to the experimental data comes from the RKS – HV (Huron – Vidal) model. However, RKS (Redlich – Kwong – Soave) and PSRK (Peng – Robinson – Stryjek – Vera) provide the same deviation values from the experimental data.

Both RKS and PSRK equations of state are considered relatively accurate for calculating the thermodynamic properties of pure CO_2. However, there are some differences in their performance. PSRK is often considered more accurate than RKS, particularly at high pressures and low temperatures. This is because PSRK considers the effects of molecular interactions between CO_2 molecules and becomes more critical at high pressures and low temperatures. RKS, on the other hand, assumes that the molecules in the fluid are non – interacting, which can lead to some inaccuracies at high pressures and low temperatures [154, 159-161].

The RKS with the HV mixing rule is a well – known and commonly used thermodynamic model for predicting the thermodynamic parameters of pure fluids and their mixes. For CO_2 specifically, the RKS – HV equation of state has been shown to provide reasonably accurate predictions for a range of thermodynamic properties over various temperatures and pressures. The RKS – HV equation of state's accuracy is determined by the quality and amount of

experimental data used to estimate model parameters [154, 162-164]. However, for this experimental data, it gives the best results among other EoS.

Table 6.1: Pressure gradient analyses of different EoS for experimental setup 1.

	GERG -2008	**RKS**	**RKS-HV**	**PSRK**	**CO_2 high accuracy model**	**PR**	**PR78**
Total average relative error for all cases	23 %	- 12 %	- 11 %	- 12 %	25 %	- 2 %	-2 %
Total standard deviation	37 %	10 %	10 %	10 %	36 %	25 %	24 %

As previously mentioned, the first EoS used for PVT calculations of pure CO_2 was GERG – 2008. Figure 6.1 shows the results in comparison to the measured data. As can be observed, the findings have been overestimated by more than 30 % in most cases, with a total average inaccuracy of 23 % for all 35 cases. The PVT table generated as input for FlowManager^{TM} therefore uses the RKS – HV EoS.

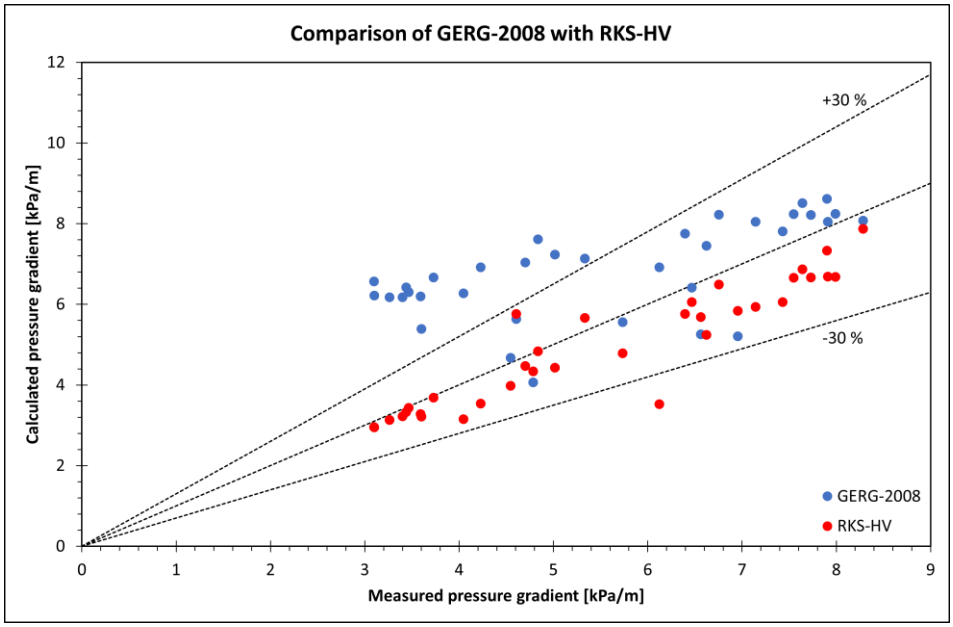

Figure 6.1: Comparison of EoS GERG-2008 with EoS RKS-HV.

6.2 Results from FlowManager™

6.2.1 Vertical upward flow

The measured vs. calculated pressure gradients for the 35 experimental cases are shown in Figure 6.2. As can be observed, the calculated pressure gradient is underestimated compared to the experimental data, with the total average relative error equal to -11 %. The total standard deviation is 10 %. Some cases have values incredibly near the experimental data. The deviation for most cases is less than 30 %. Case 16 (pointed with an arrow) is located outside the -30 % range having the lowest calculated pressure drop compared with the experimental one with the relative error value of -43 %. The density parameter, described below, can explain the reason for such deviation.

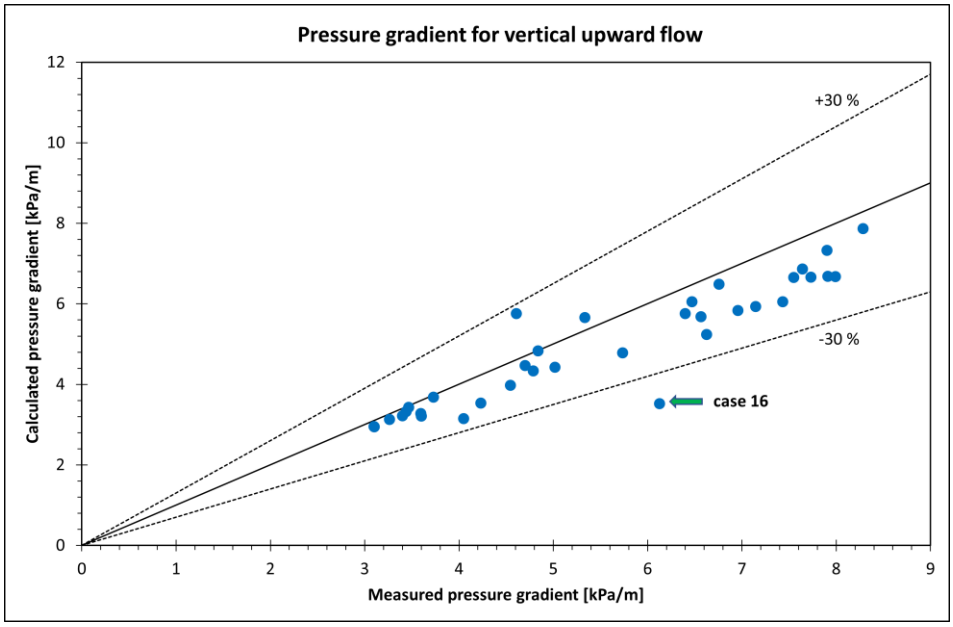

Figure 6.2: Measured pressure gradient vs. calculated for vertical upward flow in FlowManager™.

Figure 6.3 compares the measured density of gas (a) and liquid (b) with the calculated density at the pipeline's outlet. The calculated density of the gas is underestimated for all 35 cases compared with the experimental data with the total average relative error value of -1 %. The same pattern follows for the density of liquid values but with a total average relative error value of -20 %.

In the paper [7] mentioned that the liquid – to – gas ratio ρ_l/ρ_g equals 2.83, whereas, from the FlowManager™ software calculations, the ratio equals 2.25.

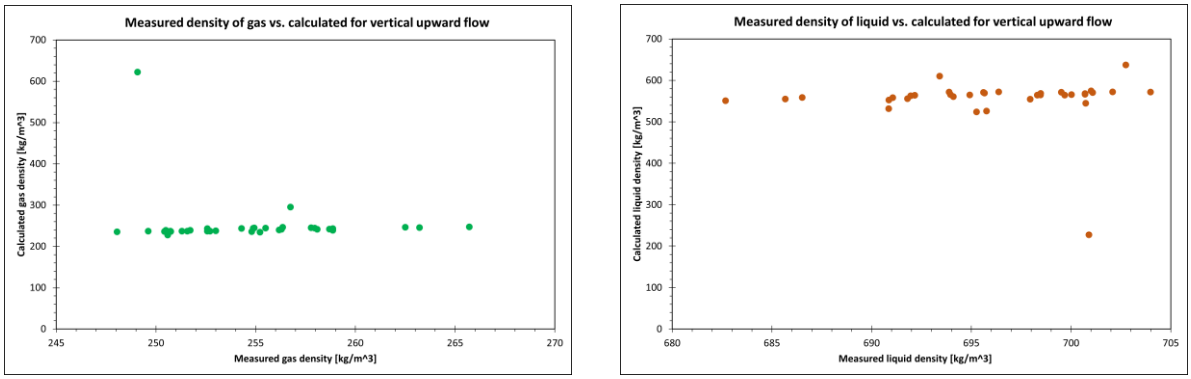

(a) (b)

Figure 6.3: Measured density of gas (a) and liquid (b) vs. calculated for vertical upward flow in FlowManager^{TM}.

Figure 6.4 depicts the calculated gas and liquid density at the pipeline's inlet and outlet vs. the number of cases. As observed, the gas density (a) is higher at the inlet and lower at the pipeline outlet except for cases 1 and 8. In case 1, there is a sudden "jump" at the pipeline outlet. According to the PVT table, large jumps in CO_2 gas density occur when crossing from the single phase gas region to the single phase liquid region even with small changes in pressure or temperature. For some of the cases simulated, the gas density jumped from typical gas values around 250 kg/m^3 at the inlet to typical liquid density which values around 560 kg/m^3 at the outlet. This quick transformation is only possible if a cooling or compression procedure is used. However, in the experiments, such activities have yet to be performed; and it was only measured for the two – phase flow region. Consequently, such changes in the phases are limited. Similar behavior also occurs on the graph with liquid density (b). Changes from liquid at the pipeline's inlet to gas at the pipeline's outlet could be feasible in practice; however, this was not the scenario explored in the experiments. For example, in case 16, seeing the phase transition during simulations is feasible. CO_2 has a density equal to liquid at the inlet of the pipeline and exits it with a density similar to gas. According to the experimental data, the temperature at the outlet is lower than at the inlet, and the CO_2 will experience a decrease in volume due to its lower temperature, causing an increase in density. Moreover, CO_2 is a substance that contracts upon cooling. Regarding this phenomenon, the density of liquid CO_2 should be higher at the outlet than at the inlet of the pipeline.

Large jumps observed in gas or liquid density strongly effect the calculated pressure drop. This is the reason for large differences in some of the measured vs. calculated pressure drops.

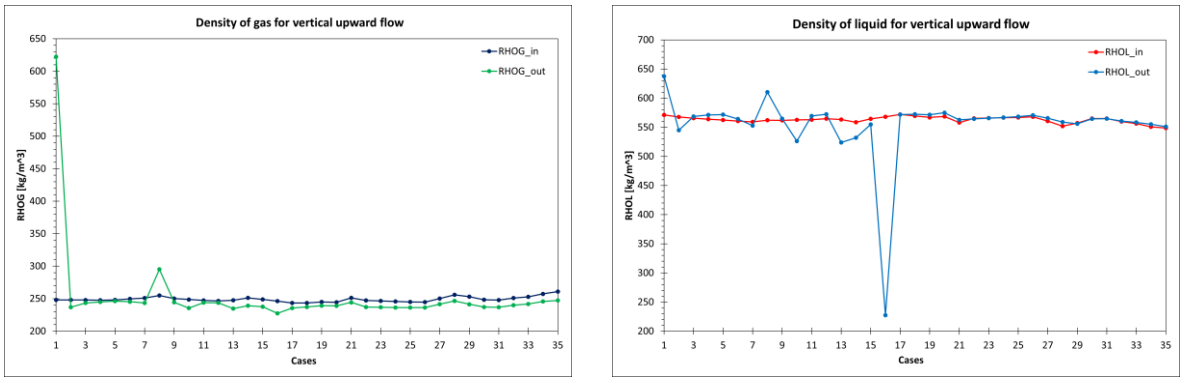

(a) (b)

Figure 6.4: Calculated density of gas (a) and liquid (b) vs. number of cases at the inlet and outlet of the vertical upward flow pipeline in FlowManager^{TM}.

Figure 6.5 presents the phase diagram of pure CO_2 and the area where the experiment was carried out with corresponding pressure and temperature to understand the phase transition phenomenon better. The left side represents a single liquid phase, the right side represents a single gas phase, and the line inside the box means when CO_2 is in a two – phase flow regime. That is where the experimental measurements were taken. This area is extremely sensitive to variations in temperature and pressure. In addition, when CO_2 is pure, it does not have a phase envelope, as for the case with impurities discussed in Chapter 3. Hence, because of the relatively narrow phase transition area (along the line), the numerical approach used in the simulations may become unstable and have difficulty accurately capturing the area. As a result, phase transitions occur from two – phase flow to a single gas or liquid phase and vice versa. This occurrence can also explain the deviation in the pressure gradient between measured and calculated data since the density is pressure and temperature dependent. Hence, the PVT created in Multiflash is not entirely reasonable for comparison with the experimental data when CO_2 is pure and in a two – phase flow.

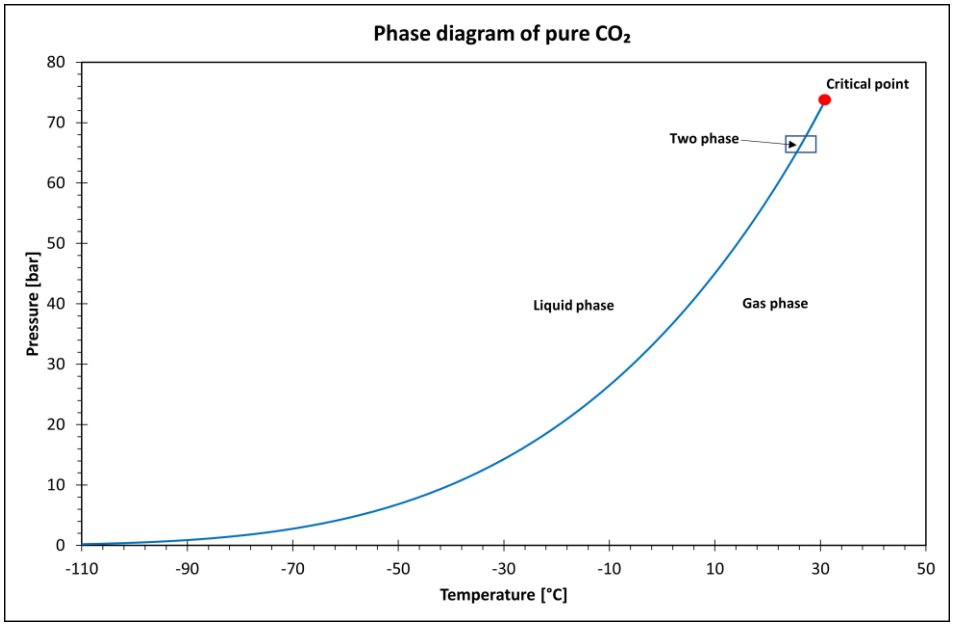

Figure 6.5: Phase diagram of pure CO_2.

The measured and simulated liquid volume fraction (VFL) was also compared. Figure 6.6 demonstrates the measured VFL vs. the calculated VFL. As demonstrated, the calculated values are slightly overestimated compared with the experimental data, with a total (all cases) average relative error value of 7 % (calculated by using Equation 6.1). The total standard deviation error of all cases is 6 %. The formula how the software calculates VFL is shown in section 4.2.

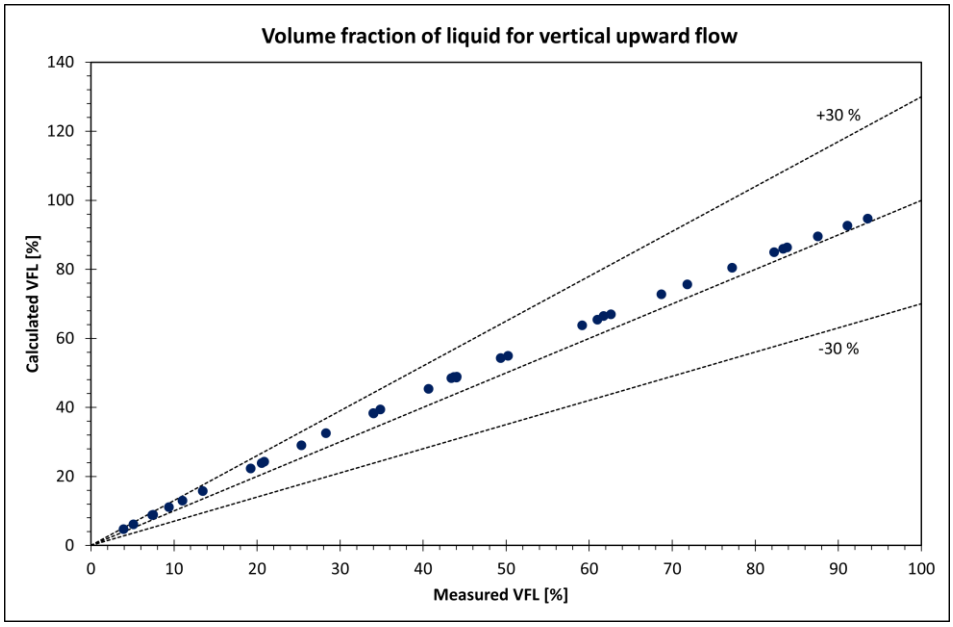

Figure 6.6: Measured volume fraction of liquid vs. calculated for vertical upward flow in FlowManager™.

6.2.2 Vertical downward flow

Figure 6.7 demonstrates the measured negative pressure gradient vs. calculated for 35 cases of vertical downward flow. It should be noted that when the flow direction is changed from upward to downward, the pressure at the pipeline outlet (bottom) can be higher than the inlet (top). This is due to gravity's effect on the fluid. Because of its position above the outlet, the fluid gains potential energy as it flows down the vertical pipeline. This potential energy is converted into pressure energy at the outlet, resulting in a higher pressure at the outlet than at the inlet.

As for the upward flow, the pressure gradient is underestimated in most cases. There are two cases outside the +30 % and several cases outside of -30 %. For example, cases 5 and 30 show the highest overestimated calculated values compared with the experimental data and are outside the +30 % range. This is because CO_2 is transitioning from a single gas to a single liquid phase (see Figure 6.9). Therefore, according to the density parameters, it enters the pipeline with a gas's density and exits with a liquid's density. On the other hand, case 24 has the positive calculated pressure gradient value (which is presented as negative in the graph). This can be explained as, despite of the phase transitioning phenomenon, case 24 has the highest mass flow rate (4.25 kg/s) compared to the other cases, which leads to a higher frictional pressure drop. The mass flow rate of a fluid is related to the frictional pressure drop through the conservation of energy principle, known as Bernoulli's equation, which relates the fluid's pressure, velocity, and elevation in a flow system. Since the mass flow rate is directly proportional to the velocity of the liquid, the frictional pressure drop is proportional to the square of the mass flow rate, which means that as the mass flow rate increases, the frictional pressure drop also increases. When the frictional pressure drop increases, the pressure of the fluid downstream of the pipeline decreases. This is because the fluid loses energy as it overcomes the increased resistance. As a result, the pressure drop across the pipeline increase, reducing the fluid's pressure downstream. Therefore, the pressure drop for case 24 gives a positive value according to the simulation results. The total average relative error is -24 %. The total standard deviation error of all cases is 38 %.

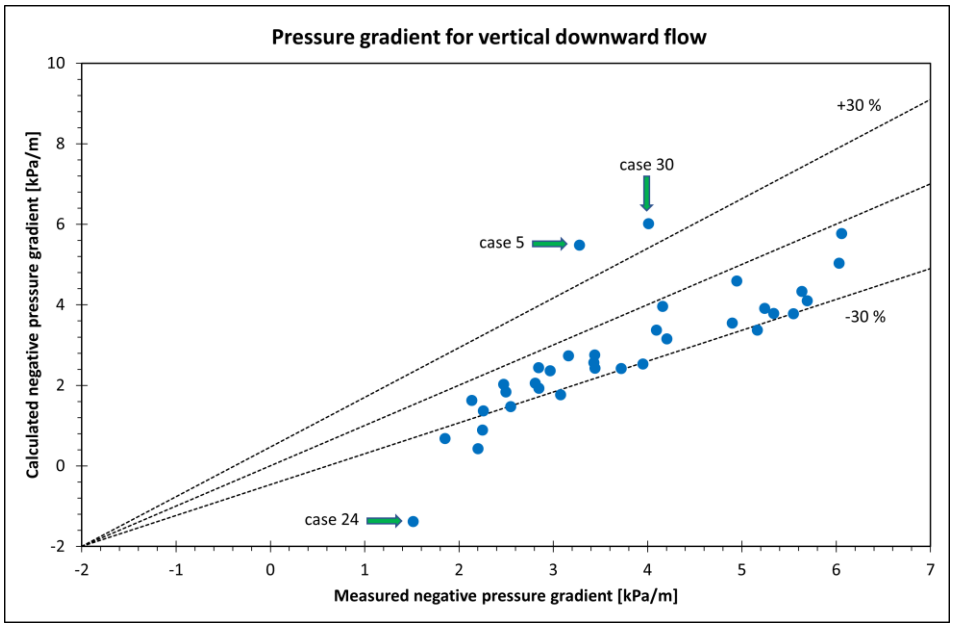

Figure 6.7: Measured negative pressure gradient vs. calculated for vertical downward flow in FlowManager^{TM}.

Figure 6.8 compares measured gas (a) and liquid (b) densities with calculated values at the pipeline's outlet. It has been discovered that the gas density from simulations is overestimated compared to the measured density, with the total average relative error for all 35 cases equal to 10 %. The calculated liquid density (b) is underestimated by around -26 %. Considerable underestimation of densities near the phase transition region strongly affects the pressure drop calculation results. This is what causes the deviation between calculated and measured pressure drops. The values are more accurate if there is no transition between phases. As a result, the liquid – to – gas density ratio ρ_l/ρ_g is 1.97, which is comparable less than experimental value.

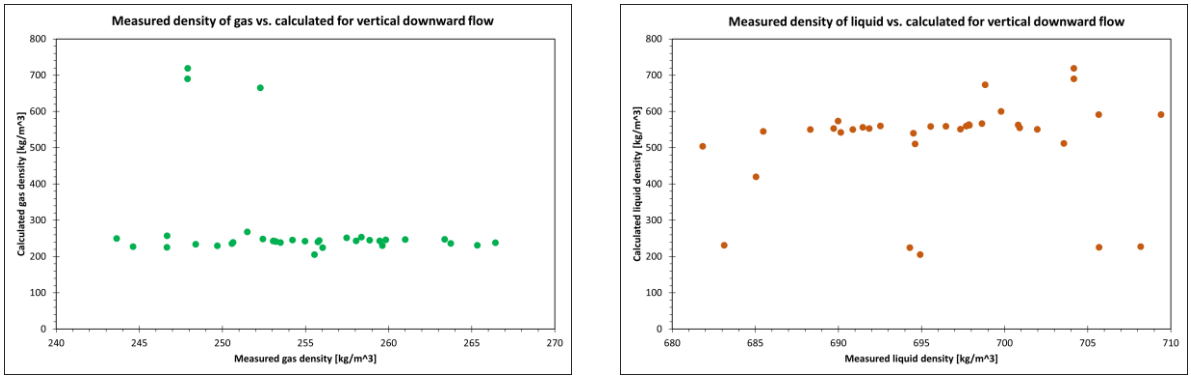

(a) (b)

Figure 6.8: Measured density of gas (a) and liquid (b) vs. calculated for vertical downward flow in FlowManager^{TM}.

Figure 6.9 shows the calculated densities of the gas (a) and liquid (b) at the pipeline's inlet and outlet. As seen, phase transitions from gas to liquid and liquid to gas occur as for the vertical

upward flow. Looking at the density of gas (a), for example, it can be seen that there is a sudden increase in density in cases 5, 30, and 32, where the flow enters the pipeline with the density of gas and exits with the density of the liquid. The density of the liquid (b) graph also shows that some cases have a sudden phase transition occurrence, and in some cases, such as cases 6 and 35, CO_2 has only one phase, gas.

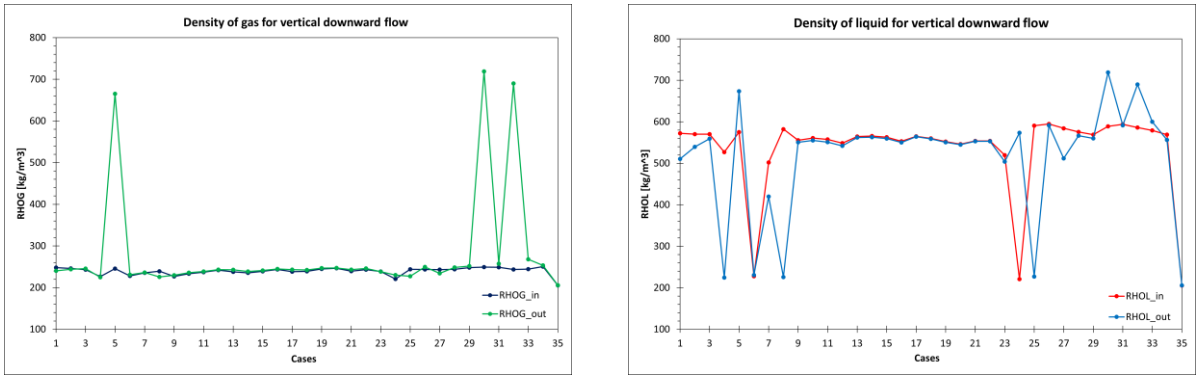

(a) (b)

Figure 6.9: Calculated density of gas (a) and liquid (b) vs. number of cases at the inlet and outlet of the vertical downward flow pipeline in FlowManager^{TM}.

Figure 6.10 illustrates the measured VFL versus the calculated. The calculated values are overestimated in all cases compared with the measured values. The total average relative error of overestimation for all cases is 8 %. The total standard deviation is 33 %. However, it should also be noted that in some cases, such as cases 6, 24, and 35 (pointed with arrows on the graph), the overestimation of calculated values equals 129 %, 55 %, and 155 %, respectively, by showing the highest deviation values. This is due to the phase transition concept shown in the density parameter. These 3 cases have a very low inlet liquid density. In the experiments, pure CO_2 always has a two – phase flow regime; however, from the simulation results, as observed, cases 6 and 35 appear in one phase flow which is gas.

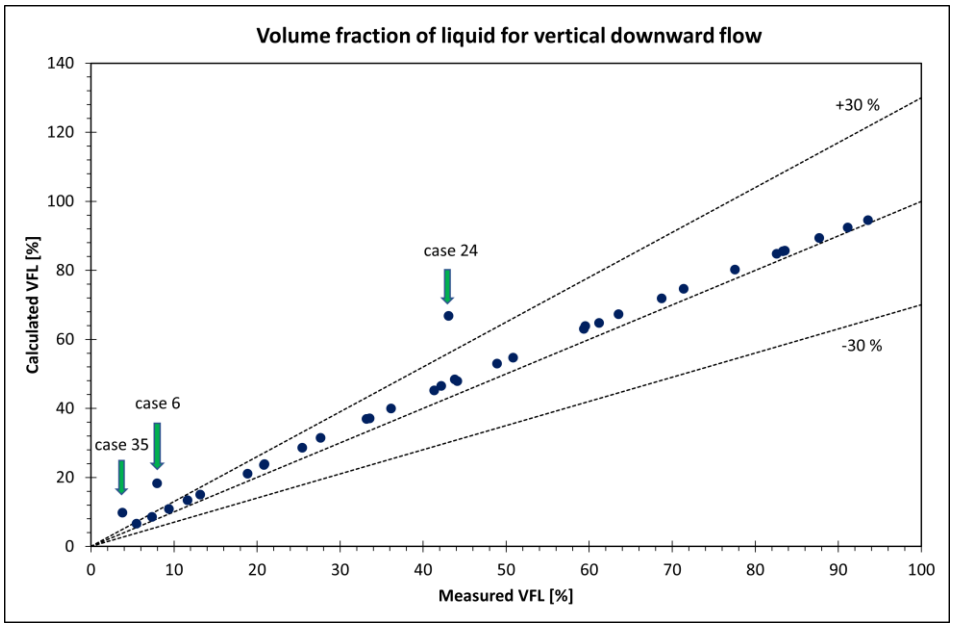

Figure 6.10: Measured volume fraction of liquid vs. calculated for vertical downward flow in FlowManager^{TM}.

6.3 Differences between upward and downward flow

Aside from differences in liquid gas ratio values, some differences in upward and downward flow can be observed. Figure 6.11 compares the measured pressure gradient (a) and VFL values (b) versus calculated data for upward and downward flow for all 35 cases calculated in FlowManager^{TM}. As can be seen, the pressure drop is more significant for upward flow, and the results are closer to the measured data. Compared to experimental data, both upward and downward results are underestimated in the pressure gradient but overestimated in VFL in both flow directions. It was discovered that the data for upward flow generally has closer results to the experimental data than the downward flow.

It should also be remarked that the experimental data for the pressure drop has ±7 % uncertainty. It was mentioned in the paper that the uncertainty could be increased for the downward flow, which may be related to flow – regime variations because friction and gravity have opposite effects in two flows. So that is also reasonable to have such deviations in the values for two different flow direction.

The measured volume fractions have an error of up to ±4 %. Because the uncertainty in the superficial liquid and superficial gas velocities is ±4 % and ±3 %, respectively, and VFL is superficial gas and superficial liquid dependent.

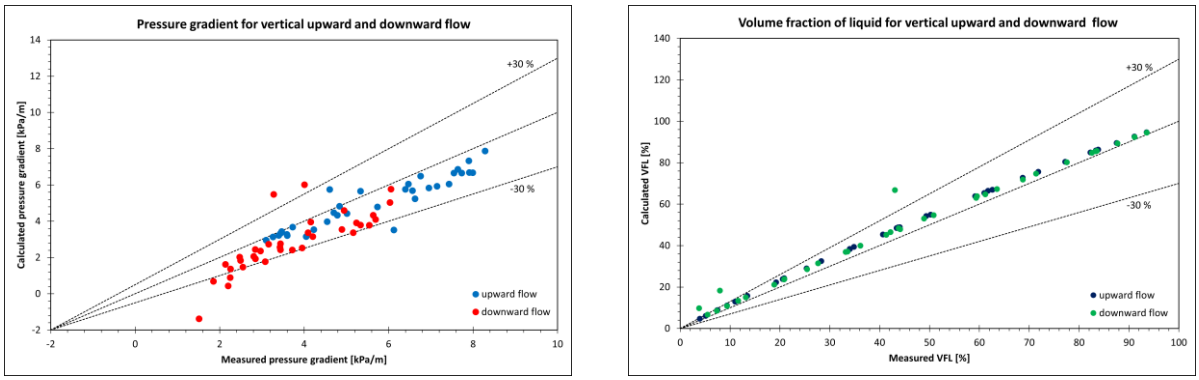

(a) (b)

Figure 6.11: Measured pressure gradient (a) and VFL (b) vs. calculated for upward and downward flow in FlowManager™.

6.4 Effect of impurities

In this section, CO_2 simulations with impurities are performed in FlowManager™ for vertical upward flow. The impurity has been chosen to be 10 % methane. Although experiments in the paper were not performed for CO_2 with impurities, its performance would be compared to that of pure CO_2 data. Because pure CO_2 does not have a phase envelope, the numerical method used in FlowManager™ faced instability depending on the density value, as stated above in section 6.2. And the primary objective of assessing the influence of impurities in the section is to see how the impurity affects CO_2 behavior and if there is a rapid "jump" from the single gas phase to the single liquid phase and vice versa.

The phase envelope for 90 % of CO_2 with 10 % CH_4 is shown in Figure 6.12. As can be observed, when CO_2 contains the impurity, the phase envelope expands, and the phase transition area increases. CO_2 exists in a two – phase flow regime under the blue curve, with the left side indicating a single liquid phase and the right side indicating a single gas phase. The critical point is located at around 23 °C and has a pressure of 79 bar. Above these numbers, CO_2 exists in a supercritical state, which implies it has the properties of both a gas and a liquid.

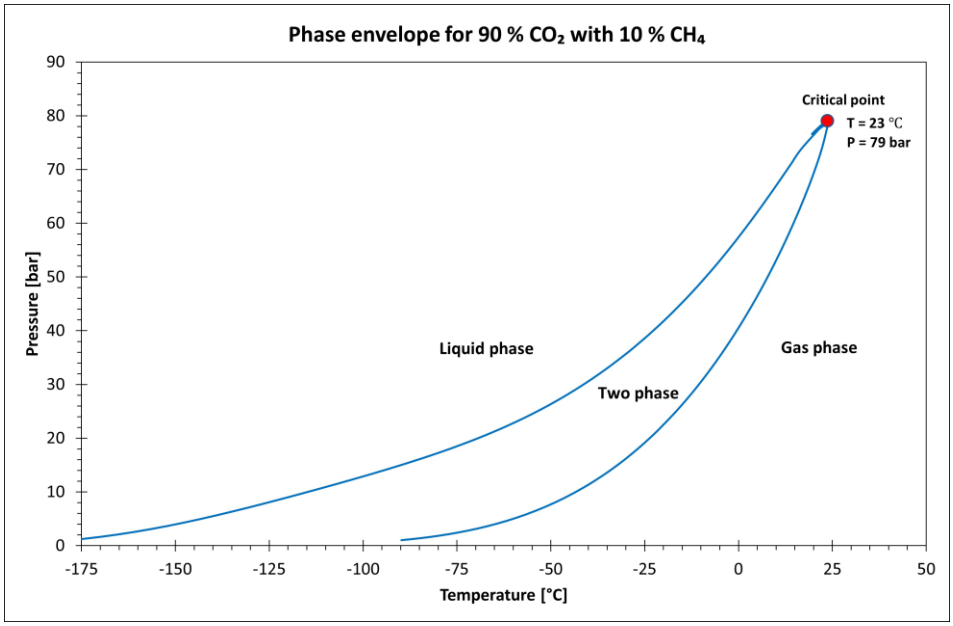

Figure 6.12: Phase envelope for 90 % CO_2 with 10 % methane.

The input values remained the same as for pure CO_2. PVT table was calculated in Multiflash, using 200 grids for temperature and pressure and the same EoS (RKS – HV) as for pure CO_2. The minimum temperature and pressure values are 15.55 °C and 1.01325 bar, respectively, and the maximum values are 27 °C and 67.4 bar. It should be noted that the bubble pressure values should be equivalent to the temperature and pressure values (200 points) for the simulation in FlowManager^{TM}; the simulations will not be performed due to missing bubble pressures. However, in this case, the bubble pressure values did not equal the temperature and pressure data. This is due to the maximum temperature of 27 °C, which is not conducive to creating a liquid – vapor phase boundary. CO_2 with methane will be in a gas phase at 27 °C and 67.4 bar pressure, and there will be no bubble pressure when CO_2 is in a single phase. Hence, the missing bubble pressure values must be filled with dummy values equal to 0.1E10 Pa (10 000 bar). The value was chosen based on the PVTsim computations [165]. Multiflash leaves the dummy value unfilled, while PVTsim fills it with the value.

As previously stated, the experiments were conducted at 25 °C to 27 °C and pressures ranging from 65 bar to 67 bar, where pure CO_2 will exist in a two – phase flow regime. However, under these conditions, CO_2 with 10 % methane as an impurity will exist in a single gas phase. Therefore, regardless of the differences in CO_2 phase existence, the parameters such as pressure drop, and density are compared below.

Figure 6.13 illustrates the pressure gradient vs. the number of cases for 90 % CO_2 with 10 % methane and pure CO_2. As can be seen, when CO_2 has impurities, the pressure drop is more significant than when CO_2 is pure. This is caused by the fact that pressure is significantly higher in the pipeline's output. Impurities in the gas increase its viscosity, resulting in more considerable frictional losses along the pipeline's length. This higher frictional loss will result in an increase in pressure drop at the pipeline's exit. Impurities in the gas also reduce its density. Lower gas density can lead to increased gas velocities, which can increase turbulence and cause pressure losses.

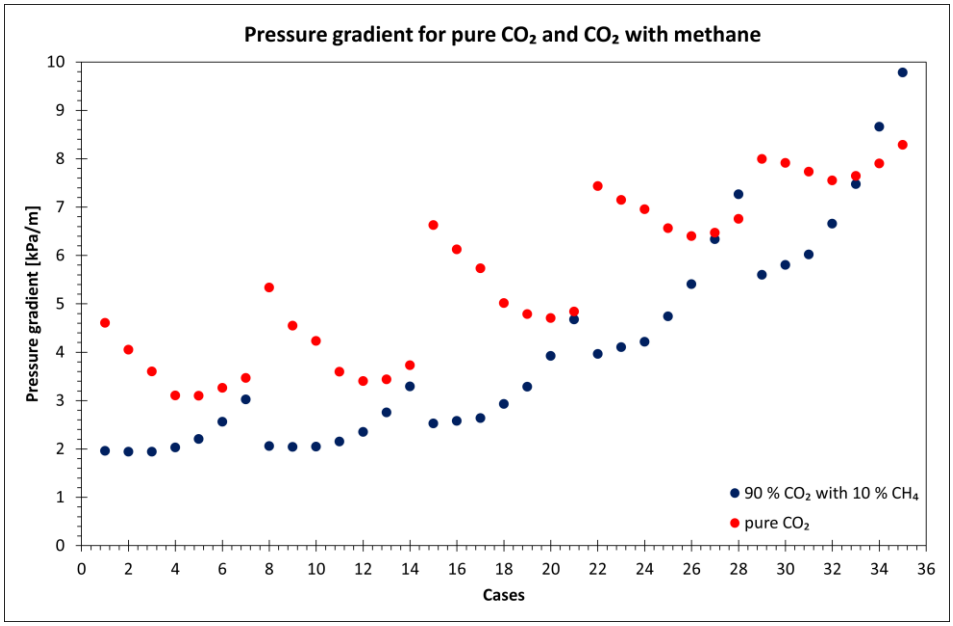

Figure 6.13: Measured pressure gradient for pure CO_2 and calculated 90 % CO_2 with 10 % methane vs. number of cases.

Figure 6.14 represents the gas density at the pipeline's input and output for CO_2 with 10 % methane and the gas density at the inlet of the pipeline for pure CO_2 vs. the number of cases. The pipeline's input and output density does not vary significantly, yielding a relatively constant number when CO_2 has an impurity. However, its density reduces significantly compared to pure CO_2. This is because the molar masses of the two gases differ. Methane has a molar mass of roughly 16 g/mol, whereas CO_2 has a molar mass of about 44 g/mol. This indicates that a mixture of 90 % CO_2 and 10 % methane will have a lower average molar mass than pure CO_2, resulting in a lower density. Furthermore, methane could impact the intermolecular interactions between the CO_2 molecules in the mixture, contributing to a decrease in density. Because methane is a smaller molecule than CO_2, its presence in the mix can disrupt the regular packing of CO_2 molecules, diminishing their overall attraction and lowering the density of the mixture. The density of a gas mixture is also affected by its temperature and pressure. At higher temperatures and lower pressures (as in this case), the gases tend to occupy more space, resulting in a reduced density of the combination.

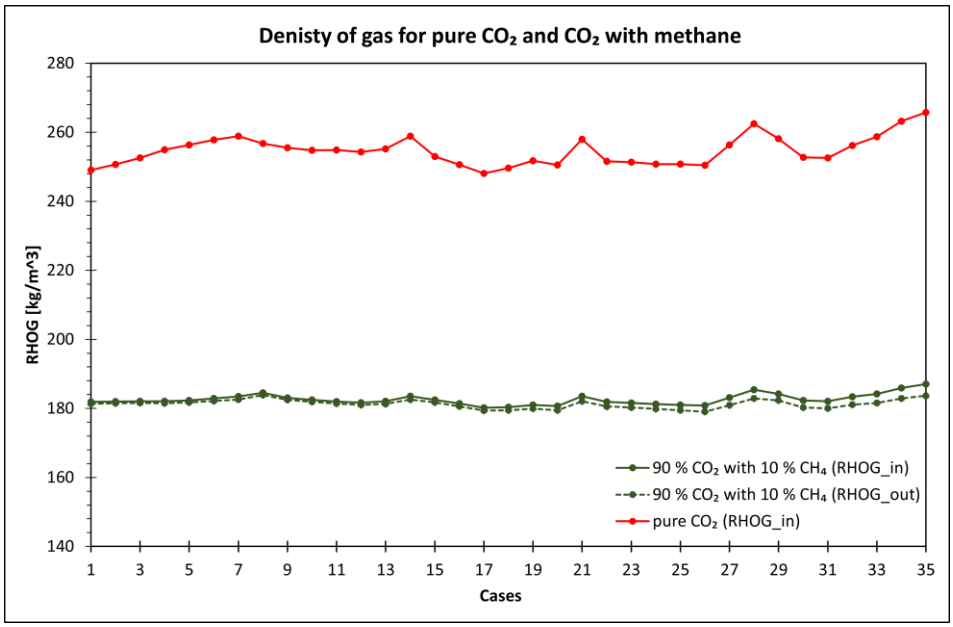

Figure 6.14: Calculated density of gas at the pipeline inlet and outlet for 90 % CO_2 with 10 % methane and measured density of gas at the pipeline outlet for pure CO_2 for vertical upward flow in FlowManager^{TM}.

6.5 Results from OLGA

6.5.1 Vertical upward flow

Figure 6.15 represents the measured pressure gradient vs. the calculated vertical upward flow for 35 experimental cases. The total average relative error for all calculated 35 cases is overestimated to 5 %. The total standard deviation is 8 %. The highest overestimated value among all 35 cases is 23 %. However, it can be observed that the values for all cases are located within the +30 % and -30 % lines. There are several cases where calculated and measured data from the experiments have a relative error value of 0 %, such cases are located precisely on the line represented in the middle (0 % deviation line).

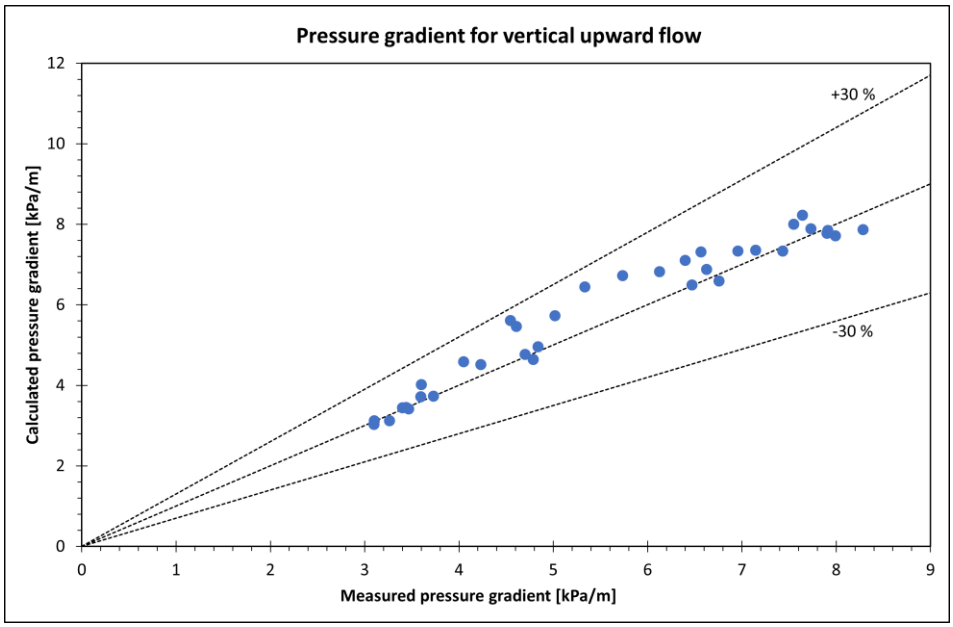

Figure 6.15: Measured pressure gradient vs. calculated for vertical upward flow in OLGA.

Figure 6.16 plots the measured density of the gas (a) and liquid (b) vs. calculated data at the pipeline's outlet for 35 cases. The calculated densities show results similar to the measured densities, with a total average relative error of 0 % for both. However, there are some data differences in some cases. For example, the highest overestimated and underestimated deviations in gas density are 2 % and -1 %, respectively. The highest overestimated and underestimated deviation values for liquid density are 1 % and -1 %, respectively. The liquid – to – gas ratio ρ_l/ρ_g equals 2.74.

Moreover, the calculated density at the inlet and outlet of the vertical pipeline for gas (a) and liquid (b) are represented in Figure 6.17. As shown, gas density is higher at the pipeline inlet and decreases at the pipeline outlet in all 35 cases. However, liquid density is lower at the inlet of the pipeline and higher at the outlet, and there are no changes in the phases of CO_2.

The gas density is higher at the inlet and lower at the outlet when the pipeline flows vertically upward. Because CO_2 density is proportional to pressure, it will be higher at the bottom (inlet) of the pipeline, where the pressure is higher, and lower at the top (outlet), where the pressure is lower. The pressure decreases as the CO_2 flows upward, causing the CO_2 to expand. As a result of this expansion, the density of CO_2 at the outlet is lower than at the inlet. For liquid flow in a vertical upward pipeline, on the other hand, the density is lower at the inlet and higher at the outlet because the pressure decreases from the bottom of the pipeline to the top, resulting in a lower density at the inlet and a higher density at the outlet. Furthermore, the liquid settles at the bottom of the pipeline due to the force of gravity acting on it, resulting in a higher density at the bottom of the pipeline and a lower density at the top of the pipeline where the liquid is moving against the force of gravity.

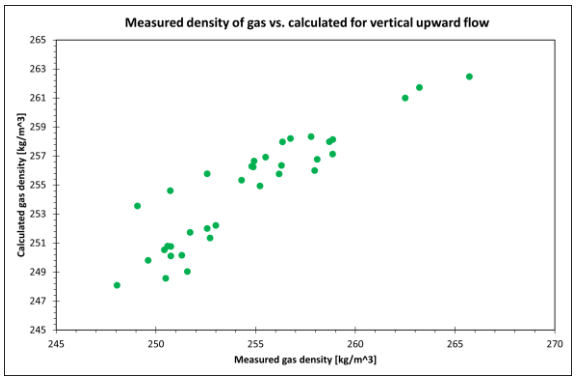

(a)

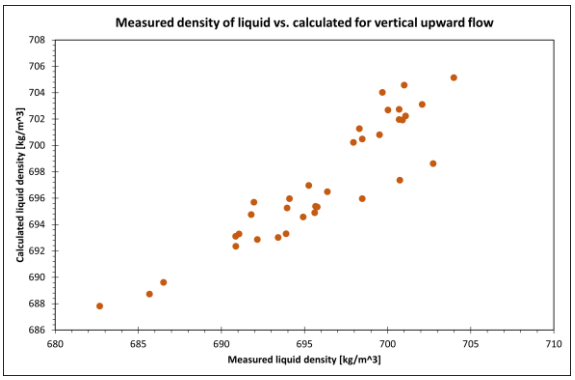

(b)

Figure 6.16: Measured density of gas (a) and liquid (b) vs. calculated for vertical upward flow in OLGA.

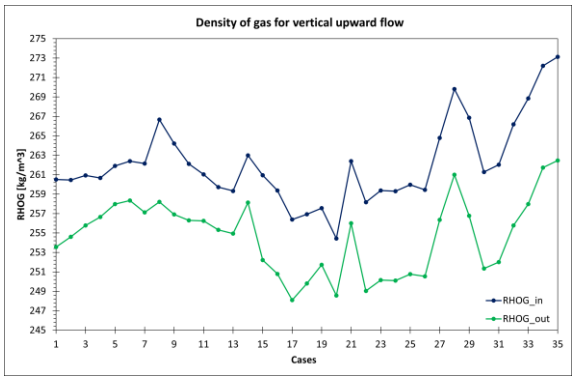

(a)

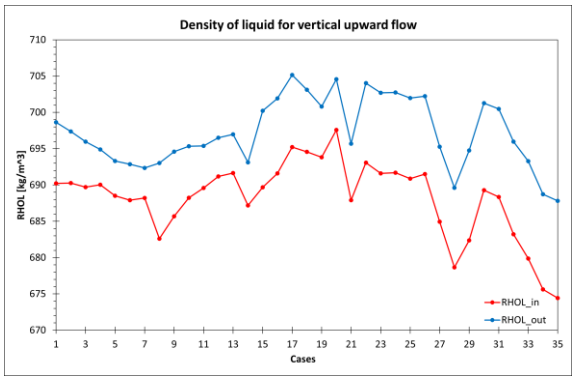

(b)

Figure 6.17: Calculated density of gas (a) and liquid (b) vs. number of cases at the inlet and outlet of the vertical upward flow pipeline in OLGA.

Figure 6.18 compares the measured versus calculated VFL for 35 cases. The total average relative error is 0 % and the total standard deviation is 1 %. The highest and lowest overestimated and underestimated values among 35 cases are 1 % and -1 %, respectively. Since the volume fraction is density – dependent, this is due to the small deviations in densities for gas and liquid.

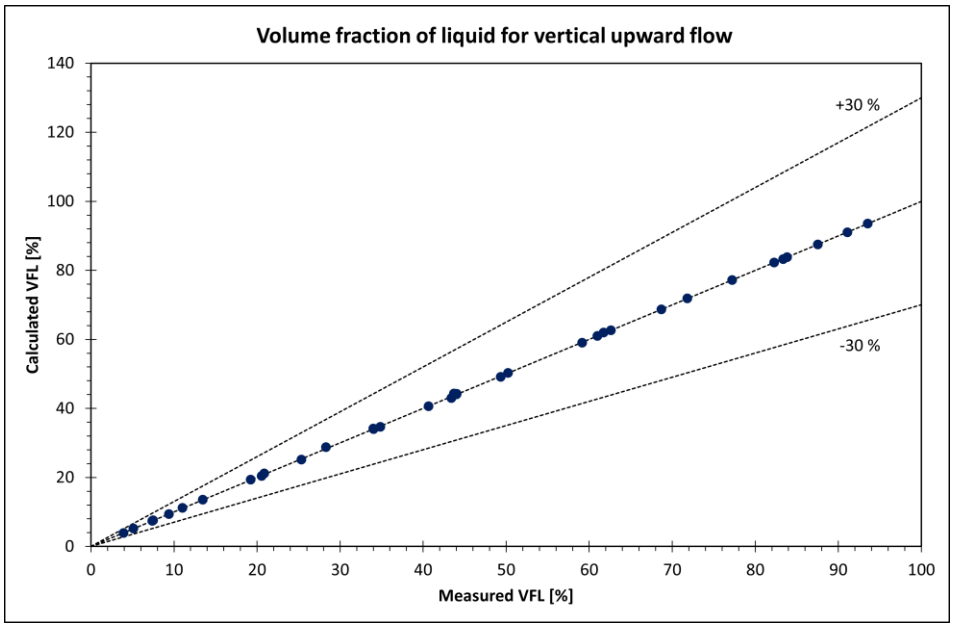

Figure 6.18: Measured volume fraction of liquid vs. calculated for vertical upward flow in OLGA.

6.5.2 Vertical downward flow

The measured negative pressure gradient vs. the calculated pressure gradient for 35 experimental cases for downward flow is represented in Figure 6.19. The graph shows that the calculated pressure gradient is overestimated, with a total average relative error of 0 %. The total standard deviation is 20 %. The highest calculated overestimated value is 48 % for case 22, and the highest underestimated value is -42 % for case 18 (pointed with an arrow on the graph). Cases 17 and 21 are overestimated by 31 % and 32 %, respectively, and located outside the 30 % line.

The calculated and measured frictional pressure drop analyses revealed that the calculated values are overestimated by 25 % to 40 % for cases outside the +30 % line. The pressure drop increases as the frictional drop along the vertical pipeline increases. This is because frictional pressure drop is one component of total pressure drop. As a result, the total pressure decrease along the pipeline will be more significant than the measured data.

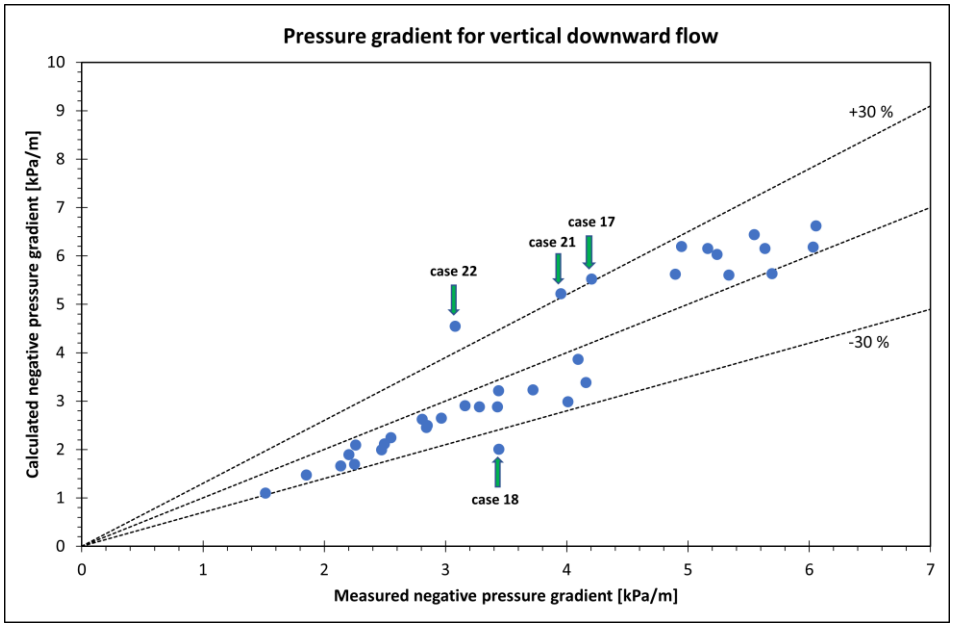

Figure 6.19: Measured negative pressure gradient vs. calculated for vertical downward flow in OLGA.

The measured densities for gas (a) and liquid (b) at the pipeline's outlet vs. calculated data are plotted in Figure 6.20. The inlet and outlet density of the gas (a) and liquid (b) at the pipeline is shown in Figure 6.21. The calculated density of the gas is overestimated, with a total average relative error of 2 %. In comparison, the calculated density of the liquid is underestimated with a total average relative error of -1 %. The liquid – to – gas ratio ρ_l/ρ_g equals 2.67.

When CO_2 with two phases flows downward in a vertical pipeline, the density of the gas phase will be lower than that of the liquid phase. For example, from Figure 6.21, it can be observed that the density of the gas is lower at the inlet and higher at the pipeline outlet. However, for the density of the liquid, the inlet density is higher than the outlet. This is because as the two – phase mixture enters the pipe at the inlet, the liquid phase usually dominates due to the higher density of the liquid. The gas phase is typically dispersed in the liquid phase as tiny bubbles. As the mixture moves down the pipe, due to gravity, the liquid phase settles towards the bottom of the pipe while the gas phase rises to the top. As a result, the gas bubbles become more extensive and merge, forming a gas phase with higher density towards the pipe outlet. Furthermore, the pressure drop along the pipeline can also cause the gas bubbles to compress, leading to an increase in gas density which can lead to further separation of the liquid and gas phases, resulting in a decrease in liquid density.

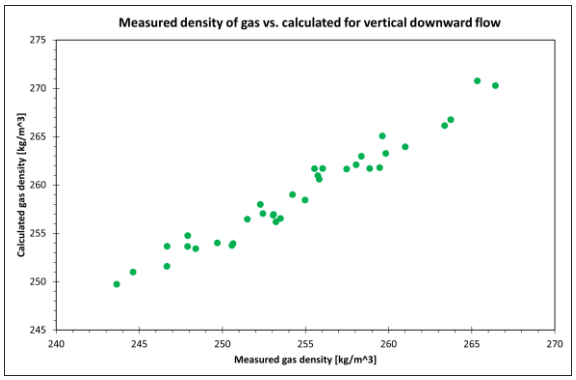

(b)

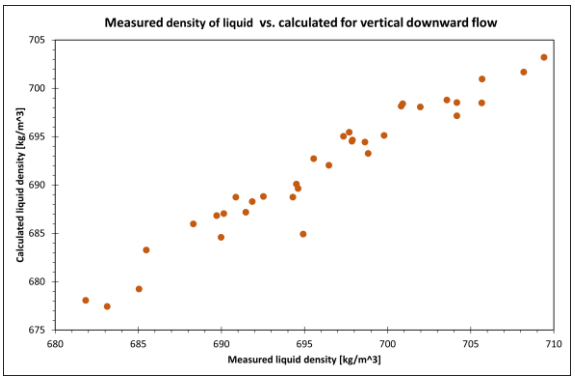

(b)

Figure 6.20: Measured density of gas (a) and liquid (b) vs. calculated for vertical downward flow in OLGA.

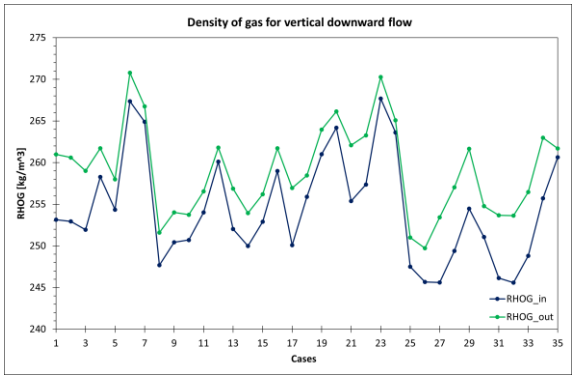

(a)

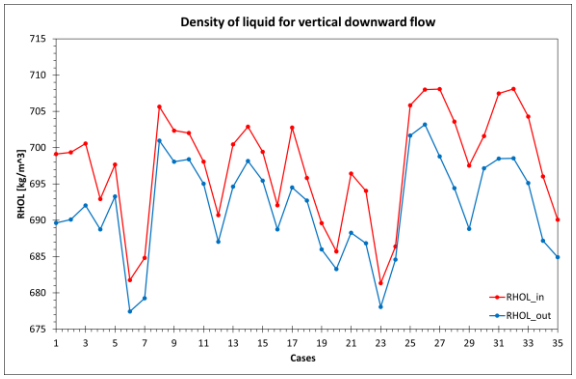

(b)

Figure 6.21: Calculated density of gas (a) and liquid (b) vs. number of cases at the inlet and outlet of the vertical downward flow pipeline in OLGA.

Figure 6.22 represents the measured VFL vs. calculated data for 35 cases. The total average relative overestimation error from the measured value is 1 %. The total standard deviation is equal to 1 %.

A better match between calculated and experimental density has a big effect on improving the pressure gradient predictions and volume fraction predictions from the model.

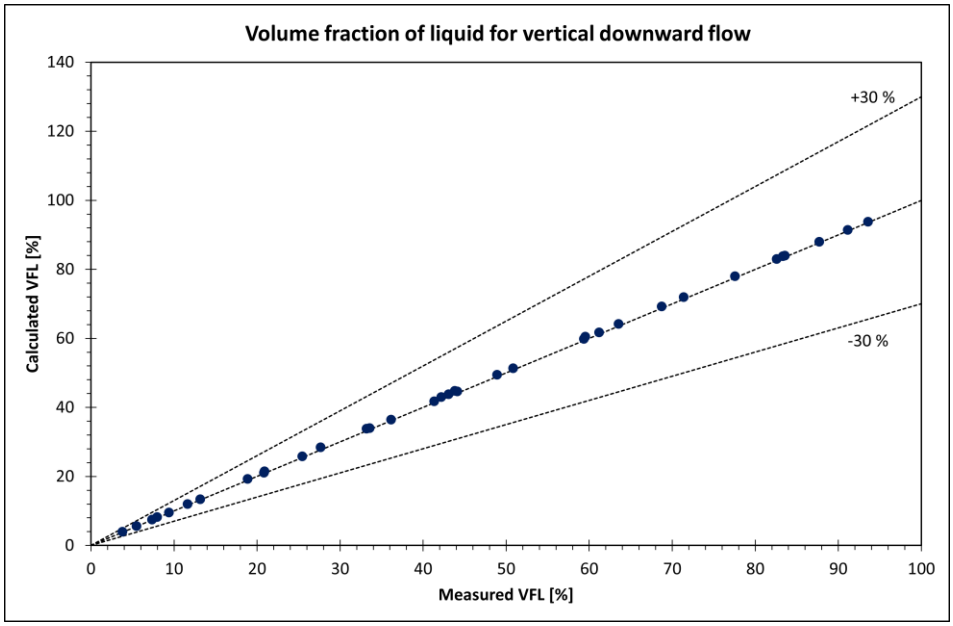

Figure 6.22: Measured volume fraction of liquid vs. calculated for vertical downward flow in OLGA.

6.6 Comparison of results from FlowManager™ and OLGA

Figure 6.23 compares calculated pressure gradients from FlowManager™ and OLGA simulations to experimental data for the vertical upward (a) and downward flow (b) for CO_2 in a two – phase flow regime. As can be seen, the results from FlowManager™ underestimate the pressure gradient; however, the OLGA simulation results are overestimated when compared to experimental data for the vertical upward flow. For the vertically downward flow, calculated values from both software are underestimated compared to experimental data.

The calculated values from OLGA match the experiments better regarding pressure drop for both flow directions by showing a lower total average relative error (5 % for upward flow and 0 % for downward flow). As previously stated, the difference in pressure gradient in FlowManager™ happens due to the phase transition phenomena of CO_2, which changes the phase from two – phase to a single gas or liquid.

Figure 6.24 depicts a VFL comparison for vertical upward flow (an) and vertical downward flow (b) calculated in FlowManager™ and OLGA. The calculated VFL from OLGA yields the best results in both flow directions. This is due to OLGA's superior density performance. As seen from the OLGA results (discussed earlier), there is no phase transition of CO_2; it always appears in a two – phase flow regime, and the liquid/gas ratio is closer to what the experiments have revealed.

However, the results in FlowManager™ revealed a sudden phase transition phenomenon where CO_2 changed from two phases to a single gas or liquid. Hence there were sudden changes in density values. For example, for the downward flow in the results of pressure gradient from FlowManager™, there are cases outside the 30 % and -30 % range. This is because a phase transition occurred in these cases. Since the VFL calculation depends on the densities, considerable deviations in the results happen.

When CO_2 is pure (100 %), and in a two – phase flow regime (along the line on the phase diagram of pure CO_2), PVT from Multiflash based on PT calculations provides poor density performance in both flow directions. However, in OLGA, the calculations were based on the PH calculation, which allowed for the accurate estimation of gas and liquid density.

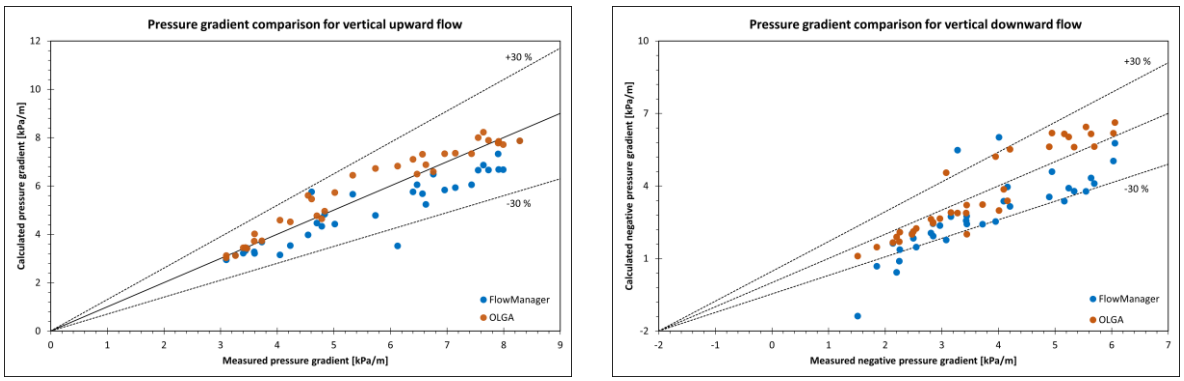

(a) (b)

Figure 6.23: Comparison of measured pressure gradient vs. calculated for vertical upward (a) and vertical downward flow (b) in FlowManager™ and OLGA.

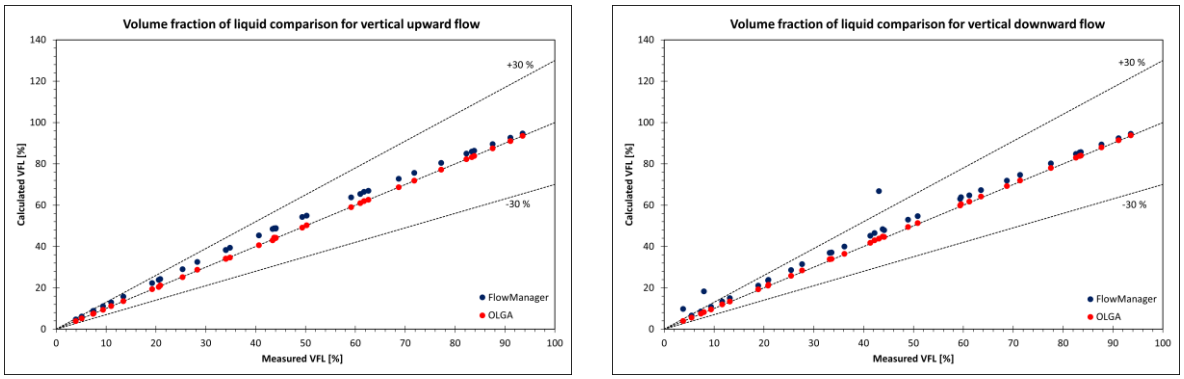

(a) (b)

Figure 6.24: Comparison of measured VFL vs. calculated for vertical upward (a) and vertical downward flow (b) in FlowManager™ and OLGA.

6.7 Evaluation of different EoS for experimental setup 2

As for experimental setup 1, the effect of PVT tables using different EoS on simulations has been analyzed. The average relative error (in pressure gradient) of the calculated pressure gradient value to the experimental data has been calculated using Equation 6.1. Table 6.2 summarizes the calculated results.

Table 6.2: Average relative error of pressure gradient for different EoS in experimental setup 2.

Cases	GERG-2008	PR	PR – HV	RKS	RKS – HV	PSRK	PR 78	RKS Advanced
Gas phase_1	-50 %	-50 %	-50 %	-49 %	-50 %	-49 %	-50 %	-50 %
Gas phase_2	-46 %	-47 %	-47 %	-46 %	-46 %	-46 %	-47 %	-46 %
Liquid phase_3	-40 %	-39 %	-38 %	-31 %	-36 %	-31 %	-38 %	-36 %
Liquid phase_4	-48 %	-47 %	-46 %	-40 %	-45 %	-40 %	-46 %	-45 %
Two-phase_5	-43 %	-42 %	-42 %	-38 %	-40 %	-38 %	-42 %	-40 %

Using PVT tables based on different EoS does not give much improvement to pressure gradient predictions. Therefore, it was decided to analyze other parameters from the simulations in order to understand why such considerable deviations in pressure gradient values happen. The parameter chosen is the density parameter. Although the densities were not measured during the experiments, the calculated density parameters from simulations were compared with the NIST data. NIST is part of the U.S. Department of Commerce and one of the oldest physical science laboratories, which provides measurement support and standards for small and big industries [166]. These results are outlined in the next section.

6.8 Results from FlowManager™ and OLGA

6.8.1 Density evaluation

According to the results of Calsep's research [158], the EoS GERG – 2008 is the best and most accurate choice for PVT calculations of CO_2. Further investigations will be undertaken by applying the GERG – 2008 EoS for calculating PVT table as the input file to FlowManager™. The density at the pipeline's inlet, PI30 at 0 m and PI50 at 100 m have been compared.

Figure 6.25 illustrates the comparison of inlet and outlet density for cases 1 and 2 (a), 3 and 4 (b), and 5 (c) and indicates the average relative error (%) from both software compared to NIST data. Data from NIST is used to compare measured values. As shown in graph (a), which compares the inlet and outlet gas density for cases 1 and 2 (CO_2 is in a single gas phase), the highest overestimated relative error value is 2 %. The calculated values from both software are reasonably close to the NIST data. In graph (b), the inlet and outlet liquid density for cases 3 and 4 (CO_2 is in a single liquid phase) were compared, with the maximum overestimated relative error value reaching 1 % and the maximum underestimating value having -1 %. The input and output densities of gas and liquid have been compared in graph (c) for case 5 (CO_2

in a two-phase). As can be observed, the highest overestimated relative error value is 1 %, and the lowest underestimated value is -5 %.

Regarding the results, the relative error between NIST data and simulations is small when CO_2 is in a single gas or liquid phase, except in case 5, where CO_2 is in a two – phase flow, particularly the values of inlet gas density. The reason for having the largest underestimated relative error is that according to the NIST data, a saturation of vapor and liquid at a temperature of 9.12 °C occurs at a pressure of 44.05 bar, but according to the experiments, the pressure is equivalent to 43.11 bar. The higher the pressure at the inlet, the higher the gas density. Having somewhat different inlet pressure values results in such variations.

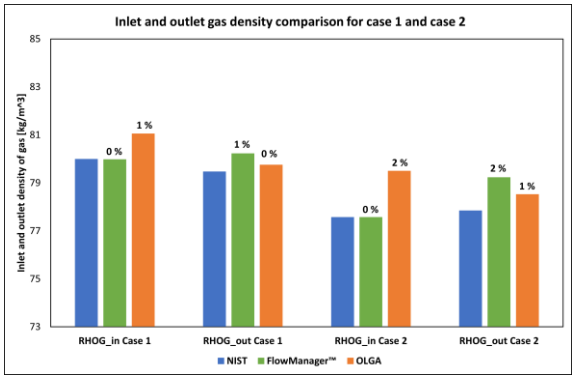

(a)

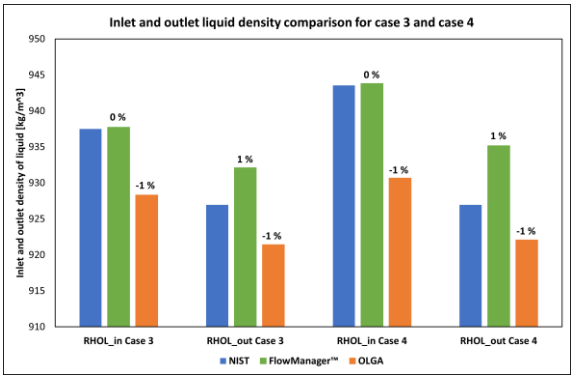

(b)

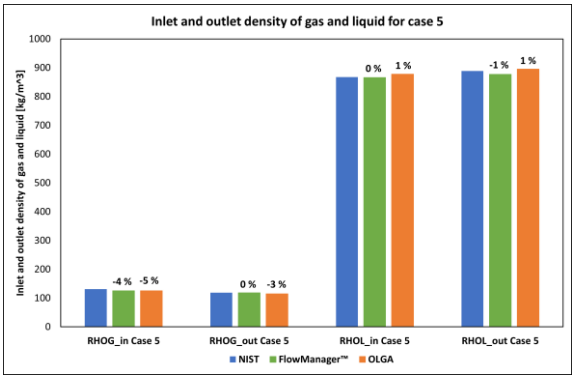

(c)

Figure 6.25: Average relative error of densities from FlowManager^{TM} and OLGA compared to NIST data for cases 1 and 2 (a), 3 and 4 (b), and 5 (c).

The density changes from FlowManager^{TM} and OLGA along the 138 m horizontal pipeline are shown in Table 6.3 and Table 6.4 for cases 1 and 2. The values have been measured at the inlet, 100 m, and outlet.

By analyzing the results, it was observed that the density of CO_2 in case 1 and case 2 from FlowManager^{TM} is increasing and decreasing at various points along the pipeline. It increases in the pipeline at 100 m and falls again at the pipeline outlet at 138 m. This is because the pressure decrease within 100 m is so small that it can be considered as constant pressure.

According to the Figure 3.4 and Figure 3.5 in Section 3, the density of CO_2 will increase with decreasing temperature given constant pressure. Given constant temperature and decreasing pressure, the density of CO_2 will decrease. As a result, as the pressure drop at the pipeline's outlet decreases, the density of CO_2 begins to decrease.

Table 6.3: Density changes from FlowManager™ and OLGA along the pipeline for case 1.

Case_1	**RHOG at 0 m**	**RHOG at 100 m**	**RHOG at 138 m**
[-]	**[kg/m^3]**	**[kg/m^3]**	**[kg/m^3]**
FlowManager™	79.98	80.22	79.81
OLGA	81.05	79.75	78.95

Table 6.4: Density changes from FlowManager™ and OLGA along the pipeline for case 2.

Case_2	**RHOG at 0 m**	**RHOG at 100 m**	**RHOG at 138 m**
[-]	**[kg/m^3]**	**[kg/m^3]**	**[kg/m^3]**
FlowManager™	77.56	79.22	78.89
OLGA	79.49	78.52	77.71

6.8.2 Pressure evaluation

Figure 6.26 below shows the measured pressure gradient in the flow loop between 0 m and 100 m and the calculated values from FlowManager™ and OLGA. As can be seen, the measured values for each case are significantly higher than the calculated values. Hence, the calculated values are underestimated to more than -30 %. Furthermore, the calculated values from both software produce substantially identical results for the four cases with the single phase flow. However, although the findings from OLGA for Case 5 are found between the 30 % and -30 % ranges, giving a closer result to the measured data, the results from FlowManager™ are located outside of the range, resulting in considerable underestimation.

Because the results from both simulators are similar for pure CO_2 in a single gas and single liquid phase, it was decided to verify the accuracy of the pressure readings from the sensors during the experiments.

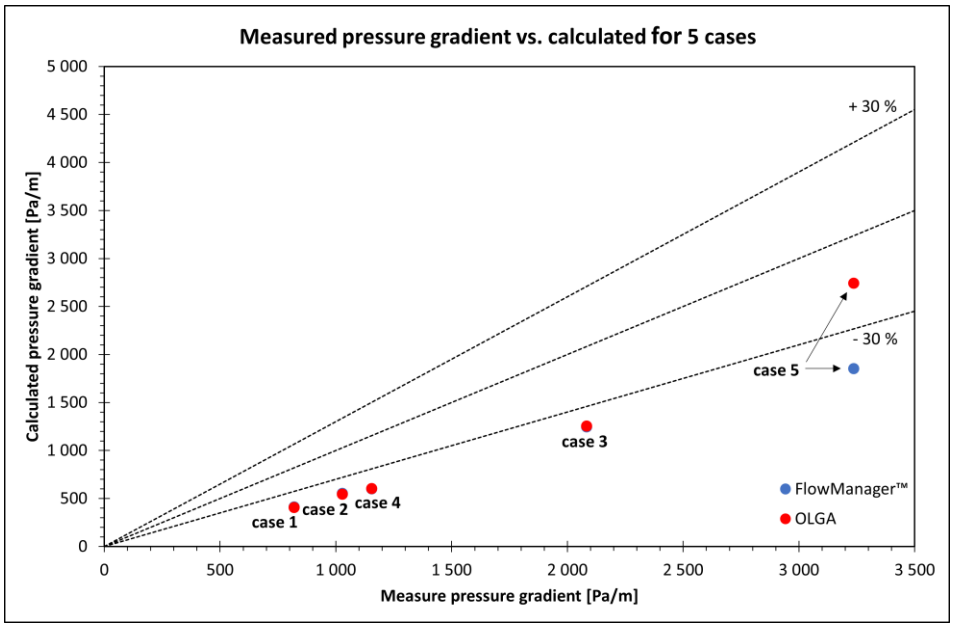

Figure 6.26: Measured pressure gradient vs. calculated from FlowManager™ and OLGA.

According to SINTEF's observations and feedback, the performance of the pressure sensors after 5 years of usage increases measurement uncertainty by up to 35 %, mainly when the pressure drop between sensors is relatively small.

The sensors from PI30 to PI60 installed on the horizontal circuit have an accuracy of 0.044 %. However, the manufacturer reports that after 5 years of use, the performance is predicted to drop to 0.125 %. As a result, the sensors' measurements now have an uncertainty of ±0.17 bar. This is particularly significant for calculating pressure drops since the difference in pressure between any two sensor readings can be off by up to 0.35 bar.

This is most likely happening in zero – flow conditions, where pressure differences in the order of 0.32 and 0.21 bar are observed. The difference falls within the uncertainty mentioned above range. Such variation can account for up to 35 % of the overall drop in pressure under current circumstances.

7 Conclusion

Analyzing the results of experiment 1, it can be concluded that when CO_2 is pure, it does not have a phase envelope where a two – phase flow regime can occur. As was observed from the phase diagram of pure CO_2; it has a phase transition line between the different physical phases. Hence, applying numerical calculations precisely on the line where the experiments were taken is complicated based on PT calculations. According to the calculations in FlowManager™, applying the PVT table from Multiflash results in poor density performance in both flow directions since CO_2 changes phase from single liquid to a single gas and vice versa resulting in having different densities at the inlet and outlet of the pipeline. Such large jumps from one phase to another in densities were caused by even little changes in temperature and pressure. However, in OLGA, the calculations were based on the PH calculation, which allowed for the accurate estimation of gas and liquid density. There was no observed phase transition phenomenon; hence the pressure drop calculations performed better. A better match between calculated and experimental density significantly improved the pressure gradient predictions and volume fraction predictions from the model.

Analyzing the results of experiment 2, it was observed that there was an inconsistency between measured and calculated data from both software, with the calculated data underestimating the measured data by up to -50 %. However, by studying calculated results gathered from FlowManager™ and OLGA it have been noticed that when pure CO_2 is in a single gas or in a single liquid phase the data were extremely similar. Furthermore, it can be concluded that the calculation applying the PVT table from Multiflash when pure CO_2 is in a single phase provides results that are pretty close to the simulation results from OLGA, based on PH calculation. However, results from the study of pure CO_2 in two – phase flow differ. Hence, they must be compared to the experimental data. In addition to the pressure gradient analysis, the calculated densities of CO_2 gas and CO_2 liquid from each software were evaluated with the NIST data. As a consequence, the relative error between calculated values from FlowManager™ and OLGA compared to the NIST data was considerably small.

According to SINTEF's findings, the performance of pressure sensors after 5 years of use increased measurement uncertainty by up to 35 %, mainly when the pressure drop between sensors is minor, as was the case in the study. Despite efforts to linearize the measurement results, the uncertainty is too significant to give a meaningful comparison with the simulated values. As a result, the results of the FlowManager™ and OLGA cannot be compared with measured data throughout the thesis time. As concluded, SINTEF will repeat the experiments for pure CO_2 in different phases, but this time with a differential pressure device that monitors how much the pressures in two points of the test section differ. As discovered during the studies, such a solution is better suited for small pressure drops. After getting measured data, the results will be compared to those acquired from the two simulators in this work as investigation will help to better understand the phenomenon under study. Further work with new experimental data will be completed by TechnipFMC.

Even though the studies were only conducted on pure CO_2, the effect of impurities on the PVT characteristics of CO_2 was also investigated. The study discovered that a small quantity of impurities increases the phase envelope of CO_2 where it is in a two – phase flow. Therefore, the more impurities CO_2 has the more expansive the area of the two – phase flow regime.

Using a low concentration of impurity is recommended to improve simulation results in FlowManager^{TM} applying PT calculations where a numerical approach might be appropriately used. If SINTEF carries out any CO_2 experiments with impurities in the future, it is recommended to do a similar comparison with simulations.

Simulating pure CO_2 in a two – phase flow regime is quite challenging due to the simultaneous presence of both liquid and gas phases. In addition, the behavior of each phase can be extremely different, resulting in complicated interactions between the two phases. One difficulty is that CO_2's behavior depends on its thermodynamic state and is extremely sensitive to slight changes in temperature and pressure. Furthermore, there is a significant mass transfer between the liquid and gas phases in a two – phase flow, which can impact the behavior of both phases. Overall, simulating pure CO_2 in a two – phase flow regime requires careful consideration of the thermodynamic state of the CO_2 as well as accounting for mass transfer between the liquid and gas phases. Because of its complexity, precisely modeling and predicting the behavior of CO_2 in such systems can be difficult.

References

[1] G. C. Change. "Carbon Dioxide." https://climate.nasa.gov/vital-signs/carbon-dioxide/ (accessed.

[2] IPCC. "Climate Change 2022." https://www.ipcc.ch/report/ar6/wg3/downloads/report/IPCC_AR6_WGIII_FullReport.pdf (accessed.

[3] I. GHG. "Net Zero by 2050." https://iea.blob.core.windows.net/assets/deebef5d-0c34-4539-9d0c-10b13d840027/NetZeroby2050-ARoadmapfortheGlobalEnergySector_CORR.pdf (accessed.

[4] UNFCCC. "Key aspects of the Paris Agreement." https://unfccc.int/most-requested/key-aspects-of-the-paris-agreement (accessed.

[5] T. G. C. Institute. "Global Status of CCS 2021." https://www.globalccsinstitute.com/wp-content/uploads/2021/10/2021-Global-Status-of-CCS-Report_Global_CCS_Institute.pdf (accessed.

[6] J. Wang, D. Ryan, E. J. Anthony, N. Wildgust, and T. Aiken, "Effects of impurities on CO2 transport, injection and storage," *Energy Procedia,* vol. 4, pp. 3071-3078, 2011.

[7] M. Hammer, H. Deng, L. Liu, M. Langsholt, and S. T. Munkejord, "Upward and downward two-phase flow of CO2 in a pipe: Comparison between experimental data and model predictions," *International Journal of Multiphase Flow,* vol. 138, p. 103590, 2021.

[8] D. Y. Leung, G. Caramanna, and M. M. Maroto-Valer, "An overview of current status of carbon dioxide capture and storage technologies," *Renewable and Sustainable Energy Reviews,* vol. 39, pp. 426-443, 2014.

[9] E. Commission. "Taxonomy Report: Technical Annex." https://finance.ec.europa.eu/system/files/2020-03/200309-sustainable-finance-teg-final-report-taxonomy-annexes_en.pdf (accessed.

[10] E. Commission. "A Clean Planet for all " https://eur-lex.europa.eu/legal-content/EN/TXT/PDF/?uri=CELEX:52018DC0773 (accessed.

[11] N. M. o. P. a. Energy, "Longship—Carbon Capture and Storage," 2020. [Online]. Available: https://www.regjeringen.no/contentassets/943cb244091d4b2fb3782f395d69b05b/en-gb/pdfs/stm201920200033000engpdfs.pdf

[12] G. C. Institute. "Global Status of CCS Report: 2019." https://www.globalccsinstitute.com/resources/publications-reports-research/global-status-of-ccs-report-2019/ (accessed.

[13] E. Blomen, C. Hendriks, and F. Neele, "Capture technologies: improvements and promising developments," *Energy procedia,* vol. 1, no. 1, pp. 1505-1512, 2009.

[14] H. Yang *et al.*, "Progress in carbon dioxide separation and capture: A review," *Journal of environmental sciences,* vol. 20, no. 1, pp. 14-27, 2008.

[15] L. Raynal *et al.*, "The DMX™ process: an original solution for lowering the cost of post-combustion carbon capture," *Energy Procedia,* vol. 4, pp. 779-786, 2011.

[16] H. Zhai, "Advanced membranes and learning scale required for cost-effective post-combustion carbon capture," *Iscience,* vol. 13, pp. 440-451, 2019.

[17] O. Y. Perevertaylenko, A. O. Gariev, T. Damartzis, L. L. Tovazhnyanskyy, P. O. Kapustenko, and O. P. Arsenyeva, "Searches of cost effective ways for amine absorption unit design in CO2 post-combustion capture process," *Energy,* vol. 90, pp. 105-112, 2015.

[18] G. C. Institute. "Capturing CO2." https://www.globalccsinstitute.com/archive/hub/publications/191018/fact-sheet-capturing-co2.pdf (accessed.

[19] H. G. Darabkhani, H. Varasteh, and B. Bazooyar, *Carbon Capture Technologies for Gas-Turbine-Based Power Plants*. Elsevier, 2022.

[20] D. Jansen, M. Gazzani, G. Manzolini, E. van Dijk, and M. Carbo, "Pre-combustion CO2 capture," *International Journal of Greenhouse Gas Control,* vol. 40, pp. 167-187, 2015.

[21] C. A. del Pozo, S. Cloete, J. H. Cloete, Á. J. Álvaro, and S. Amini, "The oxygen production pre-combustion (OPPC) IGCC plant for efficient power production with CO2 capture," *Energy Conversion and Management,* vol. 201, p. 112109, 2019.

[22] P. Cobden *et al.*, "Sorption-enhanced hydrogen production for pre-combustion CO2 capture: Thermodynamic analysis and experimental results," *International journal of greenhouse gas control,* vol. 1, no. 2, pp. 170-179, 2007.

[23] E. I. Koytsoumpa, C. Bergins, and E. Kakaras, "The CO2 economy: Review of CO2 capture and reuse technologies," *The Journal of Supercritical Fluids,* vol. 132, pp. 3-16, 2018.

[24] L. Zheng, *Oxy-fuel combustion for power generation and carbon dioxide (CO2) capture*. Elsevier, 2011.

[25] M. A. Nemitallah *et al.*, "Oxy-fuel combustion technology: current status, applications, and trends," *International Journal of Energy Research,* vol. 41, no. 12, pp. 1670-1708, 2017.

[26] R. Stanger *et al.*, "Oxyfuel combustion for CO2 capture in power plants," *International journal of greenhouse gas control,* vol. 40, pp. 55-125, 2015.

[27] I. Pfaff and A. Kather, "Comparative thermodynamic analysis and integration issues of CCS steam power plants based on oxy-combustion with cryogenic or membrane based air separation," *Energy Procedia,* vol. 1, no. 1, pp. 495-502, 2009.

[28] F. Wu, M. D. Argyle, P. A. Dellenback, and M. Fan, "Progress in O2 separation for oxy-fuel combustion–A promising way for cost-effective CO2 capture: A review," *Progress in Energy and Combustion Science,* vol. 67, pp. 188-205, 2018.

[29] V. Anthony Veder. "CO2 Liquid Logistics Shipping Concept (LLSC): Overall Supply Chain Optimization." https://www.globalccsinstitute.com/archive/hub/publications/19011/co2-liquid-logistics-shipping-concept-llsc-overall-supply-chain-optimization.pdf (accessed.

[30] S. T. Munkejord, M. Hammer, and S. W. Løvseth, "CO2 transport: Data and models–A review," *Applied Energy,* vol. 169, pp. 499-523, 2016.

[31] R. Svensson, M. Odenberger, F. Johnsson, and L. Strömberg, "Transportation systems for CO2—application to carbon capture and storage," *Energy conversion and management,* vol. 45, no. 15-16, pp. 2343-2353, 2004.

[32] R. Skagestad *et al.*, "Ship transport of CO2-status and technology gaps," *Tel-Tek Report,* vol. 2214090, pp. 1-52, 2014.

[33] M. Equinor, "Northern Lights Project Concept Report," Tech. Rep. RE-PM673-00001. Available from https://northernlightsccs. com …, 2019.

[34] S. Roussanaly, H. Deng, G. Skaugen, and T. Gundersen, "At what pressure shall CO2 be transported by ship? An in-depth cost comparison of 7 and 15 barg shipping," *Energies,* vol. 14, no. 18, p. 5635, 2021.

[35] A. Omata and K. Hattori, "Preliminary feasibility study on CO2 carrier for ship-based CCS," *Global CCS Institute,* 2011.

[36] ZEP/CCSA. "Guidance for CO2 transport by ship." https://zeroemissionsplatform.eu/wp-content/uploads/ZEP-CCSA-Report-on-CO2-transport-by-ship-March-2022.pdf (accessed.

[37] J. Kjärstad, R. Skagestad, N. H. Eldrup, and F. Johnsson, "Ship transport—A low cost and low risk CO2 transport option in the Nordic countries," *International Journal of Greenhouse Gas Control,* vol. 54, pp. 168-184, 2016.

[38] K. Johnsen, K. Helle, S. Røneid, and H. Holt, "DNV recommended practice: Design and operation of CO2 pipelines," *Energy Procedia,* vol. 4, pp. 3032-3039, 2011.

[39] S. M. Forbes, P. Verma, T. E. Curry, S. J. Friedmann, and S. M. Wade, "Guidelines for carbon dioxide capture, transport and storage," *Guidelines for carbon dioxide capture, transport and storage.,* 2008.

[40] A. Dugstad, M. Halseid, and B. Morland, "Effect of SO2 and NO2 on corrosion and solid formation in dense phase CO2 pipelines," *Energy Procedia,* vol. 37, pp. 2877-2887, 2013.

[41] E. Energy, "CO2 Pipeline Infraestructure: An analysis of global challenges and opportunities," *Final report for IEA Greenhouse Gas Programme,* vol. 450, pp. 1-134, 2010.

[42] M. Chaczykowski and A. J. Osiadacz, "Dynamic simulation of pipelines containing dense phase/supercritical CO2-rich mixtures for carbon capture and storage," *International Journal of Greenhouse Gas Control,* vol. 9, pp. 446-456, 2012.

[43] FEED, "CO2 Transport Pipeline ", 2011. [Online]. Available: https://www.globalccsinstitute.com/archive/hub/publications/77446/feed-study-co2-transport-pipeline.pdf

[44] I. E. Agency, "Development of a Global CO2 pipeline infrastructure," 2010. [Online]. Available: https://ieaghg.org/docs/General_Docs/Reports/2010-13.pdf

[45] D. N. Veritas, "Design and operation of CO2 pipelines," *DNV RP-J202,* 2010.

[46] G. C. Institute, "CO2 Pipeline Infrastructure ", 2014. [Online]. Available: https://ieaghg.org/docs/General_Docs/Reports/2013-18.pdf

[47] S. P. Peletiri, N. Rahmanian, and I. M. Mujtaba, "CO2 Pipeline design: A review," *Energies,* vol. 11, no. 9, p. 2184, 2018.

[48] H. Lu, X. Ma, K. Huang, L. Fu, and M. Azimi, "Carbon dioxide transport via pipelines: A systematic review," *Journal of Cleaner Production,* vol. 266, p. 121994, 2020.

[49] I. GHG, "Wellbore integrity network summary," 2012. [Online]. Available: https://ieaghg.org/docs/General_Docs/Reports/2012-01.pdf

[50] E. Lindeberg and P. Bergmo, "The long-term fate of CO2 injected into an aquifer," *Greenhouse gas control technologies,* vol. 1, pp. 489-494, 2003.

[51] M. A. Celia, J. M. Nordbotten, S. Bachu, M. Dobossy, and B. Court, "Risk of leakage versus depth of injection in geological storage," *Energy Procedia,* vol. 1, no. 1, pp. 2573-2580, 2009.

[52] P. A. Patil *et al.*, "FEP Based Model Development for Assessing Well Integrity Risk Related to CO2 Storage in Central Luconia Gas Fields in Sarawak," in *International Petroleum Technology Conference*, 2021: OnePetro.

[53] APEC, "Building capacity for CO2 capture and storage in the APEC region," 2012. [Online]. Available: https://www.globalccsinstitute.com/archive/hub/publications/114711/building-capacity-co2-capture-and-storage-apec-region.pdf

[54] D. GL, "Miljørisiko for EL001, Northern Lights, mottak og permanent lagring av CO2," 2019. [Online]. Available: https://norlights.com/wp-content/uploads/2021/03/Environmental-risk-analysis-and-strategy-for-environmental-monitoring-Norwegian.pdf

[55] D. GL, "Use of risk assessments and performance requirements for selection of offshore subsea leak detection systems," 2018. [Online]. Available: https://www.ptil.no/contentassets/5ba82b64b2f941548ecf55217696ba3c/use-of-risk-assessments-and-performace-aquirements-for-selection-of-offshore-subsea-leak-detection-systems.pdf

[56] K. Li, X. Zhou, R. Tu, Q. Xie, and X. Jiang, "The flow and heat transfer characteristics of supercritical CO2 leakage from a pipeline," *Energy,* vol. 71, pp. 665-672, 2014.

[57] W. J. Kostowski and J. Skorek, "Real gas flow simulation in damaged distribution pipelines," *Energy,* vol. 45, no. 1, pp. 481-488, 2012.

[58] D.-p. Huang, G.-l. Ding, and H. Quack, "Theoretical analysis of deposition and melting process during throttling high pressure CO2 into atmosphere," *Applied thermal engineering,* vol. 27, no. 8-9, pp. 1295-1302, 2007.

[59] Z. Ziabakhsh-Ganji and H. Kooi, "Sensitivity of Joule–Thomson cooling to impure CO2 injection in depleted gas reservoirs," *Applied energy,* vol. 113, pp. 434-451, 2014.

[60] I. Khalil and D. R. Miller, "The structure of supercritical fluid free-jet expansions," *AIChE Journal*, vol. 50, no. 11, pp. 2697-2704, 2004.

[61] K. Shitashima, Y. Maeda, and T. Ohsumi, "Development of detection and monitoring techniques of CO2 leakage from seafloor in sub-seabed CO2 storage," *Applied geochemistry*, vol. 30, pp. 114-124, 2013.

[62] I. GHG, "Quantification techniques for CO2 leakage," 2012. [Online]. Available: https://ieaghg.org/docs/General_Docs/Reports/2012-02.pdf

[63] K. Michael *et al.*, "Geological storage of CO2 in saline aquifers—A review of the experience from existing storage operations," *International journal of greenhouse gas control*, vol. 4, no. 4, pp. 659-667, 2010.

[64] M. Jakobsson, L. Mayer, and D. Monahan, "Arctic Ocean bathymetry: A necessary geospatial framework," *Arctic*, pp. 41-47, 2015.

[65] J. Greinert, "Monitoring temporal variability of bubble release at seeps: The hydroacoustic swath system GasQuant," *Journal of Geophysical Research: Oceans*, vol. 113, no. C7, 2008.

[66] S. Jagannathan *et al.*, "Ocean acoustic waveguide remote sensing (OAWRS) of marine ecosystems," *Marine Ecology Progress Series*, vol. 395, pp. 137-160, 2009.

[67] R. Arts, O. Eiken, A. Chadwick, P. Zweigel, L. Van der Meer, and B. Zinszner, "Monitoring of CO2 injected at Sleipner using time-lapse seismic data," *Energy*, vol. 29, no. 9-10, pp. 1383-1392, 2004.

[68] R. Chadwick, D. Noy, R. Arts, and O. Eiken, "Latest time-lapse seismic data from Sleipner yield new insights into CO2 plume development," *Energy Procedia*, vol. 1, no. 1, pp. 2103-2110, 2009.

[69] O. Eiken, I. Brevik, R. Nitg-Tno, E. L. Sintef, and K. Fagervik, "Seismic monitoring of CO2 injected into a marine acquifer," in *2000 SEG Annual Meeting*, 2000: OnePetro.

[70] D. P. Strogen, Arnot, M. J., Bland, K. J., and Griffin, A. G. , "Opportunities for underground geological storage of CO2 in New Zealand - Report CCS-08/7 - Onshore Taranaki Neogene reservoirs.

GNS Science Report 2009/60. 104 p. ," 2009. [Online]. Available: https://www.researchgate.net/profile/Kj-Bland/publication/268435094_Opportunities_for_underground_geological_storage_of_CO2_in_New_Zealand_-Report_CCS_-087_-Onshore_Taranaki_Neogene_reservoirs/links/5509cf430cf20f127f90ad4a/Opportunities-for-underground-geological-storage-of-CO2-in-New-Zealand-Report-CCS-08-7-Onshore-Taranaki-Neogene-reservoirs.pdf

[71] Equinor. "Northern Lights - Receiving and permanent storage of CO2." https://norlights.com/wp-content/uploads/2021/03/RE-PM673-00011-02-Impact-Assessment.pdf (accessed.

[72] B. Metz, O. Davidson, H. De Coninck, M. Loos, and L. Meyer, *IPCC special report on carbon dioxide capture and storage*. Cambridge: Cambridge University Press, 2005.

[73] A. Bielinski, A. Kopp, H. Schütt, and H. Class, "Monitoring of CO2 plumes during storage in geological formations using temperature signals: Numerical investigation," *International journal of greenhouse gas control,* vol. 2, no. 3, pp. 319-328, 2008.

[74] A. Liebscher *et al.*, "Injection operation and operational pressure–temperature monitoring at the CO2 storage pilot site Ketzin, Germany—Design, results, recommendations," *International Journal of Greenhouse Gas Control,* vol. 15, pp. 163-173, 2013.

[75] S. D. Hovorka *et al.*, "Monitoring a large volume CO2 injection: Year two results from SECARB project at Denbury's Cranfield, Mississippi, USA," *Energy Procedia,* vol. 4, pp. 3478-3485, 2011.

[76] K. Shitashima, "Application of chemical sensor to oceanography-development of deep sea pH sensor using ISFET," *Chikyukagaku (Geochemistry),* vol. 32, pp. 1-11, 1998.

[77] K. Shitashima, Y. Koike, M. Kyo, and A. Hemmi, "Development of electrochemical in-situ pH-pCO 2 sensor for deep-sea oceanography applications," in *SENSORS, 2008 IEEE*, 2008: IEEE, pp. 1414-1417.

[78] K. Shitashima, Y. Maeda, Y. Koike, and T. Ohsumi, "Natural analogue of the rise and dissolution of liquid CO2 in the ocean," *International journal of greenhouse gas control,* vol. 2, no. 1, pp. 95-104, 2008.

[79] I.-K. Waarum *et al.*, "CCS leakage detection technology-Industry needs, government regulations, and sensor performance," *Energy Procedia,* vol. 114, pp. 3613-3627, 2017.

[80] J. Blackford and F. Gilbert, "pH variability and CO2 induced acidification in the North Sea," *Journal of Marine Systems,* vol. 64, no. 1-4, pp. 229-241, 2007.

[81] H. A. Botnen, A. M. Omar, I. Thorseth, T. Johannessen, and G. Alendal, "The effect of submarine CO2 vents on seawater: Implications for detection of subsea carbon sequestration leakage," *Limnology and Oceanography,* vol. 60, no. 2, pp. 402-410, 2015.

[82] J. J. Roberts, S. M. Gilfillan, L. Stalker, and M. Naylor, "Geochemical tracers for monitoring offshore CO2 stores," *International Journal of Greenhouse Gas Control,* vol. 65, pp. 218-234, 2017.

[83] A. Flohr *et al.*, "Utility of natural and artificial geochemical tracers for leakage monitoring and quantification during an offshore controlled CO2 release experiment," *International Journal of Greenhouse Gas Control,* vol. 111, p. 103421, 2021.

[84] M. Myers, L. Stalker, B. Pejcic, and A. Ross, "Tracers–Past, present and future applications in CO2 geosequestration," *Applied geochemistry,* vol. 30, pp. 125-135, 2013.

[85] A. M. Omar *et al.*, "Detection and quantification of CO2 seepage in seawater using the stoichiometric Cseep method: Results from a recent subsea CO2 release experiment in the North Sea," *International Journal of Greenhouse Gas Control,* vol. 108, p. 103310, 2021.

[86] P. G. Brewer *et al.*, "Three-dimensional acoustic monitoring and modeling of a deep-sea CO2 droplet cloud," *Geophysical research letters,* vol. 33, no. 23, 2006.

[87] H. Hirayama *et al.*, "Culture-dependent and-independent characterization of microbial communities associated with a shallow submarine hydrothermal system occurring within a coral reef off Taketomi Island, Japan," *Applied and environmental microbiology*, vol. 73, no. 23, pp. 7642-7656, 2007.

[88] Y. Furushima, M. Nagao, A. Suzuki, H. Yamamoto, and T. Maruyama, "Periodic behavior of the bubble jet (geyser) in the Taketomi submarine hot springs of the southern part of Yaeyama Archipelago, Japan," *Marine Technology Society Journal*, vol. 43, no. 3, pp. 13-22, 2009.

[89] A. International. "Why pipeline leak detection is a crucial element of Carbon capture and storage (CCS)." https://www.atmosi.com/us/news-events/blogs/why-pipeline-leak-detection-is-a-crucial-element-of-carbon-capture-and-storage-ccs/#lds%20for%20carbon (accessed.

[90] D. GL, "Offshore leak detection," 2019. [Online]. Available: https://www.dnv.com/oilgas/download/dnv-rp-f302-offshore-leak-detection.html

[91] M. A. Adegboye, W.-K. Fung, and A. Karnik, "Recent advances in pipeline monitoring and oil leakage detection technologies: Principles and approaches," *Sensors*, vol. 19, no. 11, p. 2548, 2019.

[92] S. Solomon, M. Carpenter, and T. A. Flach, "Intermediate storage of carbon dioxide in geological formations: a technical perspective," *International journal of greenhouse gas control*, vol. 2, no. 4, pp. 502-510, 2008.

[93] A. Kovscek and M. Cakici, "Geologic storage of carbon dioxide and enhanced oil recovery. II. Cooptimization of storage and recovery," *Energy conversion and Management*, vol. 46, no. 11-12, pp. 1941-1956, 2005.

[94] I. GHG, "Enhanced coal bed methane recovery with CO2 sequestration," *PH3/3, International Energy Agency Greenhouse Gas R&D Programme, Cheltenham*, vol. 139, 1998.

[95] P. Ringrose, *How to store CO2 underground: Insights from early-mover CCS Projects*. Springer, 2020.

[96] N. Singh, "Deep saline aquifiers for sequestration of carbon dioxide," in *International geological congress, Oslo*, 2008.

[97] G. C. Institute. "Carbon capture and storage images." https://www.globalccsinstitute.com/resources/ccs-image-library/ (accessed.

[98] Y. F. Zhang. "Carbon Capture and Sequestration in Europe: Growth Rate Key To Meet Climate Change Mitigation Targets." https://jpt.spe.org/twa/carbon-capture-and-sequestration-in-europe-growth-rate-key-to-meet-climate-change-mitigation-targets#:~:text=Energy%20systems%20models%20such%20as,of%20the%20global%20economy%20(Fig. (accessed.

[99] Equinor. "Sleipner partnership releases CO2 storage data." https://www.equinor.com/news/archive/2019-06-12-sleipner-co2-storage-data (accessed.

[100] D. Pichot, L. Granados, T. Morel, A. Schuller, R. Dubettier, and F. Lockwood, "Start-up of Port-Jérôme CRYOCAP™ Plant: Optimized Cryogenic CO2 Capture from H2 Plants," *Energy Procedia*, vol. 114, pp. 2682-2689, 2017.

[101] M. Ros, A. Read, J. Uilenreef, and J. Limbeek, "Start of a CO2 Hub in Rotterdam: Connecting CCS and CCU," *Energy Procedia,* vol. 63, pp. 2691-2701, 2014.

[102] L. Beck, "Carbon capture and storage in the USA: the role of US innovation leadership in climate-technology commercialization," *Clean Energy,* vol. 4, no. 1, pp. 2-11, 2020.

[103] IOGP. "CCUS projects in Europe." https://iogpeurope.org/wp-content/uploads/2022/11/Map-of-EU-CCUS-Projects.pdf (accessed.

[104] M. F. Hasan, E. L. First, F. Boukouvala, and C. A. Floudas, "A multi-scale framework for CO2 capture, utilization, and sequestration: CCUS and CCU," *Computers & Chemical Engineering,* vol. 81, pp. 2-21, 2015.

[105] S. Roussanaly and A.-A. Grimstad, "The economic value of CO2 for EOR applications," *Energy Procedia,* vol. 63, pp. 7836-7843, 2014.

[106] SINTEF. "MACON CCS." https://www.sintef.no/en/projects/2021/macon-ccs/ (accessed.

[107] A. Chawla *et al.*, "IoT-Based Monitoring in Carbon Capture and Storage Systems," *IEEE Internet of Things Magazine,* vol. 5, no. 4, pp. 106-111, 2022.

[108] Equinor. "Northern Lights." https://norlights.com/ (accessed.

[109] O. Engineer. "Norway to Launch $2,7B Carbon Capture and Storage Project 'Longship'." https://www.oedigital.com/news/481822-norway-to-launch-2-7b-carbon-capture-and-storage-project-longship (accessed.

[110] N. A. Røkke and H. Knuutila, "TCCS–10. CO2 Capture, Transport and Storage Trondheim 17th–19th June 2019. Selected papers," ed: SINTEF Academic Press, 2019.

[111] N. Lights. "Annual report Northern Lights 2021." https://norlights.com/wp-content/uploads/2022/04/Northern-Lights-Annual-report-2021.pdf (accessed.

[112] J.-Q. Shi, C. Imrie, C. Sinayuc, S. Durucan, A. Korre, and O. Eiken, "Snøhvit CO2 storage project: Assessment of CO2 injection performance through history matching of the injection well pressure over a 32-months period," *Energy Procedia,* vol. 37, pp. 3267-3274, 2013.

[113] T. Maldal and I. Tappel, "CO2 underground storage for Snøhvit gas field development," *Energy,* vol. 29, no. 9-10, pp. 1403-1411, 2004.

[114] O. Kårstad, "Geological storage, including costs and risks, in saline aquifers," in *WORKSHOP ON CARBON DIOXIDE CAPTURE AND STORAGE*, 2003, p. 53.

[115] O. Hansen *et al.*, "Snøhvit: The history of injecting and storing 1 Mt CO2 in the fluvial Tubåen Fm," *Energy Procedia,* vol. 37, pp. 3565-3573, 2013.

[116] N. P. Directorate. "Storage capacity Snøhvit area." https://www.npd.no/en/facts/publications/co2-atlases/co2-atlas-for-the-norwegian-continental-shelf/6-the-barents-sea/6.2-storage-options-of-the-barents-sea/6.2.1-saline-aquifers/storage-capacity-snohvit-area/ (accessed.

[117] Equinor. "Snøhvit Future, Hammerfest LNG and Melkøya." https://www.equinor.com/no/energi/snohvit (accessed.

[118] O. Eiken, P. Ringrose, C. Hermanrud, B. Nazarian, T. A. Torp, and L. Høier, "Lessons learned from 14 years of CCS operations: Sleipner, In Salah and Snøhvit," *Energy procedia*, vol. 4, pp. 5541-5548, 2011.

[119] R. Chadwick, G. Williams, and I. Falcon-Suarez, "Forensic mapping of seismic velocity heterogeneity in a CO2 layer at the Sleipner CO2 storage operation, North Sea, using time-lapse seismics," *International Journal of Greenhouse Gas Control*, vol. 90, p. 102793, 2019.

[120] A. Chadwick *et al.*, "Quantitative analysis of time-lapse seismic monitoring data at the Sleipner CO 2 storage operation," *The Leading Edge*, vol. 29, no. 2, pp. 170-177, 2010.

[121] S. Hagen. "Offshore CCS-projects in Norway." https://www.standard.no/Global/externalSites/ISO-TC-265-Oslo2015/Workshop/4%20Sveinung%20Hagen.pdf (accessed.

[122] MIT. "Sleipner Fact Sheet: Carbon Dioxide Capture and Storage Project." https://sequestration.mit.edu/tools/projects/sleipner.html (accessed.

[123] R. Chadwick, "Offshore CO2 storage: Sleipner natural gas field beneath the North Sea," in *Geological Storage of Carbon Dioxide (CO2)*: Elsevier, 2013, pp. 227-253e.

[124] O. Eiken, "Twenty Years of Monitoring CO2 Injection," *Geophysics and geosequestration*, p. 209, 2019.

[125] SINTEF. "Sleipner partnership releases CO2 storage data." https://www.sintef.no/en/latest-news/2019/sleipner-partnership-releases-co2-storage-data/ (accessed.

[126] SINTEF. "CO2 DataShare." https://co2datashare.org/ (accessed.

[127] H. Energi. "Maturing the Barents Blue project and developing new CCS business." https://www.horisontenergi.no/wp-content/uploads/2022/08/Horisont-Energi-Q222-Report-260822-FINAL.pdf (accessed.

[128] H. energi. "Project Barents Blue." https://www.horisontenergi.no/wp-content/uploads/2021/06/Barents-Blue-Project-Flyer-2021.pdf (accessed.

[129] H. Energi. "Barents Blue." https://www.tffk.no/_f/p1/i8a04b485-5574-422a-b814-da99c1c6685b/barents_blue_project_planforum_220120.pdf (accessed.

[130] N. e-fuel. "Norsk e-fuel." https://www.norsk-e-fuel.com/about-us?hsCtaTracking=416caa6e-0baf-4043-90ba-6d6d1a3cbbac%7Cc18e0fb2-4cae-47d9-a4e9-33e484004f78 (accessed.

[131] Sunfire. "Norsk e-fuel is planning Europe's first commercial plant for hydrogen-based renewable aviation fuel in Norway." https://www.sunfire.de/en/news/detail/norsk-e-fuel-is-planning-europes-first-commercial-plant-for-hydrogen-based-renewable-aviation-fuel-in-norway (accessed.

[132] B. C. AS. "Carbon Capture & Storage (CCS)." https://www.borgco2.no/ (accessed.

[133] B. C. AS. "Press release-Borg CO2 and Northern Lights to collaborate on Carbon Capture and Storage." https://www.borgco2.no/news/press-release-borg-co2-and-northern-lights-to-collaborate-on-carbon-capture-and-storage (accessed.

[134] B. CO2. "Utvidet mulighetsstudie." https://static1.squarespace.com/static/5cdba5274d546e0576dc53c7/t/633d7d156e8e6e430cfc71c5/1664974127440/220227_sluttrapp_CLIMIT_UMS_endelig.pdf (accessed.

[135] B. CO2. "Borg CO2 in Norwegian perspective." https://www.borgco2.no/news/borg-co2s-first-newsletter (accessed.

[136] Equinor. "Equinor awarded the Smeaheia and Polaris CO2 licenses." https://www.equinor.com/news/archive/20220405-awarded-smeaheia-polaris-co2-licenses (accessed.

[137] M. Fawad, M. J. Rahman, and N. H. Mondol, "Seismic reservoir characterization of potential CO2 storage reservoir sandstones in Smeaheia area, Northern North Sea," *Journal of Petroleum Science and Engineering*, vol. 205, p. 108812, 2021.

[138] Gassnova. "Smeaheia Dataset." https://co2datashare.org/dataset/smeaheia-dataset (accessed.

[139] E. De Visser *et al.*, "Dynamis CO2 quality recommendations," *International journal of greenhouse gas control*, vol. 2, no. 4, pp. 478-484, 2008.

[140] Y.-S. Choi, S. Nesic, and D. Young, "Effect of impurities on the corrosion behavior of CO2 transmission pipeline steel in supercritical CO2− water environments," *Environmental science & technology*, vol. 44, no. 23, pp. 9233-9238, 2010.

[141] P. Shirley and P. Myles, "Quality Guidelines for Energy System Studies: CO2 Impurity Design Parameters," National Energy Technology Laboratory (NETL), Pittsburgh, PA, Morgantown, WV …, 2019.

[142] M. Moshfeghian. "Transportation of CO2 in Dense Phase." http://www.jmcampbell.com/tip-of-the-month/2012/01/transportation-of-co2-in-dense-phase/#:~:text=liquid%20and%20gas.-,The%20dense%20phase%20has%20a%20viscosity%20similar%20to%20that%20of,reservoir%20for%20enhanced%20oil%20recovery. (accessed.

[143] I. K. A. T. plc. "Multiflash for Windows." https://weblog.chylowen.co.uk/portfolio/SelectedPagesMultiFlash.pdf (accessed.

[144] NIST. "Thermophysical Properties of Fluid Systems." https://webbook.nist.gov/chemistry/fluid/ (accessed.

[145] I. Al-Siyabi, "Effect of impurities on CO2 stream properties," Heriot-Watt University, 2013.

[146] SINTEF. "Thermopack." https://www.sintef.no/en/software/thermopack/ (accessed.

[147] H. F. Hemond and E. J. Fechner, *Chemical fate and transport in the environment*. Academic Press, 2022.

[148] L. J. Pekot, P. Petit, Y. Adushita, S. Saunier, and R. De Silva, "Simulation of two-phase flow in carbon dioxide injection wells," in *SPE Offshore Europe Oil and Gas Conference and Exhibition*, 2011: OnePetro.

[149] SINTEF. "DeFACTO - Demonstration of Flow Assurance for CO2 Transport Operations." https://www.sintef.no/en/projects/2016/defacto/ (accessed.

[150] Å. Rasmussen, "Field applications of model-based multiphase flow computing," in *North Sea flow measurment workshop, St Andrews, UK*, 2004.

[151] S. Evje and T. Flåtten, "CFL-violating numerical schemes for a two-fluid model," *Journal of Scientific Computing,* vol. 29, pp. 83-114, 2006.

[152] K. H. Bendlksen, D. Malnes, R. Moe, and S. Nuland, "The dynamic two-fluid model OLGA: Theory and application," *SPE production engineering,* vol. 6, no. 02, pp. 171-180, 1991.

[153] S. Limited. "OLGA Dynamic Multiphase Flow Simulator." https://www.software.slb.com/products/olga (accessed.

[154] KBC. "Multiflash." https://www.kbc.global/process-optimization/technology/simulation-software/multiflash-simulation-software/ (accessed.

[155] G. de Koeijer, J. H. Borch, J. Jakobsenb, and M. Drescher, "Experiments and modeling of two-phase transient flow during CO2 pipeline depressurization," *Energy Procedia,* vol. 1, no. 1, pp. 1683-1689, 2009.

[156] B. Toulas. "AISI 316 Stainless Steel: Specification and Datasheet." https://www.engineeringclicks.com/aisi-316-stainless-steel/ (accessed.

[157] Calsep. "Modeling of CO2 Properties." https://www.calsep.com/14-modeling-of-co2-properties/ (accessed.

[158] O. Kunz and W. Wagner, "The GERG-2008 wide-range equation of state for natural gases and other mixtures: an expansion of GERG-2004," *Journal of chemical & engineering data,* vol. 57, no. 11, pp. 3032-3091, 2012.

[159] R. Stryjek and J. Vera, "PRSV: An improved Peng—Robinson equation of state for pure compounds and mixtures," *The canadian journal of chemical engineering,* vol. 64, no. 2, pp. 323-333, 1986.

[160] P. Ding-Yu and B. R. Donald, "A new two-constant equation of state," *Industrial & Engineering Chemistry Fundamentals,* vol. 15, no. 1, pp. 59-64, 1976.

[161] B. E. Poling, J. M. Prausnitz, and J. P. O'connell, *Properties of gases and liquids*. McGraw-Hill Education, 2001.

[162] M.-J. Huron and J. Vidal, "New mixing rules in simple equations of state for representing vapour-liquid equilibria of strongly non-ideal mixtures," *Fluid Phase Equilibria,* vol. 3, no. 4, pp. 255-271, 1979.

[163] E. I. Epelle, J. O. Oyinbo, J. A. Okolie, and D. I. Gerogiorgis, "A comparative performance evaluation of cubic equations of state for predicting the compositional distribution of hydrate inhibitors in reservoir fluid systems," *Fluid Phase Equilibria,* vol. 535, p. 112964, 2021.

[164] G. Soave, "Equilibrium constants from a modified Redlich-Kwong equation of state," *Chemical engineering science,* vol. 27, no. 6, pp. 1197-1203, 1972.

[165] SCRIBD. "PVTsim Tutorial Calsep." https://www.scribd.com/document/270076582/PVTsim-Tutorial-Calsep (accessed.

[166] NIST. "About NIST." https://www.nist.gov/about-nist (accessed.

Appendices

Appendix A: Task Description

University of South-Eastern Norway

Faculty of Technology, Natural Sciences and Maritime Sciences, Campus Porsgrunn

FMH606 Master's Thesis

Title: Thermodynamics and fluid flow models for CO_2 flow assurance

USN supervisor: main supervisor Amaranath Sena Kumara Wahumpurage, co-supervisor Britt Margrethe Emilie Moldestad

External partner: TechnipFMC & SINTEF

Task background:
The proposed topic will be part of the Macon CCS (Monitoring and Control of Networks in Carbon Capture and Storage) research project in collaboration with TechnipFMC, SINTEF and other industry partners. Macon CCS aims to be an enabler for large-scale deployment of CCS from industrial sources by addressing selected and internationally recognized barriers in monitoring and control of diverse industrial CCS transport networks.
https://www.sintef.no/en/projects/2021/macon-ccs/

Task description:
Benchmarking pure CO2 pipe flow experimental data made available by SINTEF with results from a flow simulator. The effect of CO_2 with impurities compared with pure CO_2 on pipe flow simulations can be further investigated. A literature review on leakage detection methods suitable for subsea CO_2 transport will be performed.

Student category: PT student

Is the task suitable for online students (not present at the campus)? Yes

Practical arrangements:
zzz

Supervision:
As a general rule, the student is entitled to 15-20 hours of supervision. This includes necessary time for the supervisor to prepare for supervision meetings (reading material to be discussed, etc).

Signatures:

Supervisor:
main supervisor: Amaranath Sena Kumara Wahumpurage
co-supervisor: Britt Margrethe Emilie Moldestad
from TechnipFMC: Angela Lynn De Leebeeck, Jaspreet Singh Sachdeva

Student: ALUA AKHMETOVA

Date: 15.11.2022